Applications for the Electroless Deposition of Gold Nanoparticles onto Silicon

by

Morgan Millard
BSc, University of New Brunswick, 2010

A Thesis Submitted in Partial Fulfillment
of the Requirements for the Degree of

MASTER'S OF SCIENCE

in the Department of Chemistry

Supervisory Committee

Applications for the Electroless Deposition of Gold Nanoparticles onto Silicon

by

Morgan Millard
BSc, University of New Brunswick, 2010

Supervisory Committee

Dr. Alexandre Brolo, (Department of Chemistry)
Supervisor

Dr. Matt Moffitt, (Department of Chemistry)
Departmental Member

Dr. Byoung-Chul Choi, (Department of Physics)
Outside Member

Abstract

Supervisory Committee
Dr. Alexandre Brolo, (Department of Chemistry)
Supervisor
Dr. Matt Moffit, (Department of Chemistry)
Departmental Member
Dr. Byoung-Chul Choi, (Department of Physics)
Outside Member

Gold nanoparticles were deposited onto a silicon substrate using electroless deposition. The process was optimized by adjusting the deposition time, the temperature of the plating solution, the amount of time that the silicon was exposed to hydrofluoric acid, and the concentration of the plating solution. The nanoparticles deposited on the silicon were characterized using scanning electron microscopy.

The optimized electroless deposition process was then used to modify the surface of silicon solar cells with gold nanoparticles for enhanced power generation. Spectral response and I-V curve tests were performed on the modified solar cells to quantify the enhancements. The modified surfaces of the silicon solar cells were characterized by scanning electron microscopy and reflectance measurements.

The electroless deposition process was also used to generate nanostructures for surface-enhanced Raman scattering (SERS). A template-nanohole array was fabricated on silicon by focused ion beam milling. Gold nanoparticles were deposited in the holes of the template, resulting in interesting gold-nanodoughnut structures. The gold nanodoughnuts were examined by scanning electron microscopy, and their potential as SERS substrates were tested using Rhodamine 6G as a molecular probe under 633 nm laser excitation.

Table of Contents

List of Tables

List of Figures

Acknowledgments

I have been very blessed with the opportunity, and the privilege to do my Masters of Science, and to have so many people that helped me along the way and made everything possible. First and foremost, I would like to thank my supervisor, Dr. Alex Brolo. For his generosity in responding to my email and offering me a position after my funding had been cut in another program only a week before classes started (even if he did think I was girl), and for all the help, support and patience he has given me since - Thank you. I would also like to thank Milton Wang, who helped me understand everything about my research and helped me brainstorm ways to get around all the hurdles that showed up along the way. I would also like to thank the rest of the Brolo group, the ones still here and the ones who have moved on, Elaine Humphrey and Adam Schuetze for all their help with the SEM, and anyone else who helped make this possible, it has been a pleasure to work with all of you.

For more personal acknowledgements, I want to thank my parents, Glenda Hope and John Burdon, who have never been anything but hugely supportive of whatever I decide to do. Thank you for giving me the opportunity to go to university to begin with and the encouragement you have always given to push myself to achieve anything. Lastly, I would like to thank my girlfriend, Caitlinn O'Leary, who has made everything about this degree easier and more enjoyable. Even without the Master's Degree you have made this whole journey worth it.

Dedication

I dedicate this work to my mom, Glenda Hope, because mentioning her in the acknowledgements does not give enough credit for everything this amazing woman has done for me.

Chapter 1: Introduction

Technology has undergone a vast evolution over the past one hundred years. In this relatively short amount of time, huge advancements have been made in everything from transportation to medicine. As mankind continues to grow and learn, new technological achievements are introduced. However, in order to keep the momentum of technological advancements going through to the next century and beyond, priority must be placed in the constant improvement of what mankind has already achieved.

In the pursuit of better and better technology, there are two pathways that a researcher can take. The first is to try to make something that is completely different than what has been done before, investigating the properties of new materials, or even making new materials in order to advance the science. The second is to build from previous implementations, making what was made more efficient, in either cost or performance.

The research presented in this thesis works under the premise of the second pathway. As mentioned previously, in order to make an existing technology better, either the cost, both in materials and labour, or the effectiveness of the technology must be improved. An excellent example of this is in computers. When computers were first made they took up so much space that entire rooms were required to house them; however, even taking into account their considerable size, the work they could do was extremely limited. Due to their size, and the cost of producing such a large construct, the consumer base for this product was very limited, with only wealthy schools, universities and some professional businesses having access to them. Since their creation, computers can now fit in a pocket, and are commonly used by many people within developed countries. This constant reduction in size was possible through the miniaturization of the necessary

components within computers. Therefore, due to their reduced size, the technology has become more cost effective, as well as more effective in terms of the limitations computers had when first developed. This has been the general trend for improvement in most technological fields, to make devices smaller, or using less materials, while still trying to improve their performance. Currently, this reduction has reached nano-scale device components within the research community.

At the nano-scale, a large amount of interest has been placed into the fabrication of nanoparticles and nanostructures. It has been found that materials display unique properties at this scale that are not seen in the bulk. Among these properties, being most relevant for this thesis, is plasmonic resonance[1], which will be discussed in more detail in Chapter 2. Plasmonics are achieved using nano-scaled structures of electron rich metal, usually gold or silver. Therefore, the fabrication of metal nanoparticles and nanostructures has been heavily researched[2,3].

Typically, nanoparticles are fabricated by the reduction of metal ions in solution, the reduced metal undergoes nucleation forming spherical nanoparticles that are suspended in the solution[4,5]. These nanoparticles are then attached to a surface that has been modified with the proper chemical groups[6]. Nanoparticles have other applications that do not require them to be immobilized on a surface[7], but for the purposes of this research they are immobilized. This whole process is fairly time consuming, with a reasonable amount of time required to fabricate the nanoparticles, to modify the substrate and then to attach nanoparticles to the modified substrate.

Electroless deposition is a process in which nanoparticles can be placed on a silicon surface without the need to prefabricate the particles or to modify the surface

beforehand. The process is very fast, and can be done using very low concentrations of metal. Thus, in this thesis the electroless deposition process was investigated as a way depositing metal, in this case gold, onto silicon. A few applications for this process were investigated. These included the effects of nanoparticles in Si-solar cells performance, and their applications as substrates for surface-enhanced Raman scattering (SERS).

According to a study done by British Petroleum (BP)[8], the global energy demands will increase by 40% between 2010 and 2030. This significant increase coincides with the growing need to reduce the use of fossil fuels, which currently make up >60%[9] of the energy produced today. Therefore in order to meet this demand, renewable energies, such as solar power, must be employed. However, for renewable energies to meet this demand, they will need to be more efficient than they are currently. In the case of solar energy, a large amount of research is being carried out aiming at making more and more efficient cells; however, these cells, such as multi-junction solar cells are extremely expensive and difficult to fabricate and are currently not viable for commercial or wide spread use. The most used solar cell type is the p-n junction silicon solar cell, which is so far the best cell in terms of cost versus electricity produced. However, they are still very expensive, so a great deal of research is going into solar cells that are less expensive to fabricate such as organic cells, dye sensitized solar cells, and thin-film solar cells.

In the case of thin-film solar cells, their low optical thickness is a large hindrance in their practicality for commercial use. Basically, they are too thin to allow all the photons to be absorbed as they pass through the cell. Plasmonic metal nanoparticles can be used to overcome this problem, due to their ability to scatter light, which will increase the optical thickness of the cells, allowing them to generate more electricity[10]. However,

thin-filmed Si solar cells are both difficult to make without the proper apparatus and expensive to buy in the small quantities required to test them. Therefore, standard silicon p-n junction solar cells were used in this thesis. If a solar cell that already has a high optical thickness shows enhanced performance after the deposition of gold nanoparticles, it is logical to conclude that the enhancements would also be present in the thin-film solar cells. Therefore, as a proof of concept, silicon p-n junction solar cells were modified with gold nanoparticles using the electroless deposition process in order to investigate their effects on power generation.

Plasmonic metal nanoparticles and nanostructures have also been of great interest in the field of medical research, particularly in chemical sensing[11]. Plasmonic nanoparticles are especially useful for this because of the enhancements that they provide to Raman signals, in a technique referred to as surface-enhanced Raman scattering (SERS)[12]. SERS uses the unique properties of surface plasmon resonance in order to increase the intensity of Raman scattering. This enhancement of Raman signal has been recorded to be as great as 10^{10} times in some special cases[13]. The large increase in the Raman scattering observed from molecules is special surface regions called hot spots. These are concentrated local electromagnetic fields resulting from the interaction between metallic nanostructures. In order to generate controllable and reproducible hot spots, nanostructures of plasmonic metals are organized onto a surface. These structures are generally made using lithography techniques, such a focused ion beam milling, combined with vapor deposition of the metal onto the surface. The vapor deposition is both expensive and time consuming, while electroless deposition is a very fast process

and it is comparatively inexpensive. Therefore, the use of electroless deposition will be investigated for the fabrication of nanostructures as possible SERS substrates.

Chapter 2 will go over the background of electroless deposition and plasmonics. Photovoltaics will then be discussed as well, with emphasis on the effects metal nanoparticles have on solar cells. Surface-enhanced Raman scattering will then be discussed, looking at simple examples involving single particles, and more complicated examples involving coupled nanostructures. Chapter 3 will go over the experimental procedures, materials, and equipment used throughout the research. Chapter 4 will go through the optimization of the electroless deposition process, as well as early size tuning experiments using K-gold. And Chapter 5 will discuss the effects of nanoparticles deposited on to silicon solar cells using electroless, while chapter 6 will go over the structure fabrication of nanodoughnuts and their potential as SERS substrates. The work will be concluded in Chapter 7 as well as a look at future possibilities.

Chapter 2: Background

2.1 Electroless Deposition:

Electroless deposition is a method used to reduce metal ions to a surface without the use of an applied potential. The classical use for electroless deposition is to deposit a metallic film onto a surface. There are two types of electroless deposition: autocatalytic deposition and galvanic displacement. Autocatalytic deposition involves deposition of metal using a redox reagent in the plating solution, which will only reduce the metal to the surface[14]. This method of electroless deposition will not be investigated in this thesis. The other method is galvanic displacement, in which metal ions are reduced to a surface by the oxidation of that same surface. The use of galvanic displacement was investigated in this thesis and any mention of electroless deposition hereafter will be referring to this technique[14]. The advantages of galvanic displacement over autocatalytic deposition is that the reaction rates are faster, the reactants are more simple and that silicon is easily reduced and is ideal for galvanic displacement.

Metallic nanoparticles immobilized on semiconductor surfaces, such as silicon, provide a promising platform for applications in several areas including circuits[14], measurements[15] and photovoltaics[10], to name just a few. As mentioned in Chapter 1, nanoparticles are typically immobilized onto a substrate using an organic molecule linker such as (3-aminopropyl)-triethoxysilane (APTMS)[6]. The substrate is modified using this molecule, where the silane group at the end of the molecule binds to the surface. This process is referred to as silanization[6]. For certain classes of silanes such as APTMS, the

opposite end of the chain is an amine, which will bind with metallic nanoparticles, thus immobilizing them to the surface.

To perform electroless deposition on silicon, the surface must first be treated with hydrofluoric acid (HF). This serves two purposes: first of all, the silicon surface must be oxidizable to enable the electroless reaction at the surface, thus the HF removes the SiO_2 protective layer from the Si surface. The second is that the HF will H-terminate the surface of the silicon[16], forming SiH, SiH_2 and SiH_3 groups on the surface. These H-terminated units are more reactive with respect to electroless deposition than bare silicon, as more electrons are produced when the H-terminated silicon is oxidized (discussed later on), and therefore more gold can be reduced to the surface. The initial deposition of a gold cation to the surface is the rate limiting step of the reaction, so H-terminating the silicon reduces this steps rate. It is believed that the initial electroless deposition takes place in areas on the silicon surface containing defects[14].

The electroless deposition of gold onto a silicon substrate will be investigated. Gold ions were reduced out of solution, forming nucleation sites at the silicon for additional gold deposition. The process resulted in dome-shaped gold nanoparticles on the surface of the silicon. The gold deposition was done using a plating solution containing chloroauric acid ($HAuCl_4$) and potassium fluoride (KF). Traditionally, the plating solution would have HF instead of KF. When the silicon surface is oxidized in the presence of HF, the fluorine anions react with the silicon oxide forming SiF_6^- that is released into the solution. This allows the electroless deposition to continue so that a metallic film can be produced[14,17]. However, since a film was not required, KF was used as a less effective substitute that is better suited for the production of nanoparticles.

However, since the concentration of the KF is fairly low (0.1 M), the fluorine anions are quickly used up and the surface of the silicon oxidizes, effectively stopping the electroless deposition. This allows for the growth of larger nanoparticles, but not the growth of a film[14].

The redox half reactions for this electroless process are shown below:

$$\mathbf{Si_{(s)} + 2H_2O_{(l)} \rightarrow SiO_{2(s)} + 4H^+_{(aq)} + 4\ e^-} \qquad \mathbf{(1)}$$

$$\mathbf{Au^{3+}_{(aq)} + 3e^- \rightarrow Au_{(s)}} \qquad \mathbf{(2)}$$

However, since the silicon surface has been H-terminated, the oxidization equation becomes:

$$\mathbf{SiH_{x(aq)} + 2H_2O_{(l)} \rightarrow SiO_{2(s)} + (4+x)H^+_{(aq)} + (4+x)e^-} \qquad \mathbf{(3)}$$

Where x can be 1, 2 or 3: for the mono-, di- and trihydride units. Further reactions will focus on the silicon dihydride unit for simplicity.

Also considering the fluorine anions in the solution the following reaction also takes place:

$$\mathbf{SiO_{2(s)} + 4H^+_{(aq)} + 6F^-_{(aq)} \rightarrow SiF_6^{2-}{}_{(aq)} + 2H_2O_{(l)}} \qquad \mathbf{(4)}$$

Fluorine anions and protons from both the $HAuCl_4$ and the oxidation of silicon react with the SiO_2 forming silicon hexafluoride anions and water.

Therefore the initial total reaction[14, 18] is:

$$\mathbf{2Au^{3+}_{(aq)} + SiH_{2(s)} + 6F^-_{(aq)} \rightarrow 2Au_{(s)} + SiF_6^{2-}{}_{(aq)} + 2H^+_{(aq)}} \qquad \mathbf{(5)}$$

The SiH_2 is oxidized to SiO_2 by water from the solution. The gold cations are then reduced to the surface using the electrons from the oxidation of the SiH_x. The SiO_2 is then removed from the surface by the fluorine anions and SiF_6^{2-} is dissolved into the solution.

Once the fluorine anions are used up the total reaction becomes:

$$\mathbf{2Au^{3+}_{(aq)} + SiH_{2(s)} + 2H_2O_{(l)} \rightarrow 2Au_{(s)} + SiO_{2(s)} + 6H^{+}_{(aq)}} \qquad \mathbf{(6)}$$

Since there are no fluorine anions present the solid SiO_2 stays on the surface. The electroless deposition stops once the surface has been oxidized.

2.2 Surface Plasmon Resonance:

Surface plasmon resonance is a phenomenon that occurs when an electron rich material (usually a metal) interacts with the electric field present in light. These metals are referred to as surface plasmas: materials that contain freely mobile charges[18]. When a plasma is exposed to a light source, usually a laser, at a certain frequency (called the plasmon frequency) the electrons in the surface plasma will begin to oscillate in response to the electric field of the light. Figure 2.2.1 shows this effect with spherical metal particles.

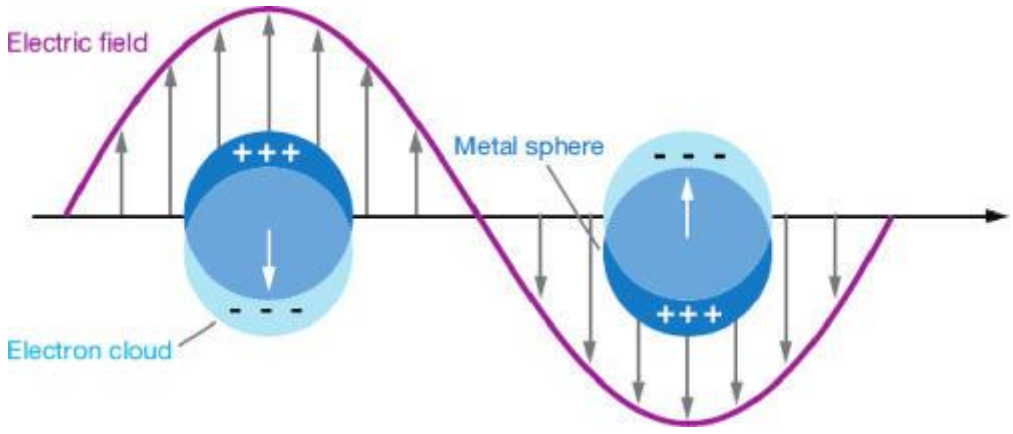

Figure 2.2.1 – Surface plasmon resonance for spherical metal particles[19]. Reused with permission, © Annual Reviews.

In Figure 2.2.1 the electric field (grey arrows) of the light, represented by the sinusoidal purple line, interacts with the electrons of the metal sphere. This causes a uniform shift of the electron within the sphere in the opposite direction of the electric field. The electrons are then pulled in the other direction by a restoring force that is the result of the positive charge distribution on the opposite end the particle. This creates an oscillation of electrons that produces a localized electric field at the particle. The magnetic field also has an effect on the plasmon resonance; however the contribution is so small that it is usually ignored. Figure 2.2.1 is an example of localized surface plasmon resonance (LSPR). The localized electric field is not uniform around the metal sphere, as the electrons oscillate along a specific axis. Figure 2.2.2 shows a simulation of the electric field intensity around a 60 nm gold nanoparticle.

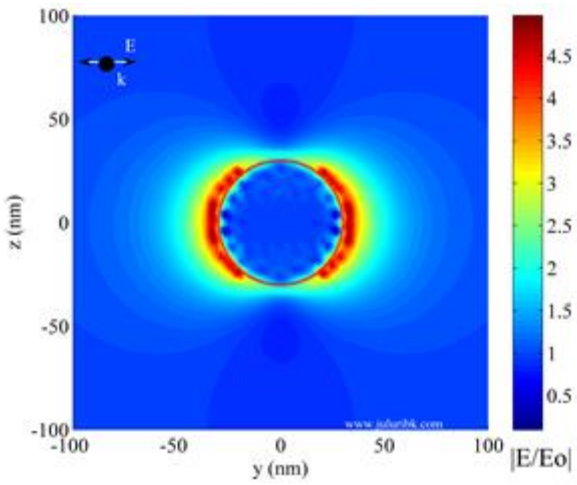

Figure 2.2.2 – Relative local electric field intensity simulation of a 60nm gold nanoparticles using a 532nm laser calculated using discrete dipole scattering approximation (DDSCAT)[20]. Reused with permission from juluribk.com.

In Figure 2.2.2 the electric field around the particle is colour coded based on the ratio of the local electric field due to the plasmonic resonance of the gold particle (E) and

the electric field without the nanoparticle (E_0). In Figure 2.2.2 the red areas represent the regions with the higher intensities, while the blue areas correspond to the weaker intensities. In the case of the single nanoparticle, the areas with the highest intensities are located on the opposite sides of the nanoparticle, showing the direction in which the electrons oscillate. These red regions are referred to as hot spots, and are of particular interest, in surface-enhanced Raman scattering. The circular shapes that make up the image in Figure 2.2.2 do not represent localized hot spots and are merely artifacts in the DDSCAT approximation.

2.3 Photovoltaics and Solar Cells:

The photovoltaic effect is defined as the ability of a material to convert light into electricity[21]. The photovoltaic effect is used in solar cells, to generate electricity. There are many varieties of solar cells, including p-n junction cells, thin film cells[22], organic cells[23,24], dye-sensitized solar cells[25,26] and more. For the purposes of this thesis, the photovoltaic effect of silicon p-n junction solar cells will be discussed. The basic setup for a silicon solar cell is shown in Figure 2.3.1.

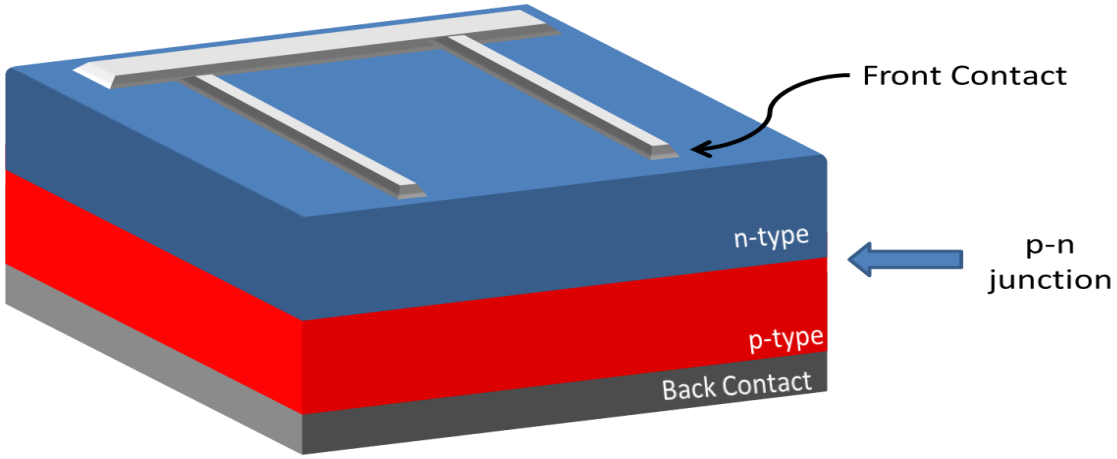

Figure 2.3.1 – Cartoon representation of a typical p-n junction solar cell. The different features starting from the top are the front contact, the n-type semiconductor, the p-type semiconductor and the back contact.

A silicon p-n junction solar cell (silicon solar cell or cell from this point on) is a semiconductor diode created from two layers of doped silicon, as well as a front contact for collecting electrons, and a back contact for the recombination of the electrons (these features will be discussed more later). The first or top layer of the cell is referred to as the n-type layer. An n-type semiconductor is created by doping a semiconductor, in this case silicon, with an atom that has more outer electrons than that of the semiconductor, such as phosphorus. Silicon's crystal lattice has a tetrahedral coordination, when it is doped with phosphorus a silicon atom is replaced in the tetrahedral unit cell. Phosphorus has 5 outer electrons, where silicon only has 4. Thus in order for the phosphorus to fit into the crystal lattice of the silicon, only 4 of phosphorus' electrons are required, leaving one "free" electron that is mobile throughout this layer. If the entire layer is doped with phosphorus, then there are many mobile electrons making this an n-type semiconductor. The second layer, or bottom layer of the solar cell, is a p-type semiconductor. A p-type semiconductor is created in a similar fashion as the n-type; however, instead of using an

atom with more outer electrons than the semiconductor, an atom with fewer outer electrons is used. Boron is used for this purpose, as it only has 3 out electrons. Similarly to the n-type, the boron replaces a silicon atom in the unit cell. Since silicon has 4 outer electrons, boron does not have enough electrons to fit into silicon's crystal lattice. This creates "holes" within the semiconductor which are viewed as positive mobile charges within the silicon, creating a p-type semiconductor[21]. Figure 2.3.1 shows only one configuration of a p-n junction solar cell. It is possible to switch the semiconductors, with the p-type being on top and the n-type below, however the n-type silicon is more costly to manufacture so it is typically used as the thin layer on top in order to reduce costs. The top layer needs to be thin so that the photons can penetrate the surface and reach the junction.

At the junction of these two types of semiconductors (p and n), electrons diffuse from the n-type layer into the p-type layer, and the holes diffuse from the p-type layer into the n-type layer. This diffusion causes the formation of an electric field at the junction[21]. This electric field can be seen in Figure 2.3.2.

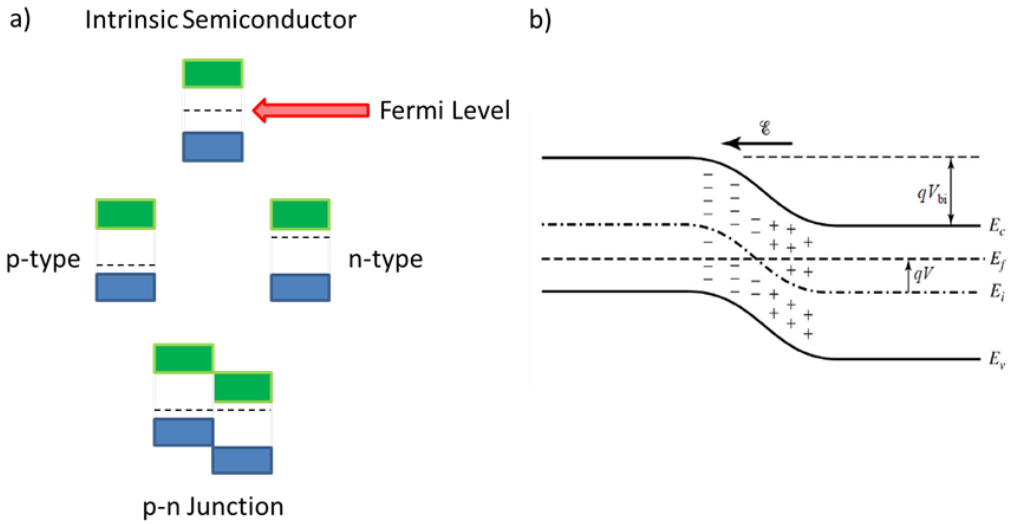

Figure 2.3.2 – a) Semiconductor band diagrams for an Intrinsic, p-type, n-type and p-n junction semiconductor. b) Band edge diagram from a p-n junction semiconductor[27]. Reused with permission, © John Wiley and Sons.

Figure 2.3.2a shows band diagrams for different types of doped semiconductors. The bands at the bottom of Figure 2.3.2a represent the valence band of the semiconductor (blue), while the band at the top represents the conduction band (green), and the dashed line represents the Fermi level of the material. This figure is only meant to show how individual semiconductors are combined to form the p-n junction band edge diagram, so other elements of the semiconductor bands (such as the donor and acceptor levels) are not included. The top of Figure 2.3.2a represents the band diagram for an intrinsic semiconductor, that has not been doped and the Fermi level is located directly in between the bands. The Fermi level is defined as the energy level where the probability of being occupied by an electron is 50%. The diagram on the right in Figure 2.3.2a represents the n-type semiconductor; since the n-type layer has more electrons than the intrinsic semiconductor the Fermi level is higher. Conversely, on the left side, since the p-type

semiconductor has fewer electrons than the intrinsic type, the Fermi level is lowered. At the bottom of Figure 2.3.2a is a diagram of the p-n junction. Since the Fermi level is related to a defined probability for the bulk material, this energy level will remain the same, but the bands of the different layers will shift, so that the energy of the valence band of the p-type semiconductor is higher than that of the n-type. This shift in bands yields the band edge diagram, seen in Figure 2.3.2b. The same features as the diagram in Figure 2.3.2a are observed in Figure 2.3.2b. E_v is the valence band energy level; E_c is the conduction band; and E_F being the Fermi level. E_i is the intrinsic level, and represents the middle energy between the valence and the conduction bands. In the center of the diagram, where the band energy shifts between the n-type and the p-type layer, the diffusion of the electrons into the p-type layer and the holes into the n-type layer takes place. This is referred to as the depletion region and represented by the + and – signs in Figure 2.3.2b. As mentioned before, the depletion region produces an electric field (E) pointed to the direction of the p-type side. This electric field is essential for the photovoltaic effect, and it allows solar cells to generate electricity. Figure 2.3.3 shows a cartoon representation of a solar cell under illumination.

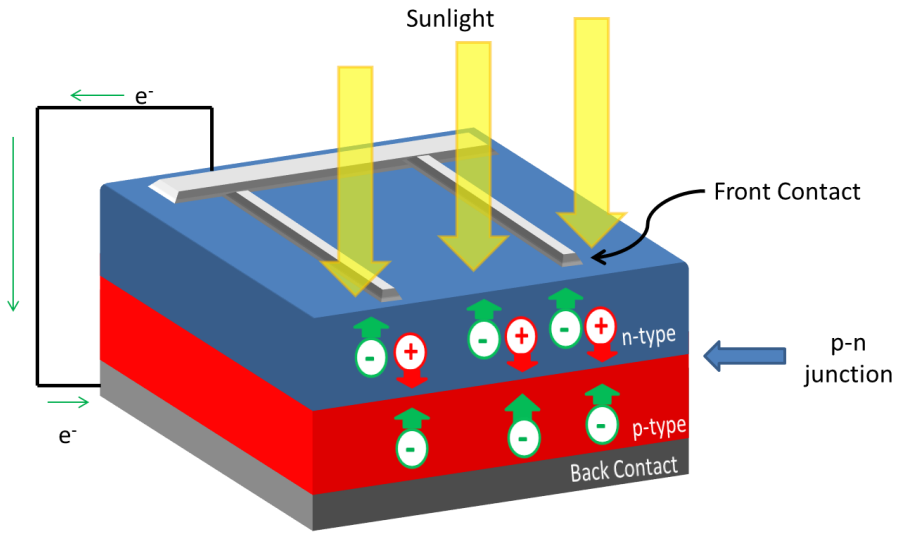

Figure 2.3.3 – Cartoon characterization of a solar under solar illumination.

In Figure 2.3.3, the downward pointing yellow arrows represent the photons produced by a light source (natural or artificial). When the light shines onto a solar cell, photons will penetrate the surface. The photon is then absorbed at the p-n junction creating an electron-hole pair (represented by the green circles and red circles respectively). Since there is an electric field at this junction, explained in Figure 2.3.2b, the electrons will be pushed away from the junction into the n-type layer. These electrons will be collected by the front contact attached to some form of load, causing a current to move through the load which can be used as electricity. The electrons then recombine with holes at the back contact, completing the circuit. This process can be repeated almost indefinitely, with most manufacturers guaranteeing 25 years of constant electricity generation[21].

2.4 Plasmonic Enhancement and Light Scattering in Silicon Solar Cells:

Within recent years there has been a significant amount of interest on the effects of plasmonic nanoparticles on the efficiency of solar cells[10,28,26,29]. In a review by H. Atwater and A. Polman[10], the different applications of plasmonic nanoparticles integrated into solar cells are discussed. The review[10] splits these applications into three categories: light trapping and scattering using nanoparticles at the surface of the solar cell, light trapping using localized surface plasmons from nanoparticles embedded in the solar cells, and light trapping by surface plasmon polariton excitation with particles located at the back contact at the interface with the semiconductor (see Figure 2.3.1). For the purpose of this thesis, only the enhancements due to nanoparticles on the surface of the solar cells will be discussed.

The principal factor responsible for the enhancements is the nanoparticles' ability to scatter light with very high efficiency. The light is preferentially scattered into the medium with the higher index of refraction[10,28]. This scattering is shown in Figure 2.4.1, which details the fraction of light scattered into the substrate based on the shape of the nanostructure.

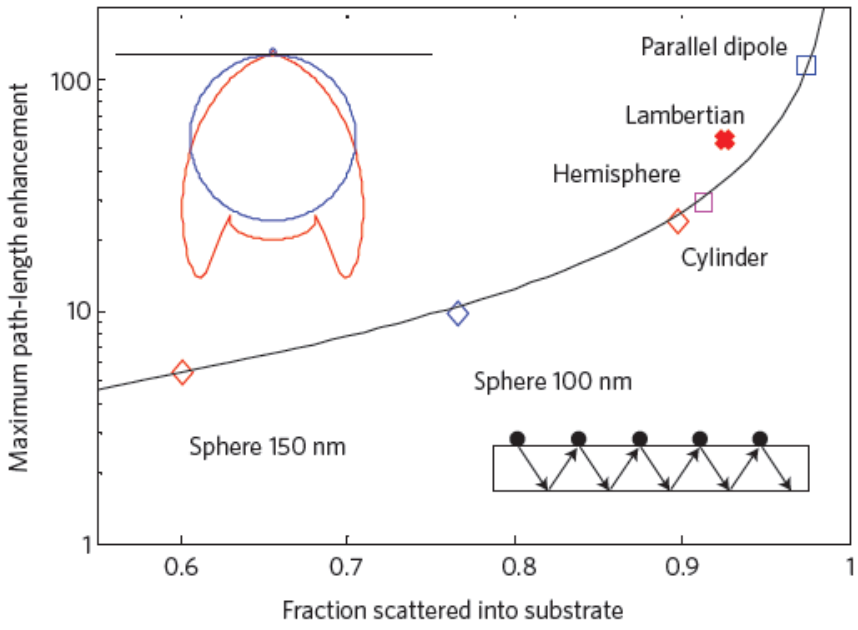

Figure 2.4.1 – Graph showing the fraction of light scattered into a substrate using different shapes of nanostructures[10]. Reused with permission, © Nature Publishing Group.

The nanoparticles deposited on the surface using the electroless deposition process are most likely hemispherical in shape; hence, from Figure 2.4.1 these particles are predicted to scatter >90% of the light into the substrate. Therefore, when light hits the particle, it will be scattered into the silicon solar cell. This phenomenon has a number of benefits. The first benefit being that the scattered light will be at greater angles then that of the original angle of the incidence. In Figure 2.4.1 the blue circle on the top left corner depicts a Lambertian scatterer, while the red outline shows the angular distribution of the scattered photons[10]. Figure 2.4.2 shows a cartoon representation of a solar cell with nanoparticles on the surface. The incident light is perpendicular to the surface of the cell in Figure 2.4.2, but the resultant scattered light is at different angles and preferentially directed into the device. This leads to an increase in the path length that effectively

increases the optical thickness of the cell; thus the number of photons absorbed to generate electricity also increases[10].

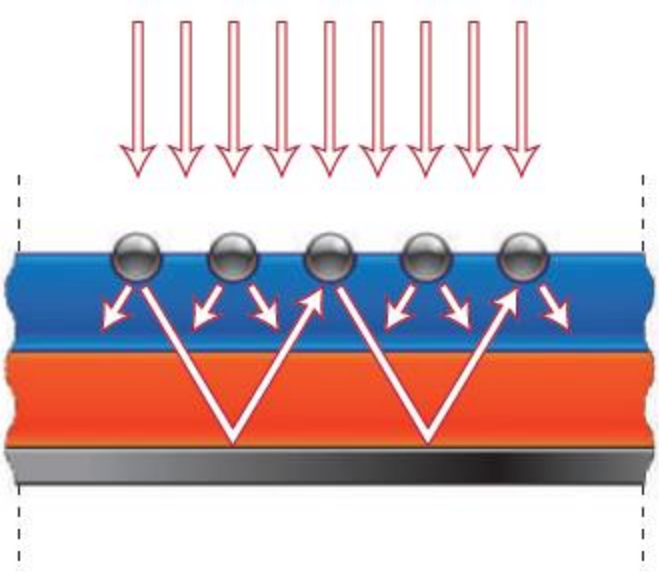

Figure 2.4.2 – Cartoon representation of a nanoparticle modified solar cell, and the nanoparticles influence the incident light[10]. Reused with permission, © Nature Publishing Group.

Another benefit to this increase in angle is that when combined with a reflective back contact, the path length of the light is increased further, making the optical thickness of the solar cell even greater[10]. In the case of the cells used for the purposes of this thesis, the back contact was primarily a silver based material. Silver is a very effective reflective surface in the visible region[30]. It has also been noted that a large portion of the scattered light is directed at angles greater than the critical angle of silicon (16°)[28]. Therefore, light reflected from the back contact will be reflected again at the surface of the solar cell, effectively trapping the light within the solar cell.

This technology is primarily useful in thin-film solar cells[31,32] that are very optically thin. Regular p-n junction solar cells were used in this research as a proof of

concept for the use of electroless deposited nanoparticles for the enhancement of solar cells in general.

2.5 Raman Spectroscopy and Surface Enhanced Raman Scattering:

Raman Spectroscopy is a technique that measures the light scattered inelastically by a molecule. For the most part, the light scattered by a molecule will be at the same energy as the original (incident) light source. This type of elastic scattering is referred to as Rayleigh scattering. However, during the scattering, molecules can also be excited to a higher vibrational energy state by using some energy from the incident photon. Alternatively, the molecule can transfer energy to the incident photon and relax to a lower vibrational energy level. These constitute inelastic scattering events and they are referred to as Stokes and anti-Stokes Raman scattering, respectively. For simplicity, only the Stokes scattering will be discussed throughout this section. This is an instantaneous process meaning that a photon does not have to be absorbed in order for the scattering to occur. The energy states diagram shown in Figure 2.5.1 helps on the explanation of Raman scattering. This image and the basic theory provided throughout this section are from ref.[30].

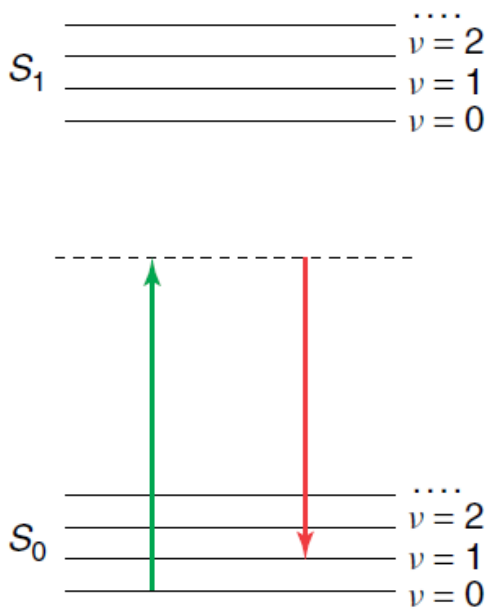

Figure 2.5.1 – Schematic Jablonski diagram depicting the electronic structure of the vibrational energy states of a molecule[30]. Reused with permission, © John Wiley and Sons.

In Figure 2.5.1, a photon (green arrow) interacts with the molecule exciting it into a virtual energy state, depicted by the dashed line, which is caused by the electric field from the light inducing an oscillating dipole. However when the molecule relaxes and the photon is scattered, the molecule falls into a higher vibrational energy state. Thus the scattered light (red arrow) has a lower energy than that of the original photon. The difference in the energies between the incident light and the scattered light (vibrational energy) is specific to the molecule and can be used to determine the identity of a species within a sample. Raman spectroscopy is an excellent technique for analyzing bulk materials. However, since the intensity of the scattered light is fairly low, it is not suited for analysis at low concentrations.

Surface enhanced Raman spectroscopy (SERS) is a technique used to increase the intensity of the Raman signal, so that it can be viewed at lower concentrations and even for a single molecule in special cases[33]. SERS is a very versatile technique that can be utilized in numerous different ways to detect types of materials.

In order for a material to be useful in SERS it must be able to undergo surface plasmon resonance (SPR), or to be more specific for nano-sized structures localized surface plasmon resonance (LSPR). As mentioned in section 2.2 on page 9, this is a phenomenon where light of certain frequencies cause the electrons within the material to oscillate with the electric field of the light, increasing the electric field at that specific location. This field localization is instrumental for the enhancement of the scattering signal. Electron rich metals are the most commonly used plasmonic materials, especially gold and silver. For the purposes of this thesis, gold will be used to discuss the SERS application. For the most part, silver nanoparticles are superior to gold in terms of their broad frequency range in which LSPR can be induced. However, in terms of the laser frequency range useful for SERS which is typically >600nm, gold nanoparticles can be tailored to give comparable enhancements to that obtained using silver. The chemical stability of the gold is an important advantage especially for SERS applications related to biological systems. The enhancements caused through SERS can be split into two contributions: chemical or charge transfer contributions and electromagnetic contribution. A large majority of the overall enhancement is from the electromagnetic portion. The chemical enhancements have been seen to improve the scattering signal by as much as a factor of 100[34]. However, these enhancements are molecule and substrate specific. In other words, the magnitude of the chemical contribution will vary depending on which

molecule is being tested and how it interacts with the substrate. Electromagnetic enhancements, on the other hand, take place regardless of which molecule is being tested. Therefore, for the purposes of this thesis, only the electromagnetic enhancements will be discussed at length.

As mentioned before the local electric field plays a crucial role in the increase of the scattering intensity. At resonance the magnitude of that electric field increases at the surface of the gold nanoparticle. This increase is given by the local field intensity enhancement factor (LFIEF), Equation 2.5.1 - below:

$$LFIEF\ (\omega) = \frac{|E(r)|^2}{|E_o(r)|^2} \qquad \textbf{Equation 2.5.1}$$

Thus the LFIEF is equal to the intensity of the electric field at a specific site on the plasmonic particle surface ($|E(r)|^2$) divided by the electric field intensity at the same site without the presence of the particle ($E_0(r)|^2$) at a specific frequency (ω). Therefore, if this was a simple emission mechanism with a laser focused on a molecule that is being manipulated by a plasmonic particle, then there would be an enhancement of LFIEF at a specific wavelength. This essentially increases the intensity of the incident light at a specific site, without having to increase the intensity of the laser. However, as mentioned previously the Raman effect is a two photon process, the photon of the laser and the scattered photon, which are at different frequencies. If the scattered photon is also under the effect of the plasmonic particle, its electric field will also be enhanced. Therefore the total enhancement factor (EF) for the scattering intensity is given by Equation 2.5.2:

$$EF = LFIEF(\omega_L) \times LFIEF(\omega_s) \qquad \textbf{Equation 2.5.2}$$

This equation shows that the local field of the nanoparticle enhances the incident laser light (ω_L), and the resultant scattered photon (ω_S) is also enhanced further by the local field, giving a much larger overall EF. As the difference between the LFIEF of the laser and the scattered light is fairly small, and the fact that the usually small difference in frequency does not affect the electric field to an appreciable extent (because of the broad plasmonic resonance), an approximation for the EF can be made given in Equation 2.5.3:

$$EF \cong LFIEF(\omega_L)^2 = \frac{|E(r)|^4}{|E_o(r)|^4} \qquad \textbf{Equation 2.5.3}$$

Therefore, the total enhancement factor is approximately equal to the LFIEF at the laser frequency squared. The EF can then be approximated to the local enhanced electric field to the power of four ($|E(r)|^4$) divided by the initial electric field to the power of four ($|E_0(r)|^4$), as shown in Equation 2.5.3. This is only a simple approximation of the enhancement and other factors such as proximity to a hot spot, and the polarizability of a specific molecule will change this approximation. However, this provides a fairly good estimation of the enhancement to a Raman signal that SERS will provide. SERS can provide scattering intensities up 10^{11} times larger than that of an normal Raman spectra, however a good SERS substrate is typically considered to have average enhancements of 10^{6}[(Ref 35)].

2.6 Surface Enhanced Raman Scattering from Organized Nanostructures:

It is also possible to increase the local field intensity, and thus the overall enhancement factor, through nano-patterning[1,30]. This is possible because organized structures provide a certain level of control over the efficiency of hot spots[30]. When

nanoparticles are randomly deposited on the surface, aggregation of the particles can occur which will cause natural SERS hot spots. However, since these are uncontrolled the enhancements are not reproducible. Therefore, organized nanostructures are used in order make sure that the hot spots are reproducible. One of the simplest examples to show this effect is to have two plasmonic cylinders or spheres in close proximity to each other as shown in Figure 2.6.1:

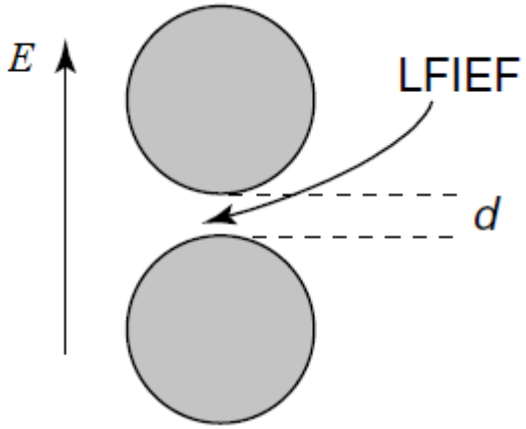

Figure 2.6.1 – Cartoon representation of two cylindrical plasmonic particles in close proximity[30]. Reused with permission, © John Wiley and Sons.

Figure 2.6.1 shows the two metallic particles with a distance d between them. The arrow depicts the direction of the electric field of the excitation. The basic idea here is that a LFIEF is induced in the area between them. The electric fields from both nanoparticles couple to produce a much larger enhancement factor. Figure 2.6.2 shows a numerical mapping of the predicted SERS intensities between two coupled particles:

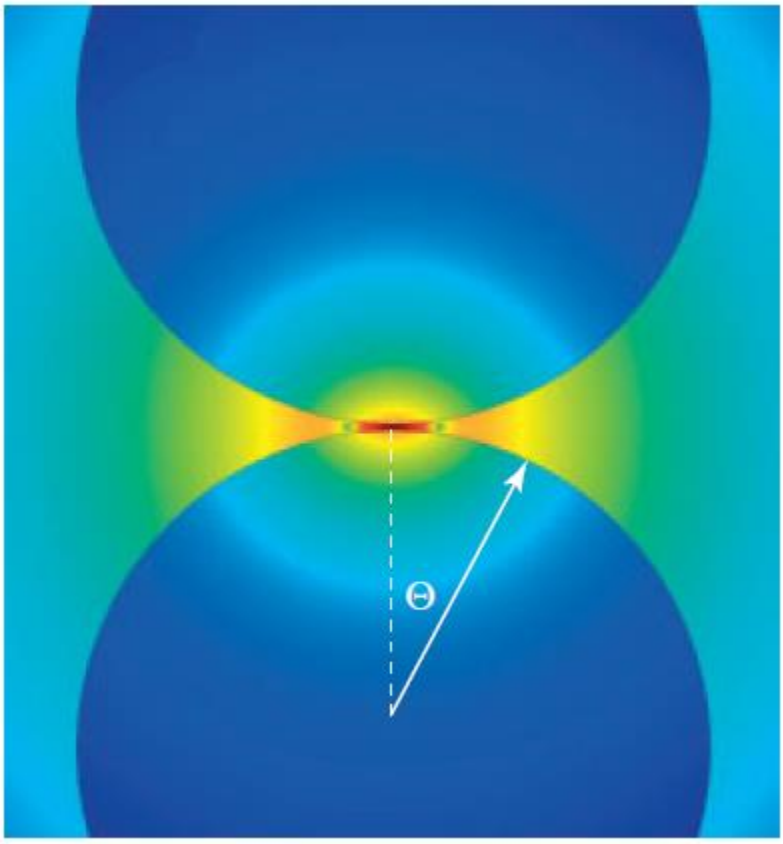

Figure 2.6.2 – Numerical mapping of the predicted SERS intensities showing the hot spot between two plasmonic nanoparticles[30]. Reused with permission, © John Wiley and Sons.

This image has been created using a logarithmic and false-colour intensity scale. The most intense LFIEF regions are depicted in red, as the intensity decreases the colour move through the colour scale to blue. As can be seen in Figure 2.6.2, the most intense signal is from the area directly in between the two particles. As the distance between the particles increases the intensity decreases. This loss in intensity can be predicted using the angle, Θ[30]. Thus the LFIEF, and the overall enhancement factor is much greater in between these particles than it is anywhere else around them.

Cylinders are not the only structures that can be used to produce hot spots, and a large amount of research has been done using different shapes and orientations[36,37 ,38,39]. Organized nanostructures are usually fabricated using a combination of focused ion beam lithography and vapour deposition.

Chapter 3: Experimental

3.1 Materials:

3.1.1 Chemicals:

Hydrogen tetrachloroaurate (III) trihydrate ($HAuCl_4 \bullet 3H_2O$, +99.9%) and potassium fluoride (KF, anhydrous powder, ≥99.99%), potassium carbonate (K_2CO_3, ACS reagent, ≥99.0%), acetone (ACS reagent, ≥99.5%) and rhodamine 6G dye were purchased from Sigma-Aldritch. Hydrofluoric acid (HF, 48-51% CA(S)) and sulfuric acid (H_2SO_4, ACS grade) were purchased from VWR International. Hydrochloric acid (HCl, reagent, A.C.S. 10^{th} ed.) was purchased from Anachemia. Ammonium hydroxide (NH_4OH, GR ACS) was purchased from EMD chemicals. Anhydrous ethyl alcohol (EtOH) was purchased from Commercial Alcohols. Hydrogen peroxide (H_2O_2, 30%) was purchased from CALEDON Laboratory Chemicals. Nitrogen gas (N_2, PP 4.8) was purchased from PRAXAIR. Colloidal Graphite (Product No. 16053, Isopropanol base) was purchased from Ted Pella, Inc. Ultrapure water was obtained using a Barnstead NANOpure Diamond water purification system.

3.1.2 Substrates:

Silicon wafers (n-type, 1-0-0, 356-406μm thickness, 1-10Ω resistivity) were purchased from Silicon Quest International. Solar Cells (200 ± 20μm thick, 25-57 Ω resistance) were manufactured from Yangzhou Huaer Solar-PV Technology Co.,Ltd..

3.2 Instrumentation:

3.2.1 Solar Cell Testing Setup:

The solar cell testing setup consisted of a Newport xenon lamp attached to a Newport 69907 power supply, a TECHTRON SI-RO-SPEC grating monochromator (0.5 µm grating, 380-850nm bandwidth, 10 nm resolution), a AUTOLAB PGSTAT30 potentiostat/galvanostat, and a desktop computer with the general purpose electrochemical system (V.4.9.$_{005}$) program for gathering results. This setup was used to perform two types of test, a spectral response test and a IV curve test. However a slight modification was performed in order to switch between tests. Figure 3.2.1 shows the setup for a spectral response test:

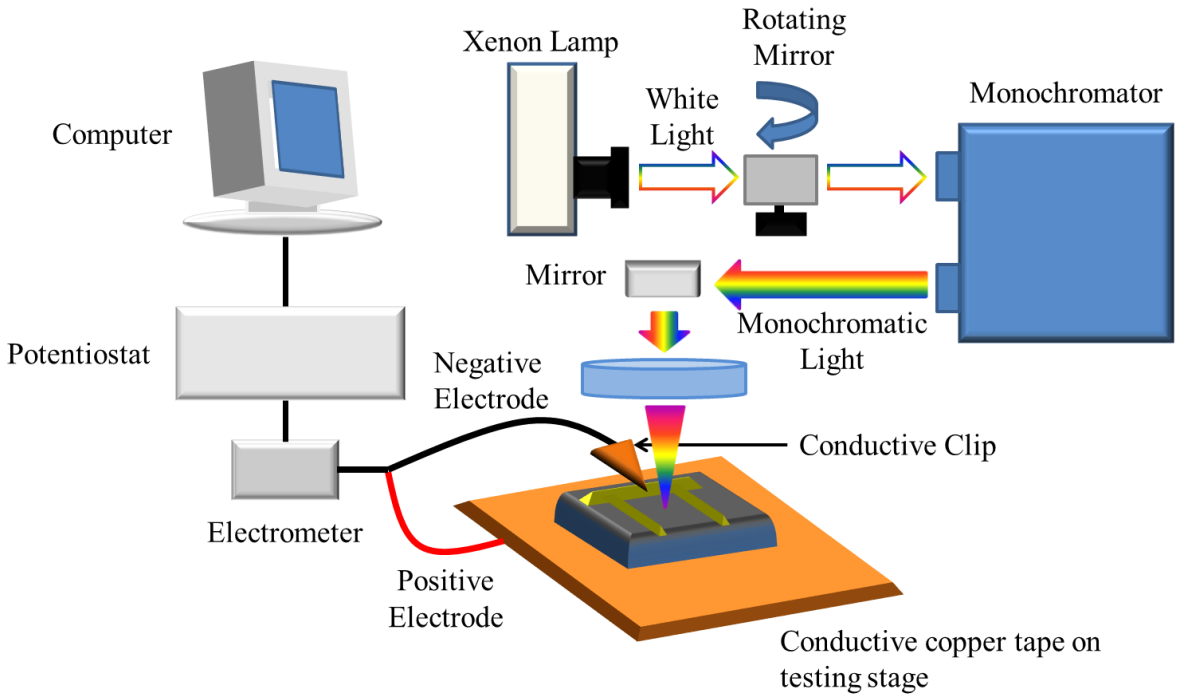

Figure 3.2.1 – Solar cell testing setup for a spectral response test.

In Figure 3.2.1 the white light is emitted from the xenon lamp, and the rotating mirror is positioned out of the lights path. The light is directed through the monochromator where it can be split into individual wavelengths for testing the spectral response. The monochromatic light is redirected with mirrors and focused through a lens onto the surface of the solar cell. The solar cell is fixed onto conductive copper tape in order to make the connection with the back contact. The solar cell is fixed onto the testing stage using a conductive clip that is placed on the front contact to complete the circuit. The electrodes are attached to both the copper tape, and the conductive clip to allow for testing.

Figure 3.2.2 shows the setup for the IV curve test:

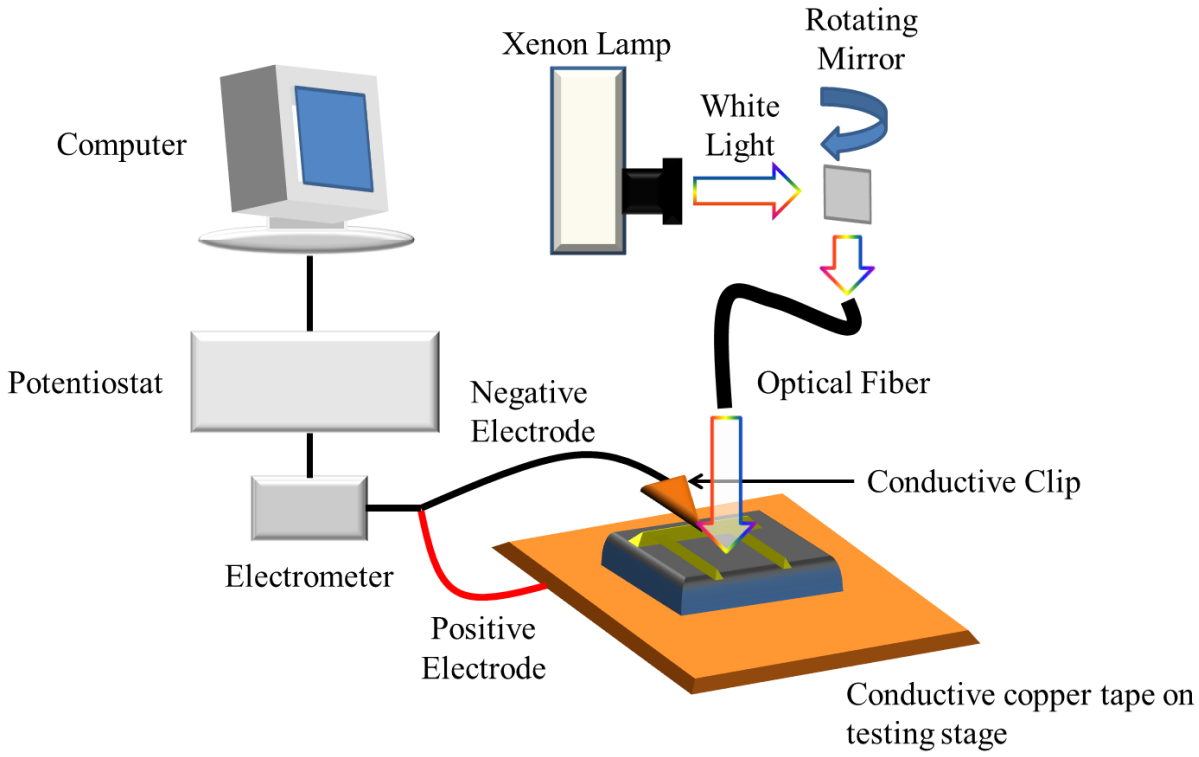

Figure 3.2.2 – Solar cell testing setup for a IV curve test.

The overall setup for the IV curve test is similar to that of the spectral response test. The key difference is that the rotating mirror is positioned in order to focus the white light into an optical fiber (using a lens). The solar cell is positioned underneath the optical fiber. The setup of the cell, and the electrodes are the same as the spectral response test.

3.3 Methods:

3.3.1 Electroless Procedures:

3.3.1.1 RCA Procedure:

Gold nanoparticles were deposited onto silicon using the Radio Corporation of America (RCA) method[6] of cleaning and treatment in a plating solution. Silicon wafers were cut into approximately 1.5cm x 1.5cm square chips. A silicon chip was then dipped in a boiling solution of 1 part NH_4OH, 1 part H_2O_2 and 5 parts ultrapure water. After ten minutes the chip was removed and rinsed with ultrapure water and dried with N_2. Once dried the chip was immediately placed in a solution 1% HF in ultrapure water for 30 seconds. The chip was then removed rinsed with ultrapure water, dried in N_2 and dipped in a solution of 1 part HCl, 1 part H_2O_2 and 6 parts ultrapure water for 10 minutes. The chips were then removed, and rinsed with ultrapure water, dried with N_2 and immediately placed in another solution of 1% HF in water for 2 minutes. After this the chips were rinsed with ultrapure water and dried under N_2 again. Once dry, the chips were dipped in a plating solution of 1mM KF and 0.1M $HAuCl_4$ for a variable amount of time at variable temperature. Once the deposition was complete the chip was removed and rinsed in

ultrapure water and then dried with N_2. The chips were then stored in air, and later characterized by SEM.

3.3.1.2 Drop-wise Procedure:

Gold nanoparticles were deposited onto silicon using a drop-wise electroless procedure. Silicon wafers were cut into approximately 1.5cm x 1.5cm chips. Silicon solar cells were pre-cut using a laser in 1.5cm x 1.5cm units. A solution of 1% HF was added drop-wise to the surface of the silicon chip or solar cell until completely covered. The HF was then rinsed with ultrapure water after a variable amount of time and dried under N_2. The sample was then either dipped in a plating solution of 1mM KF and 0.1M $HAuCl_4$ or the plating solution was added drop-wise to the surface. The plating solution was typically heated to 30°C. The plating solution could also be diluted using ultrapure water. After a variable deposition time the sample was rinsed in ultrapure water and dried under N_2. The treated silicon chips or solar cells were then stored in air until further testing was done.

3.3.1.3 Nanodoughnut Deposition:

Electroless deposition was used to deposit nano-doughnut structures onto the surface of silicon. Nano-hole arrays were made in PMMA coating a silicon chip using the focused ion beam technique. This sample was then dipped in a solution of 1% HF in water for 2 minutes. Afterwards the sample was removed and rinsed in ultrapure water and dried under N_2. The sample was then immediately dipped into a plating solution

(1mM KF and 0.1M $HAuCl_4$ in water) heated to 30°C for 2 minutes. The sample was then removed and rinsed with ultrapure water, dried under N_2 and stored for further testing.

3.3.2 K-Gold Nanoparticle Growth:

3.3.2.1 Preparation of K-Gold Solution:

K-gold solution[40,41] was prepared by dissolving 0.0500g of K_2CO_3 in 197 mL of ultrapure water while stirring. A K-gold solution is a solution of $Au(OH)_2$ made using K_2CO_3. Solution was stirred for 15 minutes to ensure all K_2CO_3 was dissolved. Once dissolved 3.750 mL of a 20 mM solution of $HAuCl_4$ in water was added. The solution was stirred in the dark for 30 minutes where it became colourless, which shows the production of $Au(OH)_3$[40,41]. The K-gold solution was stored in the dark for 15 hours to allow it to reach the proper pH (7.5-8), which helps to avoid external nucleation. External nucleation occurs when the gold hydroxide reduces out of solution forming nanoparticles in the solution. The K-gold solution was stored in the dark until use.

3.3.2.2 K-Gold Growth of Seeded Nanoparticles:

Gold nanoparticles were deposited onto the surface of silicon (either silicon chip or solar cell, see section 3.3.1on page 31) and used as seeds for K-gold growth. The silicon sample was placed in a beaker with 10.6 mL of K-gold solution in the dark. To start the growth 26 µL of formaldehyde was added to the K-gold solution, this is used to

reduce the $Au(OH)_3$ in the K-Gold solution to the seeded nanoparticles[40,41]. The particles were grown for variable times under gentle stirring. After the growth the silicon sample was removed and washed with ultrapure water and dried under N_2. The silicon sample was stored for future testing.

3.3.3 Solar Cells Preparation:

The silicon solar cells were precut into 1.5cm x 1.5cm by the manufacturer using a laser. The surface of the silicon cells were polished by the manufacturer, Yangzhou Huaer Solar-PV Technology Co., Ltd. This was done to ensure a greater correlation in the results between the silicon used for optimizing the electroless deposition procedure and the cells. The cells also came absent of any front contact, as the electroless procedures damages these structures. When the front contact is damaged the resistance of the cell increases which affects the reproducibility of the measurements done on the cells after nanoparticles are deposited. A gold front contact was added to the surface using vapour deposition, as can be seen in Figure 3.3.1.

a) b)

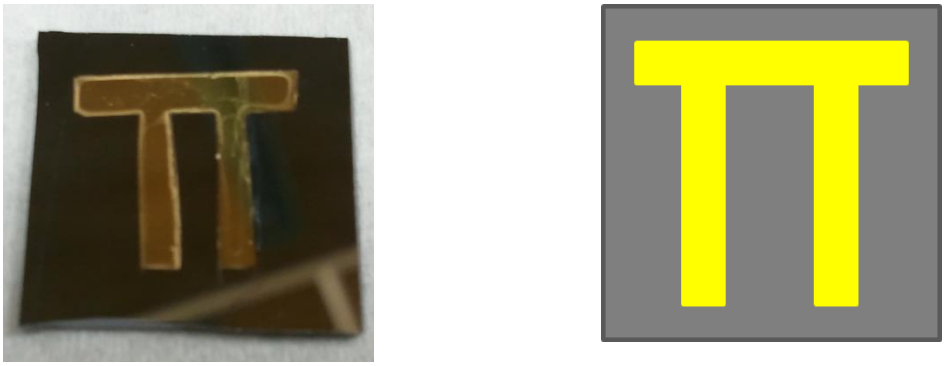

Figure 3.3.1 – A picture (a) and a cartoon representation (b) of the gold front contact, deposited by vapour deposition.

Gold was used because of its stability and its relative inertness during the electroless procedure used for solar cells. The "Pi" shape of the contact was chosen so that the light can be focused between the "fingers" allowing for better electron collection, and the top of the structure allows a large area for connection to the potentiostat for testing of the cells. The gold deposited on the surface does create a metal-semiconductor interface, which is meant to act as an ohmic contact, however it is possible that it could act as a Schottky diode. The gold structure was 100 nm thick. The resistance of a cell before the addition of the gold structure was ~32 kΩ, whereas the resistance of the cell using the vapour deposited front contact was ~3 kΩ, which is an order of magnitude lower. This is definitely an improvement over the cell without a front contact, however the resistance is much greater than the cells from the same company with factory applied front contacts (25-57 Ω). The resistance was measured using a Wavetek 35XL multimeter, giving the high resistance shown above in one direction, and an infinite

resistance reading in the other. The results gained from these devices do not suggest the high resistance effected the currents measured. The cells were covered and stored in air for future testing.

3.3.4 Solar Cells Testing:

3.3.4.1 Solar Cell Testing Setup:

Solar Cells were tested using an AUTOLAB-potentiostat/galvanostat with the General Purpose Electrochemical System (V.4.9.$_{005}$). The cell was fixed to the testing stage using a conductive clip. This clip is positioned on the front contact, which allows for electron collection from the cell. The surface of the testing stage is covered in conductive copper tape in order to complete the circuit with the back contact. To connect the cell to the potentiostat, alligator clips are attached to both the clip and the copper tape. The testing stage is then positioned beneath the appropriate light source. The light source will vary depending on the test being performed. Two different types of measurements were performed: a spectral response using the setup shown in Figure 3.2.1and an IV curve using the setup shown in Figure 3.2.2.

3.3.4.2 Spectral Response:

A spectral response measures the current output of a cell at specific wavelengths. For this measurement the testing stage is positioned under monochromatic light. The light is positioned between the fingers of the front contact for maximum current collection. Wavelengths of light were tested in 10 nm increments from 350 nm – 900nm. A <510 nm

filter is placed before the monochromator at 550 nm, in order to ensure the light is monchromatic at higher wavelengths, as lower wavelengths are not filtered out by this specific monochromator at higher wavelengths. During the test, current is measured in 0.2 second intervals. A shutter is used to block the light during the test. The measurement starts with the cell covered by the shutter, after ~5 seconds the shutter is opened and the cell is exposed to light. After ~5 seconds the shutter is closed and the wavelength is adjusted. A time frame of 5 seconds was used because it gave a suitable number of data points to average out any small fluctuations in the current. The shutter was necessary because without it the current generated by the wavelengths between the measurements would also be displayed. This would make it difficult to determine the current generated at specific wavelengths. Once adjusted, the shutter is opened and the cell is exposed to light again for another ~5 seconds. This process is repeated until 900 nm. This gives a graph of current with respect to time as depicted in Figure 3.3.2.

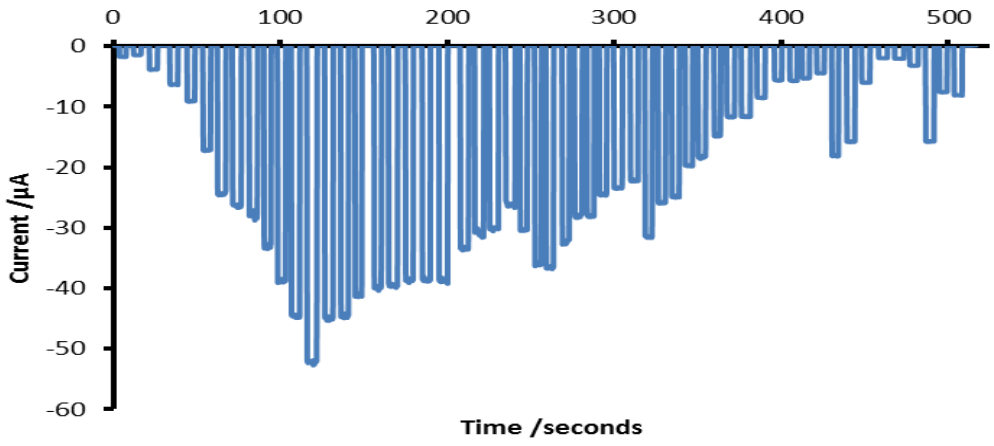

Figure 3.3.2 – Raw data for a spectral response showing the current at specific times while changing the wavelengths.

This graph is then converted into a graph of current with respect to wavelength shown in Figure 3.3.3.

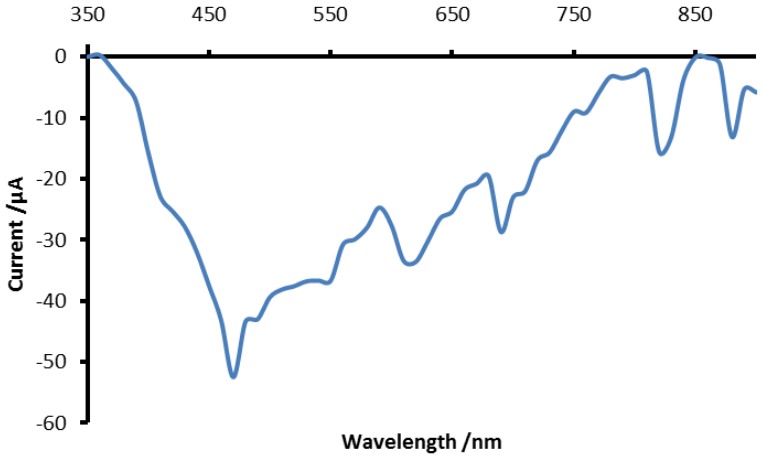

Figure 3.3.3 – Spectral response of a solar cell.

As each signal from Figure 3.3.2 relates to a certain wavelength, the peak is averaged and graphed against these wavelengths. This measurement can be repeated in order to smooth the curve to provide a more accurate measurement.

3.3.4.3 IV Curves:

An IV curve is a measurement that is used to determine the short-circuit current (I_{sc}), open-circuit potential (V_{oc}), optimal power ($P_{optimal}$), maximum power (P_{max}) and fill factor (FF) of the solar cell. The short-circuit current is the characteristic current of the solar cell when there is no applied voltage. Conversely, the open-circuit voltage is the voltage of the cell when there is no current. The product of the short-circuit current and the open-circuit voltage is the optimal power of the solar cell, which is a theoretical value that the cell can never reach. The maximum power of the solar cell is the largest value of

the current multiplied by the voltage in the IV curve. The fill factor is the ratio of the maximum power of the cell and the optimal power, which gives a value for the efficiency of the cell based on its theoretical optimal power[21]. This measurement is achieved by applying a voltage to the solar cell and measuring the current. For this measurement the testing stage is placed under a white light source, which comes directly from the xenon lamp. The voltage starts at -0.3 V and increases with a scan rate of 0.01998 V/s until it reaches 0.5V. Current is recorded at each voltage increment. This produces a graph of current with respect to voltage (I-V curve-Figure 3.3.4). This measurement is done twice, once while the cell is in complete darkness, and once while the cell is exposed to white light. The dark curve gives the diode characteristic of the solar cell when it is not illuminated, while the white curve is used to find the all the information listed above[21]. Figure 3.3.4 shows these two curves and the information that can be determined with them.

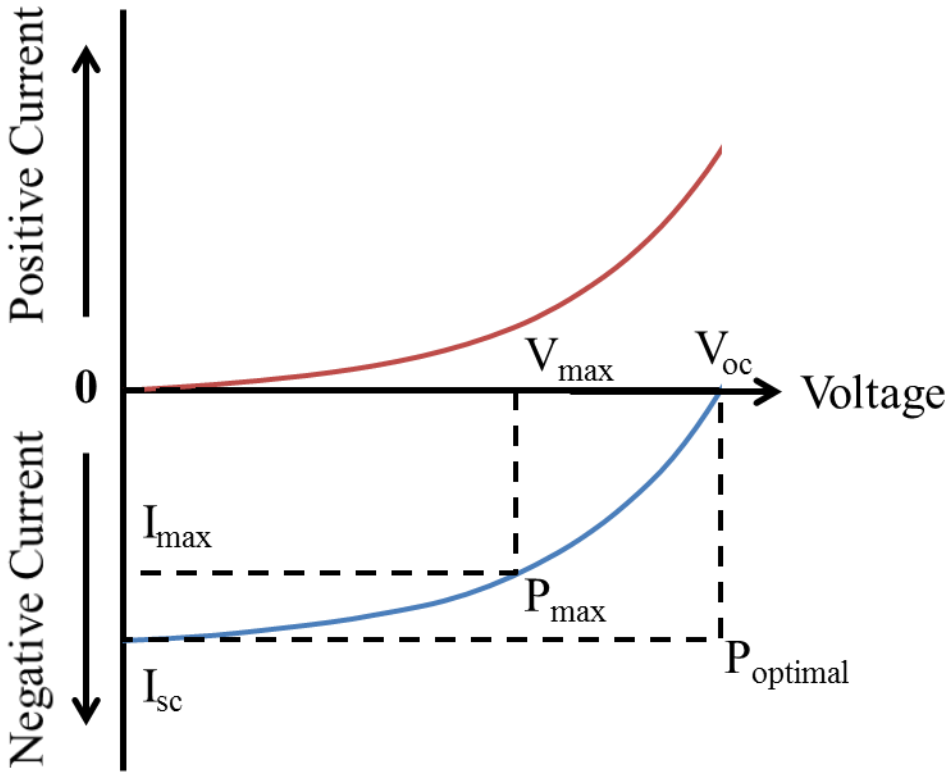

Figure 3.3.4 – IV characteristic curves of a solar cell, under no illumination (red line) and under illumination (blue line).

3.3.5 Scanning Electron Microscope:

Silicon samples, either silicon chips or solar cells, were either clamped to the stage, or adhered to the stage using carbon paste, or both. The stage was adjusted to a height of ~2.9 cm with the stage holder. The sample was placed into the exchange chamber, where it was pumped down and inserted into a cold field emission Hitachi S-4800 Scanning Electron Microscope. The working distance of the sample was adjusted to ~3.1 mm to ~4 mm from the electron beam. Images were recorded using an accelerated

voltage of 1 kV at a scanning current of 10 µA. Once finished the sample was returned to the home working distance (8 mm) and removed from the SEM.

3.3.6 Reflectance:

The reflectance curves of the silicon samples, either silicon chips or solar cells, were recorded using a PerkinElmer Lambda 1050 UV/VIS/NIR Spectrometer using the Universal Reflectance Accessory. Reflectivity was recorded from 250 nm – 800 nm. The samples were first run as blank silicon surfaces, which would then be gold nanoparticle modified using the electroless procedure. The reflectance was then taken of the modified sample, which were compared with their unmodified blanks. Figure 3.3.5 shows a reflectance measurement of a silicon surface:

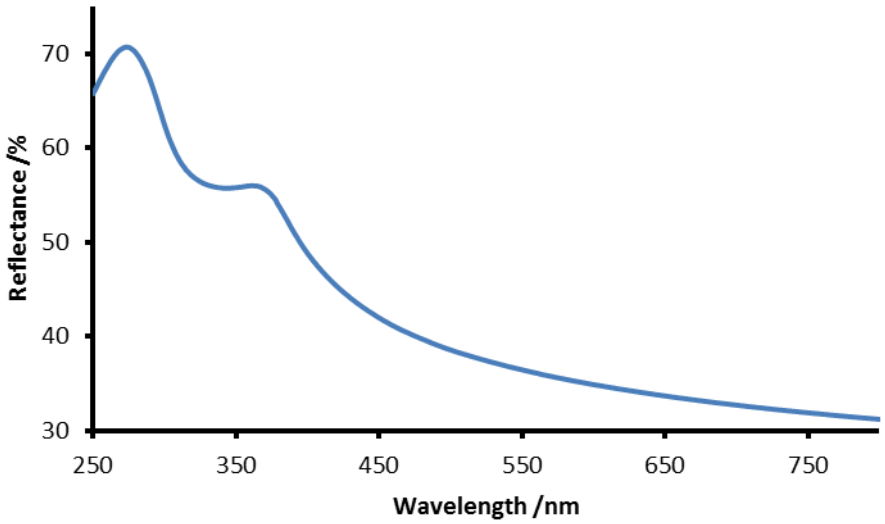

Figure 3.3.5 – Reflectance measurement of a blank silicon surface.

3.3.7 Surface Enhanced Raman Spectroscopy Measurement:

Gold nano-doughnut arrays were submerged in a 10 µmol/L solution of rhodamine 6G in ultrapure water. Raman signal was taken using RENISHAW inVia Raman Microscope with a ANDOR TECHNOLGY iDus (Model No. DU401A-BR-DD) camera, and a RENISHAW RL633 Laser, with a water submersion (63x) lens. The laser was focused on an individual nano-doughnut for each test. Each test was performed using 1 second of laser exposure, with 1 second acquisition time, and 1 accumulation at 0.5% laser power. Figure 3.3.6 shows a Raman signal of rhodamine 6G on a nano-doughnut:

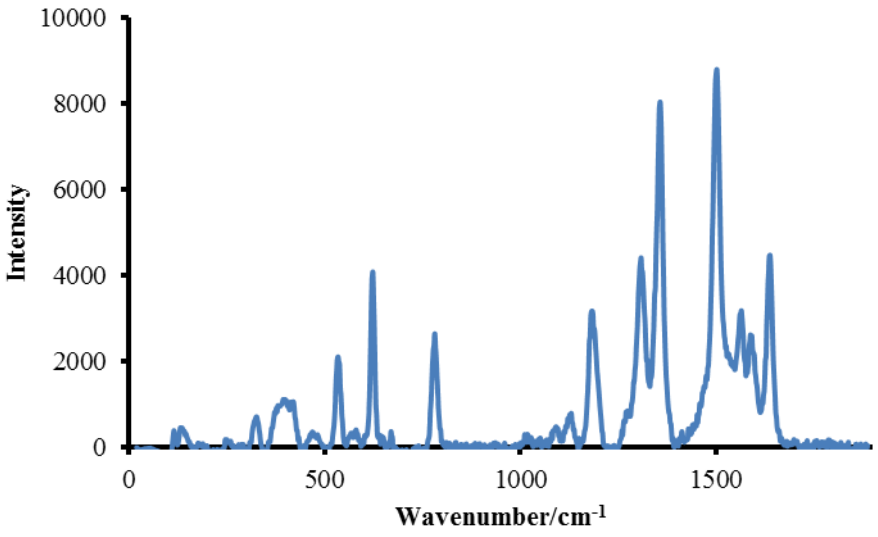

Figure 3.3.6 – Raman signal of rhodamine 6G at a nano-doughnut site in a 10 µmol/L solution. Correlating to spectra shown in ref[42]

The mapping was performed on the entire nano-doughnut array. A mapping is taken by recording the Raman signals in a grid segmented area. Each segment of the grid is taken individually, recording the signal in the first position, followed by a small movement over an adjacent segment in the grid where the Raman signal is taken again. This continues until Raman signal of the each segment of the grid has been taken. The

intensity of each of the segments are then colour coded using a logarithmic or false colour scale, which compares all the signals based on their intensity. Areas with high signal intensity are coloured red, the areas with weaker signals are labelled using colours that are lower in the colour scale moving from red to blue, and black for areas with almost next to no intensity. These signals can then be ordered to construct an image showing where the highest Raman intensities are located on the surface,

3.3.8 Focused Ion Beam:

The nanohole pattern for nanodoughnut deposition was milled using a Hitachi FB-2100 focused ion beam system. The holes were patterned in poly (methyl methacrylate) spin coated on a silicon substrate, of thickness ~500nm. The pattern was designed using a Bitmap program, and entered into the FIBs operating system. The pattern was fabricated using a 5k times magnification, a 40-0-30 beam (40kV accelerating voltage, condenser lens off, 30 micrometer diameter aperture), 13.5 pA current (at sample), 10 microseconds/pixel dwell time, and 100-250 passes. The focused ion beam milling was performed by Dr. Mohammed Rahman, a former visiting scientist at the Brolo group.

Chapter 4: Electroless Investigation

4.1 Electroless Deposition:

Although the chosen electroless method has been well established[14 ,16], an investigation of the different aspects of the procedure was necessary in order to tailor the reaction to yield the structures needed for the goals of this thesis. The results needed were a small distribution of particle size, an ability to adjust particle coverage on the surface, to be able to increase the size of the nanoparticles, and the capacity to perform the experiment on a silicon solar cell without affecting the performance of the cell by damaging either the front or the back contacts. In order to achieve these requirements, different criteria within the original reaction were studied or altered. These include: deposition time, temperature, the concentration of the plating solution, the amount of time the silicon surface was exposed to HF, the use of a K-Gold solution to grow the seeded nanoparticles, and the purposes of the different steps used in the reaction. Originally, this work was done in order to optimize the electroless process and yield the best results in terms of size distribution and surface coverage. However, during the investigation it became apparent that the variable components of the electroless procedure were not the only contributing factors to the quality of the deposition. The surface of the silicon, primarily mechanical defects on the surface, also contributes to the quality and coverage of the gold nanoparticles deposited. Therefore, due to this uncontrollable aspect, the goal of this research switched from optimization to an investigation of the effect of the variable conditions. This knowledge was used in order to tailor the electroless procedure used in the later experiments.

4.2 Time Investigation:

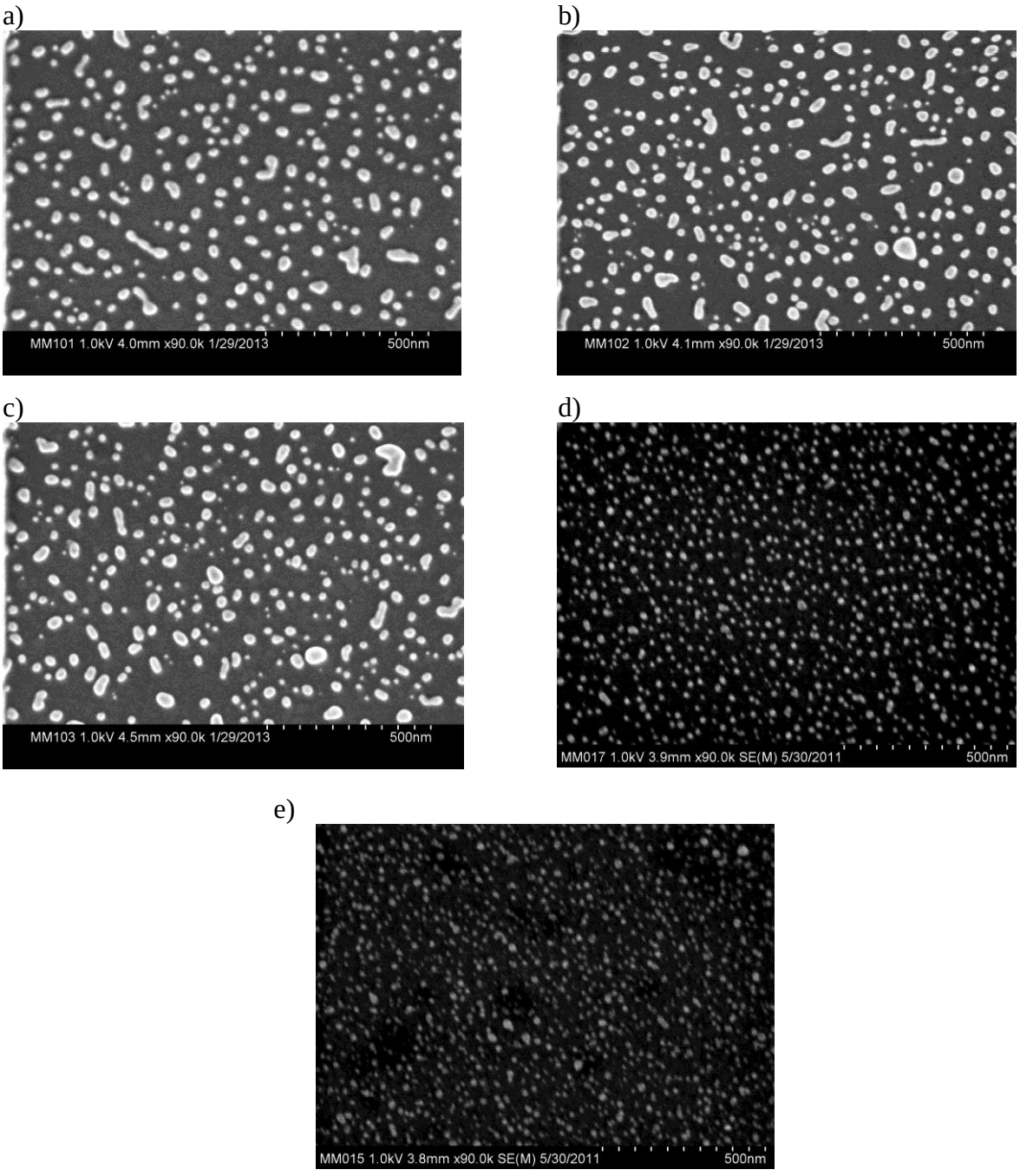

Figure 4.2.1 – SEM images of silicon surfaces after the standard electroless procedure at room temperature (~20°C) for (a) 15 seconds, (b) 30 seconds, (c) 1 minute, (d) 2 minutes and (e) 5 minutes.

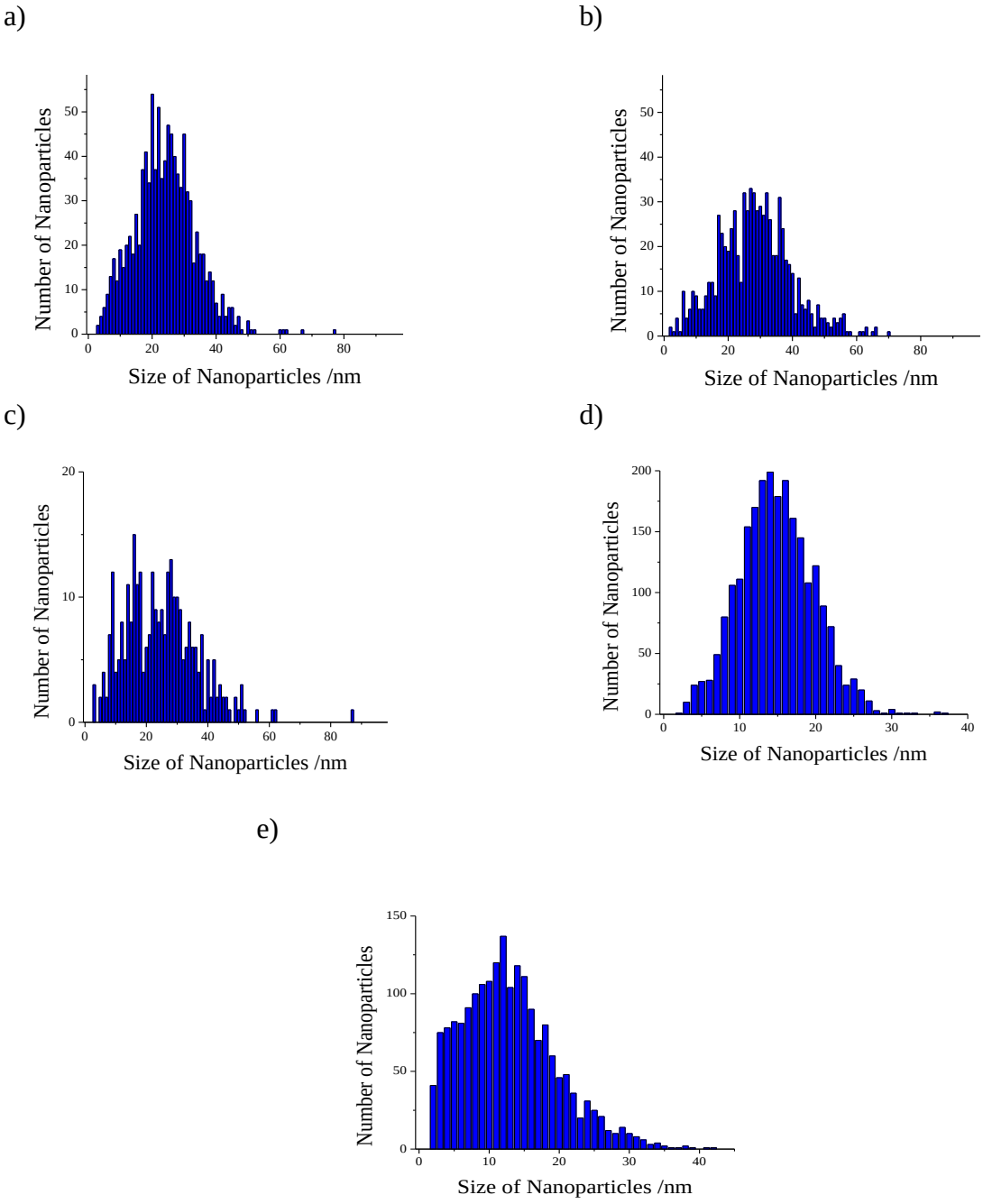

Figure 4.2.2 – Histograms of gold nanoparticles deposited onto silicon surfaces using the standard electroless procedure at room temperature (~20°C) for (a) 15 seconds, (b) 30 seconds, (c) 1 minute, (d) 2 minutes and (e) 5 minutes, created using the summation of 3 SEM images taken at different locations on the surface.

Time /s	Average Size /nm	Standard Deviation /nm	Standard Error of the Mean /nm	Average Particles/μm^2	Standard Deviation of Particles/μm^2	Percent of Surface Covered /%	Standard Deviation in Coverage /%
15	25	9	0.53	258	78	14	1.3
30	30	11	0.71	192	20	16	2.4
60	26	12	0.69	200	-	13	-
120	16	5	0.17	581	51	13	1.2
300	14	6	0.26	656	29	12	3

Table 4.2.1 – Table of time dependent results summarizing the particles size and surface coverage.

Figure 4.2.1 shows silicon surfaces that were treated using the RCA method (outlined in Section 3.3.1.1 on page 31). The conditions used in the experiment were a 2 minute dip in the HF, and variable deposition times in a concentrated plating solution at room temperature (~20°C). The deposition times used were a) 15 seconds, b) 30 seconds, c) 1 minute, d) 2 minutes, and e) 5 minutes. This experiment was performed in order to investigate the effects of longer deposition times on the gold nanoparticles deposited.

Figure 4.2.2 shows the corresponding size distribution histograms for the surfaces of the samples shown in Figure 4.2.1 and Table 4.2.1 summarizes to the results gained from the experiment. From Table 4.2.1, it can be determined that the average size of the nanoparticles is not significantly affected by changes in deposition time, at least in this range. The decrease in size between the 60 second sample and the 120 second sample is most likely due to the fact the silicon chips used for the experiment came from a different bulk silicon sample, as the original silicon sample had been used up. The 15 second, 30 second and 60 second samples all shared the same bulk parent material, whereas the 120

second and 300 second samples shared a different parent material. This shows the surface of the silicon samples effects how the nanoparticles are deposited onto the surface.

However, the average coverage (given in particles/μm^2 and percent of surface covered) from Table 4.2.1 does seem to change with deposition time. The average coverage was determined by averaging the number of particles/μm^2 different SEM images taken at different locations on the surface. The percent of the surface covered was created by taking the summation of the area of all particles in an SEM image and dividing it by the total area of that image, this was done for 3 images and averaged. For the most part, as the deposition time increases, so too does the particle coverage. The 15 second sample, shown in Figure 4.2.1a, has a larger particle count than that of the 30 second and 60 second samples (Figure 4.2.1b and Figure 4.2.1c, respectively). This is not what is expected by looking at the rest of the data that clearly shows an increase in particle coverage as deposition time increases, and is most likely due to the surface of this particular silicon sample. This has to do with the nature of the electroless process. Since the surface is a part of the reaction, it plays a large role in how the gold will be deposited on the surface. As mentioned in the section 2.1 on page 6, the initial step of the reaction is the gold reducing to the surface, primarily to areas containing defects[14]. If a sample has more mechanical defect areas, then more particles will be adsorbed to the surface. The silicon used is n-type (Section 3.1.2 on page 28), and has been doped with phosphorus, the doping procedure creates mechanical defects and impurities on the surface of the substrate. If an area of the bulk sample was more heavily doped or has more defect areas than the rest of the surface, more nanoparticles would be deposited during the electroless process. However, the percent coverage of the 30 second sample looks to be slightly

higher than the 15 second sample so more gold may have been deposited onto the surface, even though there are fewer particles.

In the 30 second and higher samples, there is an apparent increase in particle coverage as deposition time increases. However looking at the standard deviation of the particle coverage for the 120 second and 300 second samples, there is likely very little change in the surface coverage as they fall with each other's range. Thus, even though the deposition times of these samples are very different there is very little change in the number of particles deposited onto the surface. This is most likely due to a finite number of active sites present on the surface once it has been saturated in nanoparticles, this provides a plateau for the amount of particles that can be deposited on the surface under these conditions[14,16].

Therefore, from this data it can be determined that overall the longer the silicon surface is exposed to the plating solution the more nanoparticles will be deposited onto the surface. There is however a plateau that can be reached, and thus the coverage does not increase indefinitely.

4.3 Temperature Investigation:

a)

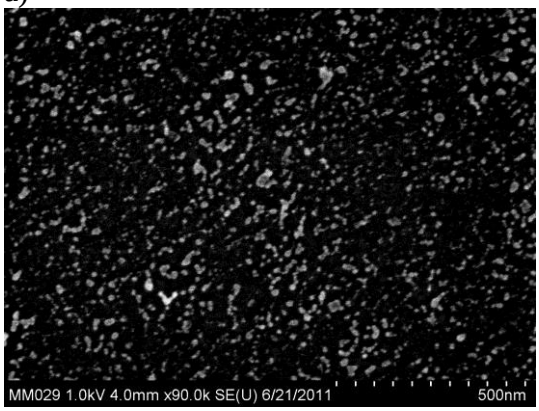

b)

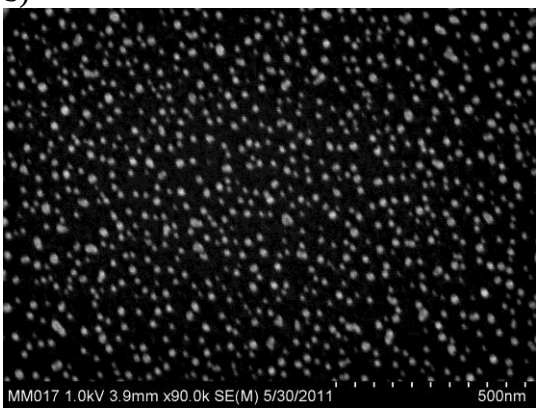

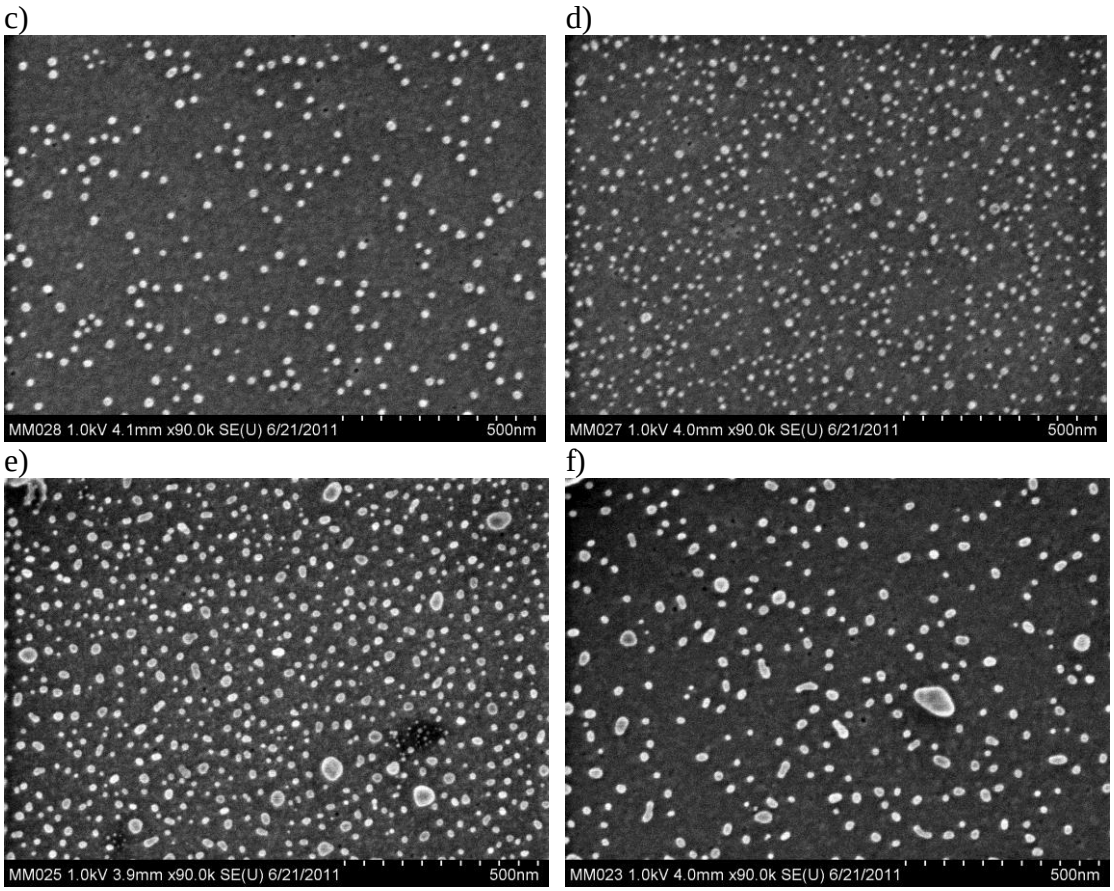

Figure 4.3.1 – SEM images of silicon surfaces after the standard electroless procedure for 2 minutes at (a) 4°C, (b) room temperature (~20°C), (c) 30°C, (d) 40°C, (e) 60°C and (f) 80°C.

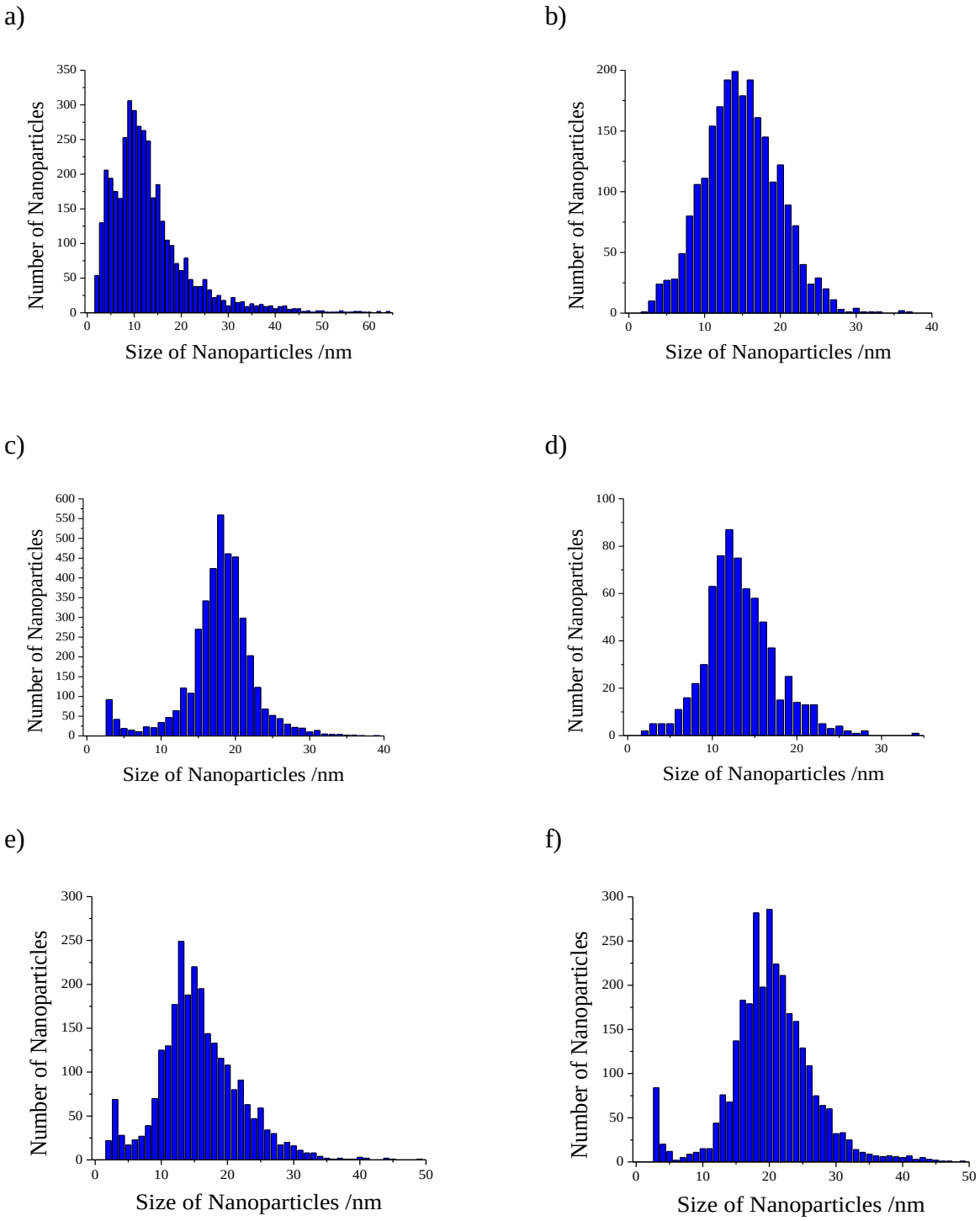

Figure 4.3.2 – Histograms of gold nanoparticles deposited onto silicon surfaces using the standard electroless procedure for 2 minutes at (a) 4°C , (b) room temperature (~20°C), (c)30°C, (d) 40°C, (e) 60°C and (f) 80°C, created using the summation of 3 SEM images taken at different locations on the surface.

Temperature /ºC	Average Size /nm	Standard Deviation /nm	Standard Error of the Mean /nm	Average Particles/μm^2	Standard Deviation of Particles/μm^2	Percent of Surface Covered /%	Standard Deviation in Coverage /%
4	14	7	0.19	553	347	9	2.5
20	16	5	0.17	581	51	13	1.2
30	19	5	0.16	190	35	6	0.61
40	15	4	0.16	466	-	9	-
60	18	6	0.23	361	119	10	4.1
80	23	8	0.32	159	30	7	1.2

Table 4.3.1 – Table of temperature dependent results summarizing the particles size and surface coverage.

Figure 4.3.1 shows SEM images of silicon treated using the RCA electroless method (Section 3.3.1.1on page 31) with a 2 minute dip time in 1% HF and a 2 minute deposition time at varying temperatures. The temperatures used were a) 4°C, b) room temperature (~20°C), c) 30°C, d) 40°C, e) 60°C and f) 80°C. This was done to see the effects temperature has on the deposition process.

Figure 4.3.2 shows the size distribution histograms created using SEM images taken from the different samples shown in Figure 4.3.1. From Figure 4.3.2 it can be seen that the size distribution, or at least the large peaks in each making up a majority of the population, decreases in width between Figure 4.3.2b and Figure 4.3.2c. Figure 4.3.2d is a similar width to Figure 4.3.2b, and size distribution further increases in Figure 4.3.2e at 60°C and again in Figure 4.3.2f at 80°C. Figure 4.3.2a, which was cooled to 4°C, also has a very wide size distribution. This suggests that there is an optimal temperature for achieving the best, most narrow, size distribution. This temperature is likely located between 20°C and 40°C.

Table 4.3.1 summarizes the results found from the images in Figure 4.3.1. From Table 4.3.1 it can be seen that for the most part the average size of the nanoparticles increases with increase in temperature. However, looking at the standard deviation, the average sizes between the 4°C and 40°C samples are somewhat indistinguishable in size. The standard deviation is a good indicator of how broad the size distribution is; the larger the standard deviation is the broader the size distribution. The standard error of these averages is only 0.19 nm, 0.17 nm, 0.16 nm and 0.16 nm for the 4°C, 20°C, 30°C and 40°C samples, respectively, so the averages are fairly accurate within the population. Therefore, it is likely that there is very little increase in size until the higher temperatures are reached.

From Table 4.3.1, the 30°C sample does not fall into this trend with an average particle size of 19 nm. This is most likely due to the same reasoning discussed in Section 4.2, in which the effects of doping and mechanical defects on the silicon surface may affect the deposition. The 30°C sample has a comparatively low particle count, at 190 particles/μm^2. However, the 30 second sample has a higher percent coverage than any of the other samples, due to the larger size of its particles. In section 4.2, the 15 second sample (shown in Figure 4.2.1a) had a higher particles count than that of other samples treated using longer deposition times, and that it was due to a higher number of defects. Conversely, if an area within a bulk sample of silicon is less heavily doped it will contain fewer defects and thus fewer nanoparticles will be deposited onto the surface. Therefore, once the defect areas and H-terminated sites (mentioned in Section 2.1 as possible areas for the beginning growth of gold nanoparticles in the electroless process) have been used up, the primary reaction occurring will be the growth of the already adsorbed

nanoparticles, which will cease once the surface has become oxidized. Therefore, the nanoparticles in the 30°C sample are larger due to the smaller surface coverage.

The standard deviation values shown in Table 4.3.1 also demonstrate an optimal temperature for size distribution. The 4°C sample has a fairly large standard deviation to its compared to average size giving a relative standard deviation (RSD) of ~0.5, which improves to ~0.31 at RT and then again to ~0.26 at 30°C. The RSD then increases to 0.27 at 40°C, to ~0.33 at 60°C and an RSD at 80°C of ~0.35. Therefore the optimal temperature is likely between 30°C and 40°C.

As mentioned previously, there seem to be a correlation between particles size and temperature. There are three factors that may make this possible. The first factor being that the gold/silicon interface is both mechanically weak and chemically inactive[43]. This means that the gold has a fair amount of mobility on the silicon due to low surface interaction. Therefore, it is possible for gold to aggregate into larger particles. The second factor also has to do with gold's mobility on the silicon surface, but due to melting points rather than surface interaction. The more nanoparticles are on the surface, and the higher the surface coverage, the lower the melting point of the gold[44]. This "melting point" mentioned here is not necessarily referring to a change in phase of the gold nanoparticle, but more of a softening that will allow the particles to fuse into one another, creating larger particles. The smaller the gold particle the lower its melting point becomes, which will be much lower than that of bulk gold. Therefore, if the surface coverage becomes high enough, the smaller gold nanoparticles will begin to melt and aggregate into larger ones. The third factor, takes into account the temperature of the plating solution. The higher the temperature the easier the surface is to oxidize. Consequently, this causes a

competition between whether the gold will nucleate to the surface or the surface will merely be oxidized by the water in the solution without forming nanoparticles. This can be seen in the SEM images and histograms (Figure 4.3.1and Figure 4.3.2, respectively) of the samples fabricated at higher temperatures. Therefore, if the surface is oxidized too quickly fewer nanoparticles will form on the surface, and therefore the only reaction taking place is the growth of the particles.

The small size distribution of the 30°C sample is most likely due to the added mobility of the particles on the surface compared to that of the 20°C sample. Gold nanoparticles have been found to have a substantially smaller melting point than that of larger gold materials, the smaller the nanoparticles the lower the melting temperature[44]. However, the low temperature may not be enough to cause gold to melt. Therefore, gold's weak interaction with silicon[43] would probably be the main contributor in this process. Gold has a high affinity for other gold materials, so with its increased mobility on the surface, the smaller nanoparticles will cluster together. This could greatly lower their melting point temperature[44] and cause them to aggregate into larger particles or the nanoparticles could merge together. Therefore, even at 30°C, this will give some of the particles more mobility on the surface allowing smaller particles to aggregate into larger ones. In this case, the aggregation is beneficial, reducing the differences in size making a more narrow size distribution.

For the 40°C the deviation in size is greater than that of the 30°C sample. However, to explain this, the same reasoning applies. At higher temperatures more particles will become mobile causing aggregation of the particles and forming particles of different sizes[44,43]. Consequently, in this case, the size distribution is increased. The 60°C

sample follows the same trend. Under the same reasoning, more particles melt at this temperature creating a wider size distribution[44]. From the histogram, particles have formed as large as 62nm in this sample. Although the size distribution of the 80°C does not follow the same trend as the previous samples, the size of the particles still increase. From the histogram of the 80°C sample (Figure 4.3.2f) it can also be seen that particles up to 89nm can be formed.

From these result it can be concluded that the higher the temperature of the plating solution used the larger nanoparticles can be formed, but that also lead to larger differences in size distribution.

Conversely, in the 4°C sample (shown in Figure 4.3.1a) most of the nanoparticles are much smaller in size than that of the previous sample, which can be seen in the corresponding histogram (Figure 4.3.2a) and in the large number of particles/μm^2 combined with the small percent of gold covering the surface shown in Table 4.3.1. Using the reverse of the previous argument, this is most likely due to the lack of mobility and the inability for the smaller particles to melt into larger particles at the lower temperature of this reaction. Therefore, aggregation of these smaller particles was not possible. The larger particles could be due to extremely active defect sites encouraging increased particle growth[14].

Therefore, it can be reasoned that the colder the plating solution the smaller the particles that are deposited, but, similarly, higher temperatures favours a larger size distribution.

4.4 HF Exposure Investigation:

a)

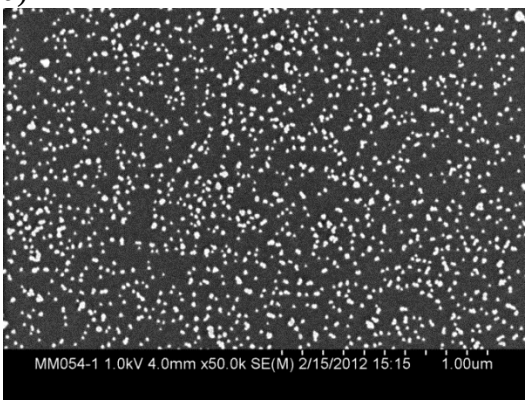

b)

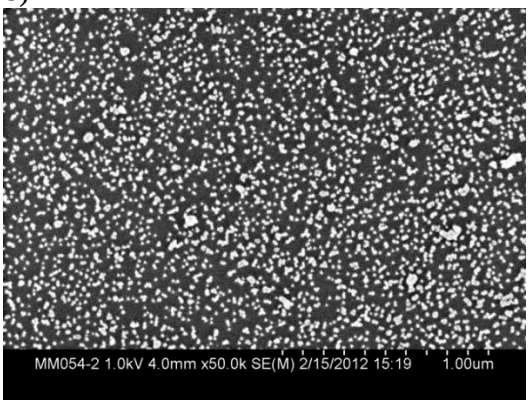

c)

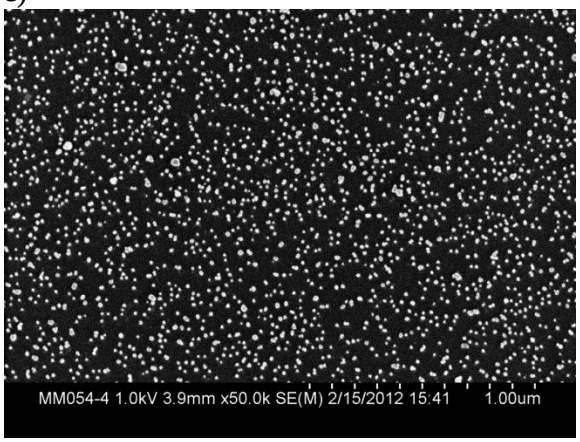

Figure 4.4.1 – SEM images of silicon surfaces after the drop-wise electroless procedure at 30°C with a 2 minute deposition time an HF exposure time of (a) 1 minute, (b) 2 minutes and (c) 4 minutes.

a)

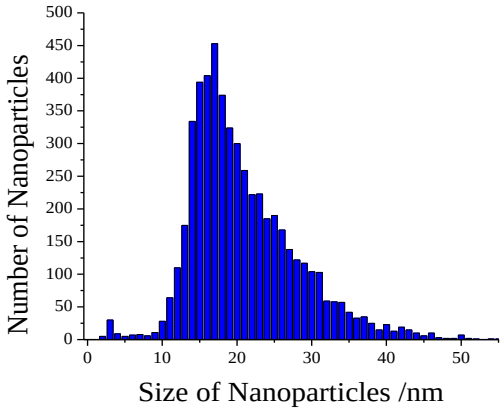

b)

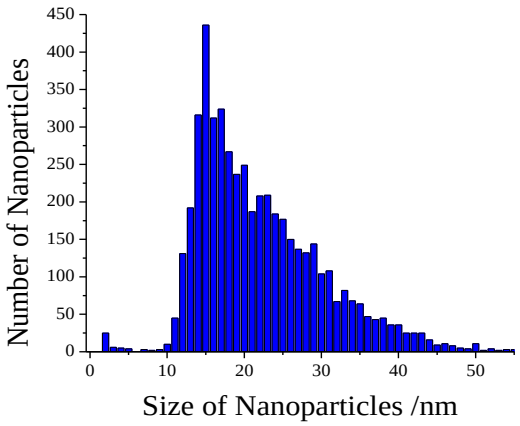

c)

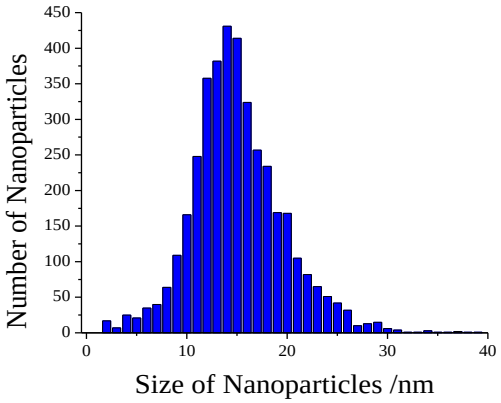

Figure 4.4.2 – Histograms of gold nanoparticles deposited onto silicon surfaces using the drop-wise electroless procedure at 30°C with a 2 minute deposition time an HF exposure time of (a) 1 minute, (b) 2 minutes and (c) 4 minutes, created using the summation of 3 SEM images taken at different locations on the surface.

HF Exposure /s	Average Size /nm	Standard Deviation /nm	Standard Error of the Mean /nm	Average Particles/μm^2	Standard Deviation of Particles/μm^2	Percent of Surface Covered /%	Standard Deviation in Coverage /%
60	21	6	0.15	273	5	10	1.0
120	24	9	0.18	440	70	22	1.8
240	17	5	0.11	438	59	10	0.24

Table 4.4.1 – Table of HF exposure results summarizing the particles size and surface coverage.

Figure 4.4.1 shows SEM images of a silicon surface treated using the drop-wise electroless procedure (Section 3.3.1.2 on page 32), exposing the silicon chip to 1% HF for variable times, followed by a 2 minute dip in the concentrated plating solution heated to 30ºC. The drop-wise procedure was used because one of the primary goals of this research is to deposit nanoparticles onto the surface of a silicon solar cell. The cell cannot be dipped in the 1% HF solution because it will dissolve the silver based back contact,

destroying the cell. Therefore, by dropping the HF on the surface the back contact of the solar cell is protected. This investigation was done to observe what effects longer HF exposure would have on the deposition of gold nanoparticles.

Figure 4.4.2 shows the size distribution histograms for the surfaces of the samples shown in Figure 4.4.1. From Figure 4.4.2 it can be seen that Figure 4.4.2c has the smallest size distribution, but the size distribution of the other sample is also fairly good. Table 4.4.1 summarizes the results found from the SEM images in Figure 4.4.1. From this it can be seen that there is a substantial increase in average particle coverage from the 60 second sample to the 120 second sample, going from an average particle coverage of 273 particles/μm^2 to 440 particles/μm^2. This is expected, as HF exposure is a mandatory step for electroless deposition to work (see Section 2.1 on page 6). The increase in surface coverage may be due to a couple of different factors. First, the longer the surface is exposed to the HF the more silicon oxide will be removed from the surface. Assuming, that one minute is not a sufficient amount of time to remove the oxide layer, then at 2 minutes more the oxide layer will be removed, which gives more areas for nanoparticles to grow on the surface. The second is an increase in the amount of H-terminated silicon[14] (see Section 2.1) which can allow for more active sites in which gold can begin to grow on the silicon as well as more electrons gained through oxidization to fuel the reaction. The third is that HF will also start to remove silicon from the surface, creating more defect sites, and therefore more particles can be deposited onto the surface[14].

The average particle coverage of the sample exposed to the HF solution for 4 minutes is only slightly lower than that of the 2 minutes sample. However, based on the overlap in the standard deviation, the 438 particles/μm^2 for the 4 minute sample and the

440 particles/μm^2 are in the same. This shows that there is a threshold for the amount of nanoparticles you can deposit onto a surface with increased HF exposure.

Therefore, the longer the silicon sample is exposed to the HF solution the greater the surface coverage will be, but only up to a certain threshold.

4.5 Plating Solution Concentration Investigation:

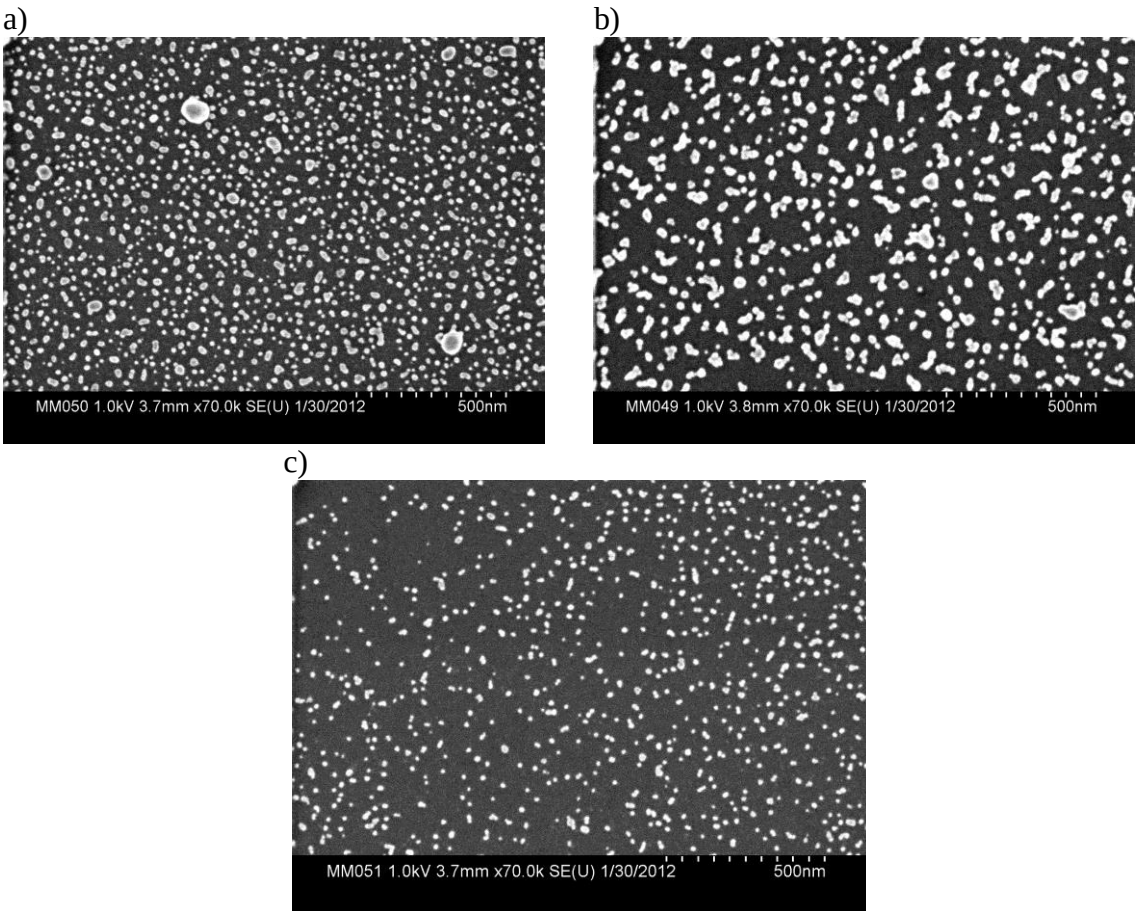

Figure 4.5.1 – SEM images of silicon surfaces after the drop-wise electroless procedure with an HF exposure time of 5 min and a 1 minute exposure to the plating solution of (a) 1:1, (b) 1:3and (c) 1:4; plating solution:water.

a)

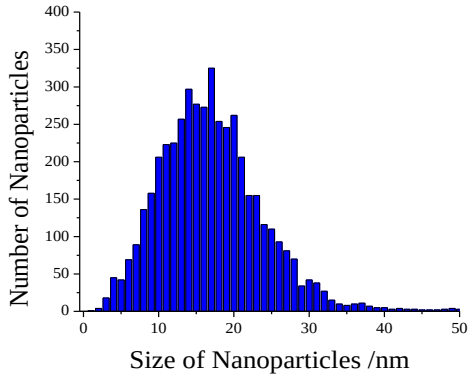

b)

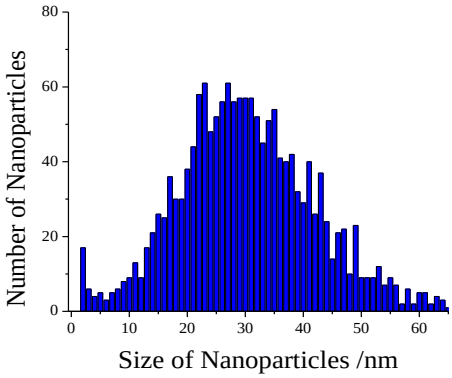

c)

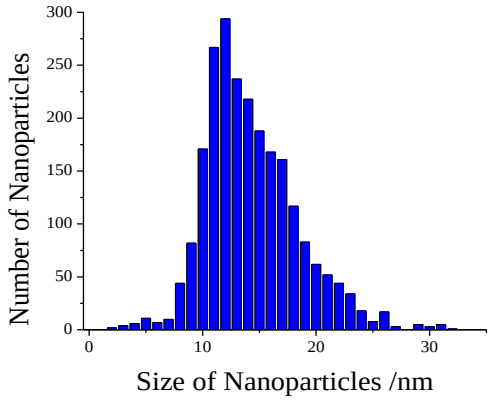

Figure 4.5.2 – Histogram of gold nanoparticles deposited onto silicon surfaces using the drop-wise electroless procedure with an HF exposure time of 5 min and a 1 minute exposure to the plating solution of (a) 1:1, (b) 1:3and (c) 1:4; plating solution:water, created using the summation of 3 SEM images taken at different locations on the surface.

Concentration (Plating Solution:Water)	Average Size /nm	Standard Deviation /nm	Standard Error of the Mean /nm	Average Particles /μm^2	Standard Deviation of Particles /μm^2	Percent of Surface Covered /%	Standard Deviation in Coverage /%
1:1	19	8	0.21	637	31	20	0.5
1:3	31	12	0.56	227	5	20	1.3
1:4	16	4	0.42	447	77	9	0.4

Table 4.5.1 – Table of concentration dependent results summarizing the particles size and surface coverage.

Figure 4.5.1 shows the SEM images of silicon samples treated using the drop-wise procedure (Section 3.3.1.2 on page 32), with a 5 minutes exposure time to a 1% HF, followed by variable dilutions of the original plating solution applied drop-wise to the surface. The sample was exposed to HF for 5 minutes to make sure that the surface was completely treated, and the threshold number of nanoparticles on the surface could be reached (as shown in Section 4.4). In this way, the concentration of the plating solution would be the contributing factor for the surface coverage. The concentration of the plating solution was diluted using ultrapure water in a) 1:1, b) 1:3 and c) 1:4 of plating solution:ultrapure water. This was done in order to see the effects concentration has on the gold nanoparticles deposited into the surface.

Figure 4.5.2 shows the corresponding histograms for the surfaces of the samples shown in Figure 4.5.1. Table 4.5.1 summarizes the results obtained from these samples. From Table 4.5.1, the average diameters of the 1:1 sample and the 1:4 sample are fairly similar and within their standard deviations at 19 nm and 16 nm, respectively. However, the 1:3 diluted sample is much larger than the other 2 samples at 31 nm. This is likely due to the same reasoning expressed in Section 4.3, in which the reduced surface coverage of the nanoparticles, 277 /μm^2, allows for more growth before the silicon surface has been

completely oxidized and the reaction stops. This is also shown in the similar ratios of surface coverage, ~20% in both cases, even though the 1:1 sample has nearly 3 times to number of particles on the surface. Therefore, this shows that there may be a correlation between particle coverage and the size of the particles.

Looking at the average particles coverage in Table 4.5.1, there is a fairly substantial decrease in coverage between the 1:1 and 1:3 diluted samples and between the 1:1 and 1:4 diluted samples. As stated previously the large size of the 1:3 diluted sample is likely a reason for why the particle count is so much lower than the 1:4 diluted sample (227 vs. 447); however, the difference between the 1:1 (637 particles/μm^2) and the 1:3 (227 particles/ μm^2) is so large, it could be assumed that this difference is also affected by the concentration of the plating solution.

This conclusion is supported by the difference in the 1:1 diluted solution and the 1:4 diluted solution, at 637 particles/μm^2 and 447 particles/μm^2, respectively. However, unlike the difference between the 1:1 and 1:3 samples, there is a substantial decrease in the percentage of gold on the surface between the 1:1 and 1:4 samples. As the average diameters for the particles in these samples are so similar the size argument can be ruled out as well, and the differences in surface coverage can be attributed to the decrease in concentration of the plating solution.

Therefore, the number of particles deposited onto the surface is affected by the concentration of the plating solution.

4.6 K-Gold Growth Investigation:

a) b)

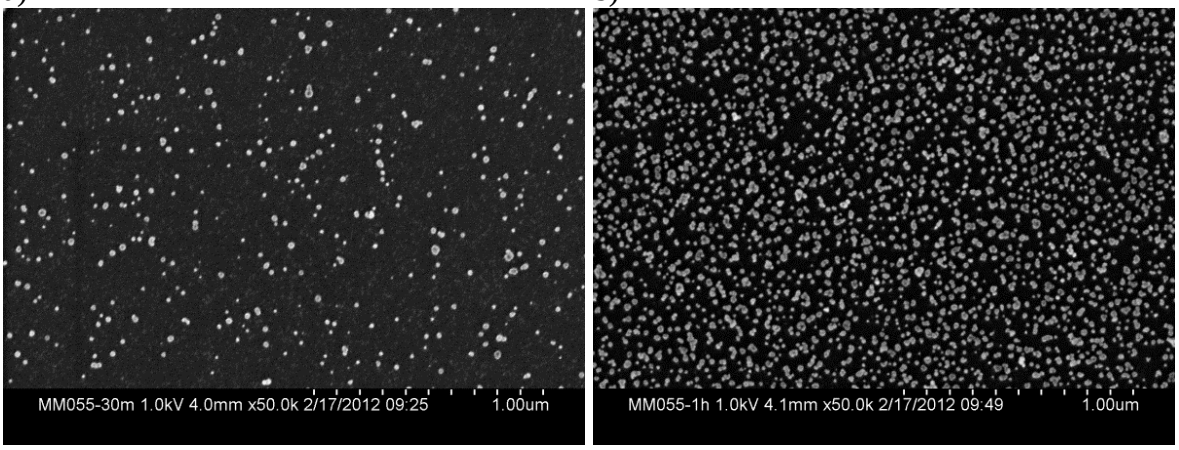

c)

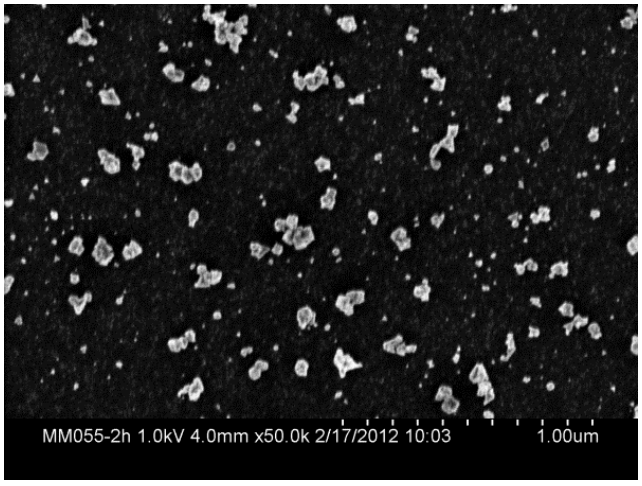

Figure 4.6.1 – SEM images of silicon surfaces seeded with gold nanoparticles using electroless deposition and grown using K-Gold for (a) 30 minutes, (b) 1 hour and (c) 2 hours.

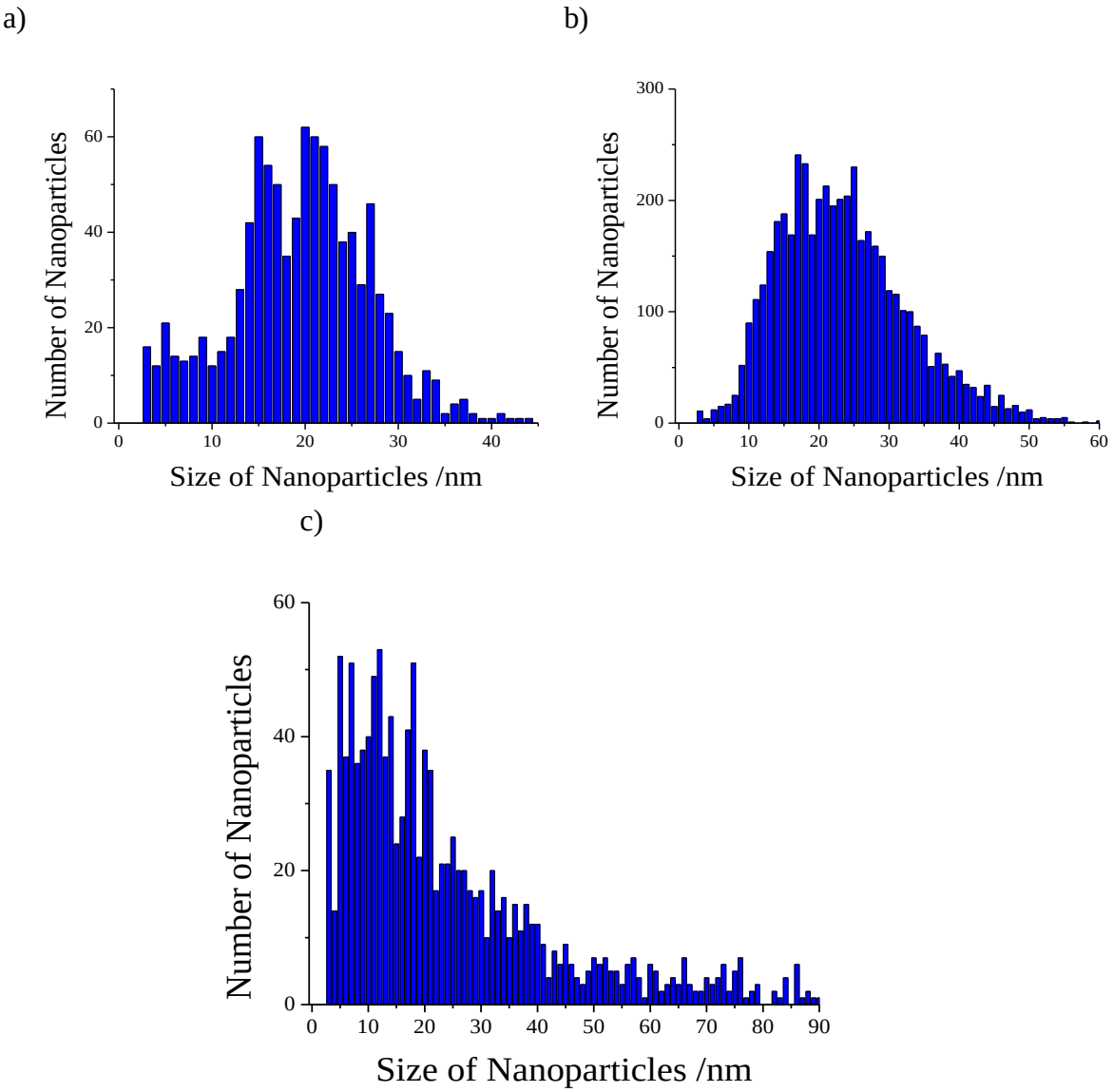

Figure 4.6.2 – Histogram of gold nanoparticles on silicon surfaces that were seeded with smaller gold nanoparticles using electroless deposition and grown using K-Gold for (a) 30 minutes, (b) 1 hour and (c) 2 hours, created using the summation of 3 SEM images taken at different locations on the surface.

K-Gold Growth Time /minutes	Average Size /nm	Standard Deviation /nm	Standard Error of the Mean /nm	Average Particles/μm^2	Standard Deviation of Particles/μm^2	Percent of Surface Covered /%	Standard Deviation in Coverage /%
30	20	8	0.46	78	17	2.3	0.4
60	24	9	0.24	381	84	20	3.9
120	26	22	1.11	101	33	9	1.6

Table 4.6.1 – Table summarizing the particles size and surface coverage at different K-Gold growth times.

K-gold growth[40,41] was performed on samples that had been gold nanoparticle modified using the electroless deposition procedure (see Section 3.3.2 on page 33). There are other methods to grow nanoparticles when they have seeded to the surface[45], but there has been no report into the growth of nanoparticles on a silicon surface using K-Gold. The electroless deposition was performed using the regular electroless procedure with a 2 minute dip in HF and 2 minutes of deposition time in a 30°C solution. The growth was performed as outlined in section 3.3.2.2 on page 33, with varying growth times.

Figure 4.6.1 shows the SEM images of silicon surfaces seeded with gold nanoparticles using drop-wise electroless deposition (see Section 32) after different lengths of exposure to the K-Gold solution. Figure 4.6.2 shows the corresponding histograms for the surfaces of the samples in Figure 4.6.1. Table 4.6.1 summarizes the results of these experiments.

Figure 4.6.1a shows a sample after 30 minutes of growth. After the 30 minutes of growth the average particle size was 20 nm, a standard deviation of 8nm, and a surface coverage of 76particles/μm^2 with 2.3% of the surface covered in gold. From the previous data in Section 4.3, the average size of a similarly treated sample was 19 nm with a

standard deviation of 5 nm. Although there is no significant increase in average particle size, the higher standard deviation suggests that there may some growth happening.

Figure 4.6.2a shows the histogram for the size distribution of the 30 minute treated sample. From the histogram there are particles above 40 nm, which is not that different from the un-grown sample. Therefore, from this there is no real evidence that any growth has actually occurred within the 30 minute time span.

Figure 4.6.1b is an SEM image of a sample seeded using the same procedure as the sample in Figure 4.6.1a, with a growth time of 1 hour. The average particle size for this sample is 24 nm, with a standard deviation of 9nm and a surface coverage of 381 particles/μm^2 with a 20% of the surface covered in gold. So, from the previous sample there has been an increase in the average particle size of this sample. The increase in size with respect to the surface coverage also point to particle growth, as most samples with a surface coverage of ~400 have an average particle size of ~14 nm – 18nm.

Figure 4.6.2b is the histogram of this Figure 2.2.1b. In comparison to the 30 minute growth sample, the 1 hour sample has a much higher maximum with particle around 60 nm. This shows that there is an increase in size with a longer growth time.

Figure 4.6.1c shows the image of another sample seeded in the same manner as the two previous samples, but it was allowed a 2 hour growth time. The average particle size is 26 nm, with a standard deviation of 22 nm, and a particle count of 101 particles/μm^2 and a percent coverage of 9%. The average size has increased further from the previous sample. From the image it can be seen that there is aggregation from the grown nanoparticles. The low particle count could be due to gold nanoparticles being removed from the surface during the growth process. As the silicon/gold interaction is

weak and chemically inactive[43], it is completely possible that the gold nanoparticles could be removed from the surface after deposition, in particular larger nanoparticles which could be more likely to be removed during the rinsing process. This was not seen in the previous samples, however in Figure 4.6.1c the larger particles are bigger than any particles deposited using the electroless procedure alone, with many particles of sizes over 70 nm, compared to the small number of particles that were over 50 nm in the temperature investigation shown in Section 4.3 (page 49). Therefore, if there was high concentration of large nanoparticles, then the interaction between these large particles and the water used to rinse the surface of the silicon, some of these particles may be rinsed off.

Figure 4.6.2c shows the histogram of Figure 4.6.1c. From the histogram, there are a large number of particles that have grown to sizes over 50 nm. However, there are also a large number of particles below 20 nm. This could be due to external nucleation in the K-gold solution. During the growth, nanoparticles can start to form in the solution, when the sample is removed, rinsed and dried off there is a chance that some of the nanoparticles present in the solution could have adsorbed to the surface. Although the interaction between the gold and the silicon is weak, it may still be possible that smaller particles can adsorb to the surface, while larger ones are removed.

The images above are representative of the center of the silicon chips treated. However, the edges of the chip display a different growth pattern than the center as seen in Figure 4.6.3.

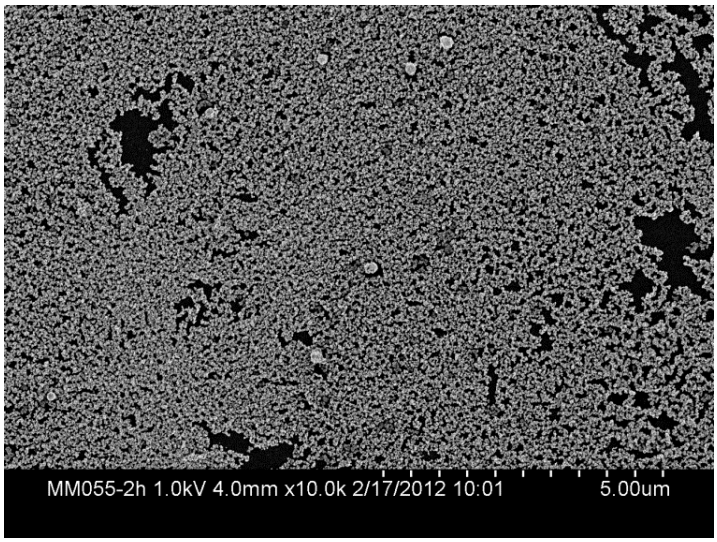

Figure 4.6.3 – SEM image of a silicon surface seeded with gold nanoparticles using electroless deposition and grown using K-Gold for 2 hours at the edges of the sample.

Therefore, at the edges there seems to be a greater amount of growth when using than the K-gold solution, so much so that the particles start to aggregate together forming a film.

4.7 Summary:

From the above experiments: the longer the silicon sample is in the plating solution the more nanoparticles are deposited to the surface, up to a certain threshold. When the plating solution is kept at low temperature a greater concentration of particles are deposited on the surface, conversely the higher the temperature of the plating solution the lower the surface coverage. The size distribution also increases at both high and low temperatures, and the best temperature for even size distribution is between 30ºC and 40ºC. The lower the concentration of the plating solution and the less time spent in the HF solution the lower the coverage of particles on the surface. The K-gold solution does

show an increase in size, however more experimentation is required in order to optimize the surface coverage and the size distribution.

Using this information, it is then possible to tailor the parameters of the nanoparticles deposited onto the surface of the silicon solar cells.

Chapter 5: Solar Cell Results

5.1 Silicon Solar Cell Modification:

Using the results in Chapter 4:, a more precise method, in terms of size distribution and coverage, was determined to adjust the parameters of the procedure given in Section 3.3.1.2 with better precision so that nanoparticles could be deposited onto the surface of the silicon solar cells in a more controllable fashion. This allows more precision in the deposition of the particles so that the effects of surface coverage and size on the current output of the modified silicon solar cells can be investigated.

In this chapter the cells will first be characterized using UV/Vis spectroscopy in order to see the effects nanoparticles have on the reflectance on the surface of the solar cell. The spectral response and the IV curves of both unmodified and modified solar cells are compared, in order see if the gold nanoparticle modified cell has a greater current or power output than that of the same cell that was not modified.

5.2 Characterization of Modified Solar Cells:

a)

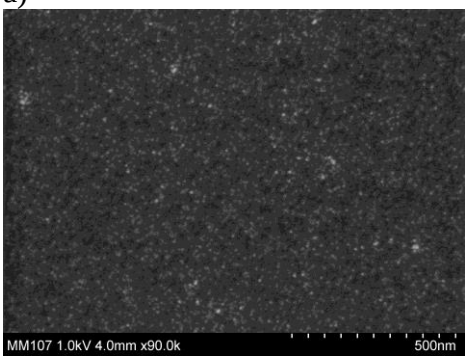

b)

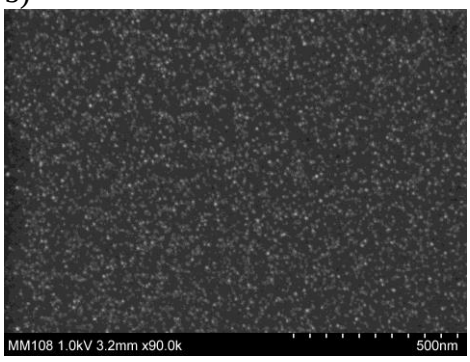

c)

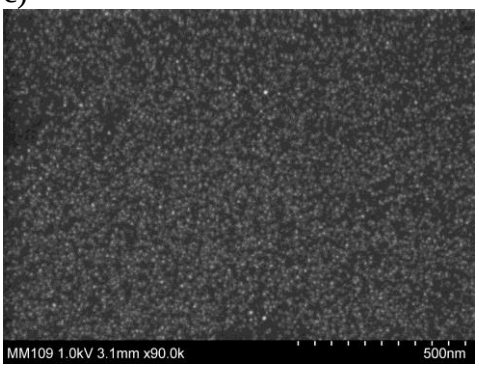

d)

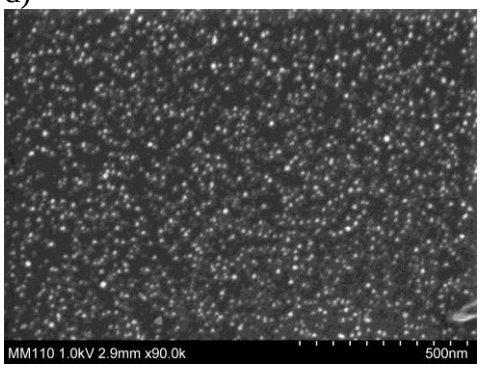

e)

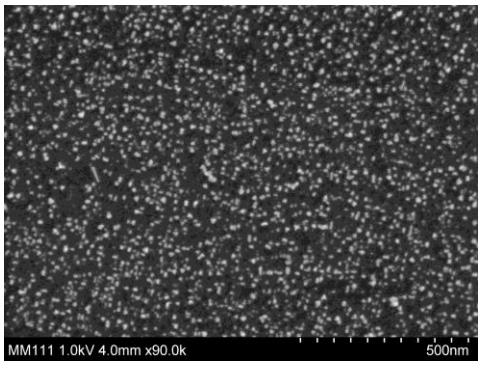

Figure 5.2.1- SEM images of silicon solar cells modified using the drop-wise electroless procedure, with 2 minutes of HF exposure, a 1:4, plating solution:water ratio, and a deposition time of a)5 seconds, b)15 seconds, c)30 seconds, d)60 seconds, and f) 120 seconds.

Figure 5.2.1 shows SEM images of gold nanoparticles deposited into silicon solar cells using the drop-wise electroless procedure, using a 2 minutes exposure to 1% HF and variable deposition times in a 1:4 dilute (plating solution:ultrapure water) mixture (see Section 3.3.1.2 on page 32). The drop-wise procedure was used in order to protect the back contact. These samples were used to see what effect nanoparticles have on the reflectance of solar cells compared to the reflectance of the unmodified cells. Figure 5.2.2 shows the reflectance measurement of a blank silicon sample, which is in agreement with the measurement shown in ref[46]. The measurement shows the percentage of light that hits the surface that is reflected off the surface.

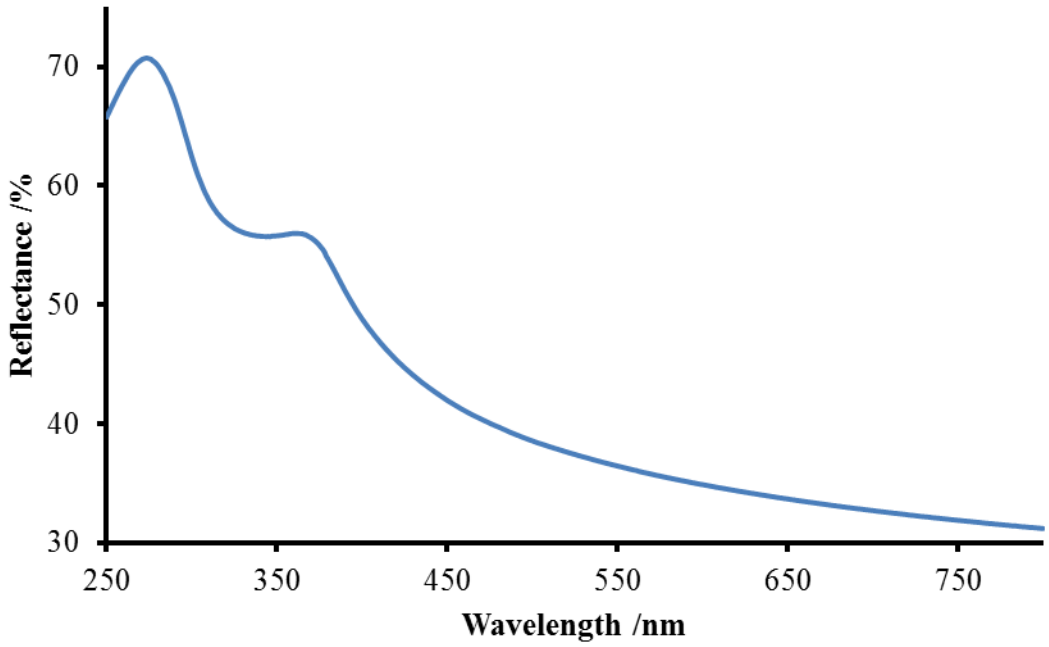

Figure 5.2.2 – Reflectance measurement of a polished silicon solar cells surface.

The silicon surface reflects less light at the higher wavelengths, gradually increasing at lower wavelengths. The maximum amount of light reflected from the blank silicon is at ~70% around 280 nm. However, with respect to the spectral response the monochromator used could only view wavelengths as low as 350 nm. Therefore, the local maximum for the reflectivity of the blank silicon cell with respects to spectral response is at ~55% and 375 nm.

After the initial measurement of the blank solar cells was taken, the surface was modified using the drop-wise electroless procedure (see Section 3.3.1.2), with a 2 minute exposure to HF and a dip in 30°C 1:4, of plating solution and water for variable amounts of time to change the surface coverage.

Table 5.2.1 shows the size data for the samples used for the reflectance measurements:

Time /s	Average Size /nm	Standard Deviation /nm	Standard Error of the Mean /nm	Average Particles/μm^2	Percent of Surface Covered /%
5	11	4	0.16	1692	3.6
15	12	3	0.09	1509	10
30	12	4	0.10	2020	12
60	14	4	0.14	938	11
120	14	5	0.13	1113	17

Table 5.2.1 – Table summarizing the particles size and surface coverage for different deposition times.

Figure 5.2.3 shows a comparison of the $((R_{modified}-R_{unmodified})/R_{unmodified})*100$ where $R_{modified}$ is the reflectance of the gold nanoparticle modified solar cell and $R_{unmodified}$ is the reflectivity of the blank cell before modification, and their difference is ΔR.

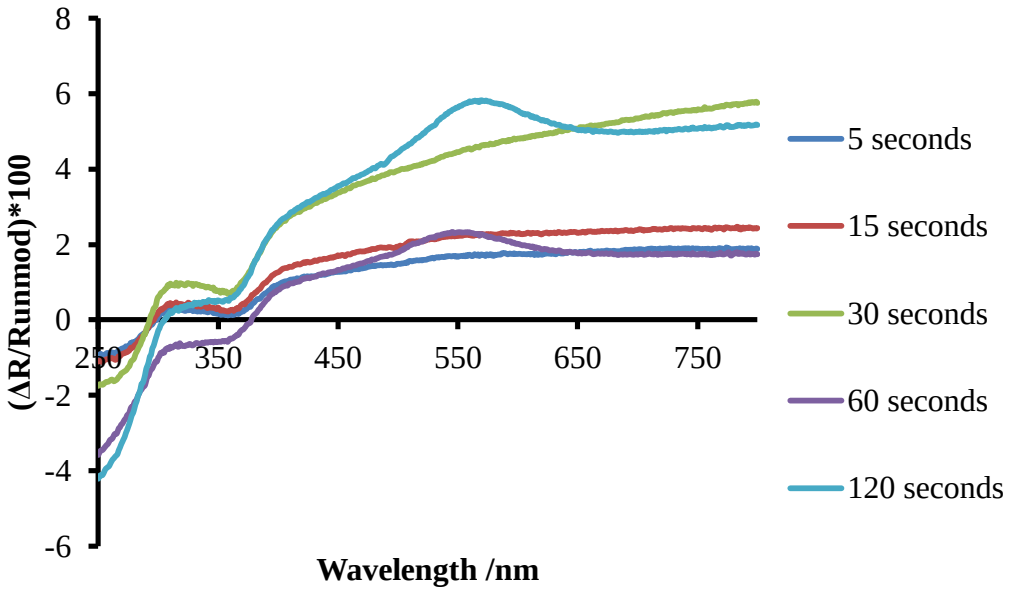

Figure 5.2.3 – Percent difference in reflectance for the reflectance measurements between a modified solar cell and its unmodified solar cell at variable times.

Therefore everything above 0 shows where the reflectance from the surface of solar has increased and everything below 0 shows where the surface absorbs more light.

Figure 5.2.3 shows that for the most part the amount of light reflected increases upon deposition time, and therefore surface coverage. This result is expected for the samples with more coverage, the more gold is on the surface the more light is reflected from the surface. However, for the samples treated using less deposition time, there should have been a slight decrease in reflection showing where the increased scattering of light into the cell was occurring.

Another interesting feature in Figure 5.2.3 is the peak that begins to form at ~550 nm for the samples that had longer deposition times. This can be seen in Figure 5.2.4:

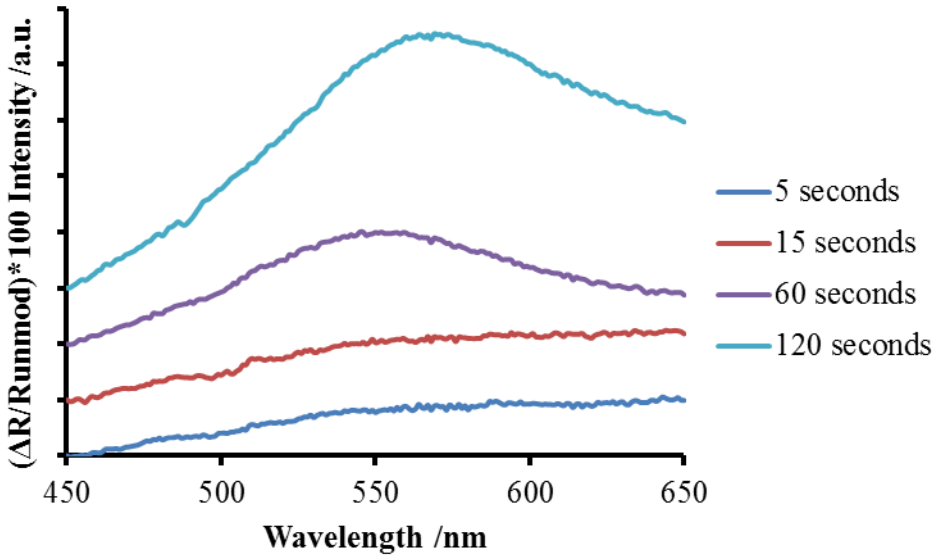

Figure 5.2.4 – Percent difference in reflectance comparison between 450 nm and 650 nm for different time depositions of gold nanoparticles.

In this case the 30 second sample was omitted, as it is apparent that it does not fit into the trend of the other samples. From Figure 5.2.3 the 30 second sample has a much higher reflection that the other samples at similar deposition times. This is due to its greater surface coverage, at 2020 particles/ μm^2 and a percent coverage of 12%. This is

because a gold film starts to develop as more particles are deposited onto the surface, which will reflect more light. However, as seen in Figure 5.2.3, the 30 second has no peak present as that which develops at deposition times of ~1 minute. There are two reasons for this: first, is that due to the high surface coverage, the peak could be so broad that it cannot be viewed under this bandwidth (250nm-800nm). The second is that the peak is more dependent on size than it is to surface coverage, as it only has an average particle size of 12±4 nm, compared to the ~14 nm of the samples showing peaks. Although this is a very small increase in size, as the surface coverage in the 5 and 15 seconds samples (1692 and 1509 particles/μm^2, respectively) are higher than that of the 60 and 120 second samples (938 and 1113 particles/μm^2, respectively) the size of the particles is the only factor seen in the data that could be responsible for this. However, when looking at the percentage of gold on the surface there is an increase between the shorter and longer deposition times, which further shows the increase particle size.

From Figure 5.2.4 it can be seen that the samples with deposition times of 5 seconds and 15 seconds, have very similar shapes with regards to their percent difference in reflectance between 450nm and 650nm. This should be expected as the surface coverage and size of the nanoparticles on the 5 second and 15 second samples are very similar (see Table 5.2.1). However, at 1 minute a peak has formed with a maximum at ~550 nm. This peak suggests that surface plasmon resonance is induced at this wavelength. The fact that the peak is so broad could be due to the different sizes of nanoparticles, which will have different plasmon resonances which is plausible due to its relative standard deviation (~0.3). The peak increases in intensity for the 2 minute deposition time suggesting that there are more nanoparticles on the surface that are under

plasmon resonance, which is displayed on Table 5.2.1. It is also interesting to note that the maximum of the peak has shifted to ~570 nm, which indicates that surface coverage does affect the plasmon resonance[47]. Sandu et al.[47] shows that the more nanoparticles on the surface the more the plasmon resonance will red-shift. This is due to coupling of the LSPR which occurs at a higher wavelength[47]. However based on the average sizes of the samples coverage is not the only parameter necessary, and particles of a larger size are needed to produce this peak.

5.3 Spectral Response Results:

Figure 5.3.1 is the spectral response signal of an unmodified solar cell, blue curve, and the same cell modified with gold nanoparticles using the electroless drop-wise procedure (see Section 3.3.1.2), in red. The solar cell was exposed to the HF for 2 minutes and was in the plating solution for 2 minutes. The drop-wise method was used in order to protect the back-contact to ensure the most accurate measurements.

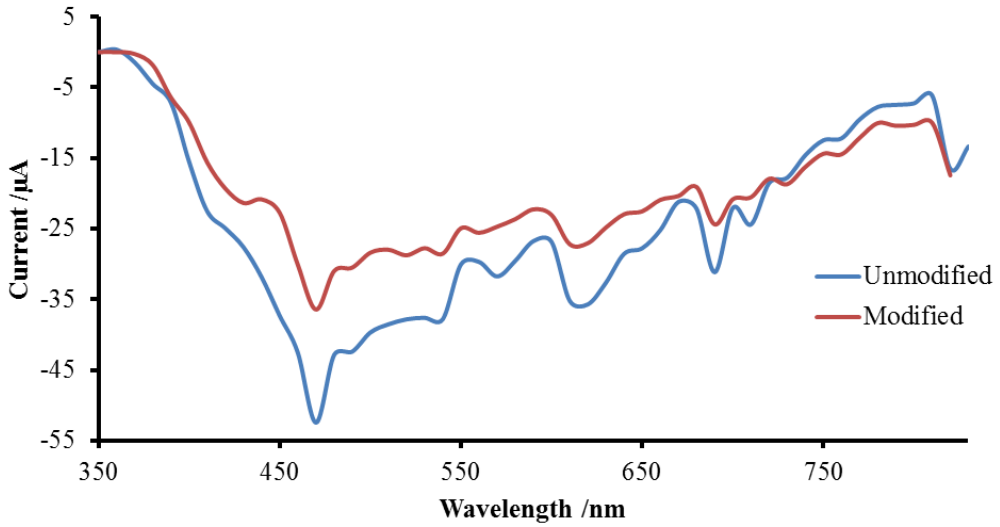

Figure 5.3.1 – Spectral Response of an unmodified cell and its gold nanoparticles modified cell.

In this case the unmodified cell has a larger overall current output at most wavelengths investigated. This decrease in current is due to a couple of factors. The first is that due the nature of the electroless procedure, the more nanoparticles that are put on the surface, the more silicon is used from the surface of the cell. This causes damage to the solar cell making defects of the surface, creating recombination sites for the electrons at the surface[21]. However, other studies suggest that the presence of the metal will prevent more recombination sites from forming[10]. Therefore this factor will be considered negligible. The other factor is that the current will be affected by the coverage of nanoparticles on the surface. The more particles there are the less current is produced; this is due to the competition between the scattering of electrons into the silicon, and the reflection and absorption from the nanoparticles[48]. Essentially at large surface coverage concentrations, less light is reaching the surface, therefore there are fewer photons to be used by the cell to produce a current.

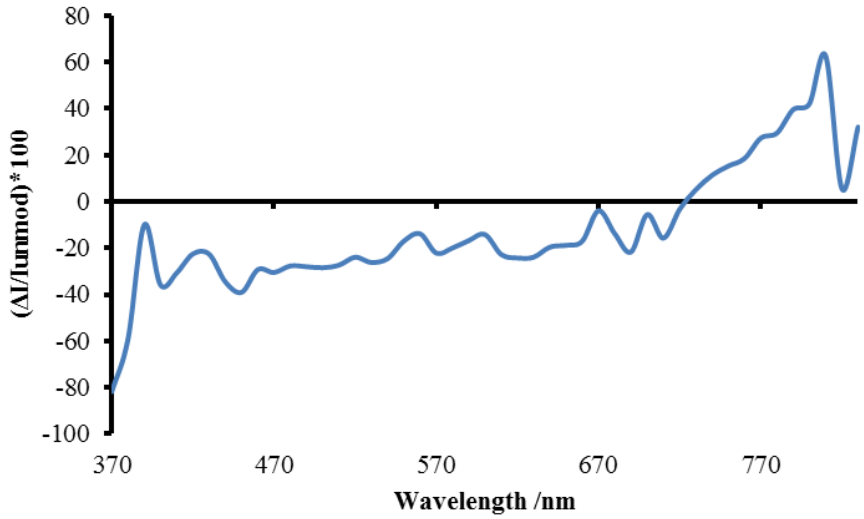

Figure 5.3.2 – Corrected difference in current between the gold nanoparticle modified solar cell and its unmodified cell.

Figure 5.3.2 shows the corrected difference in current between the modified and unmodified cell. Where ΔI is the difference between the current produced by the nanoparticle modified cell and the current of the cell before it was modified. The lamp profile was corrected by dividing ΔI by the current produced by the unmodified cell. This is used to clearly show the differences in the current output at selected wavelengths. Everything that is above the x-axis at 0 is an improvement to the cell, whereas everything below this axis is where the cell is less efficient than the unmodified cell. The benefit of this graph is that the influence of the lamp is removed. The xenon lamp emits white light; however, certain wavelengths are at a higher intensity. This means in order to show the actual spectral response the intensities at each different wavelength would have to be measured and the spectral response would need to be normalized against the lamp. The difficulty with this is that the intensity given off from the lamp will change as the lamp is used, becoming less intense. This is not a significant problem during the time frame of

the individual experiments, but has a large affect over a few months. In Figure 5.3.2 at wavelengths between ~370 nm - ~720 nm the current output of the cell is much worse than the unmodified cell, however there is a slight improvement seen above 720 nm. This could be due to an increase in error caused by the division of two small numbers, as the current is very low in both the lower (~350nm) and higher (~800nm). However, this could also indicate an increase in scattering efficiency at these higher wavelengths. Bulk gold has a reflectivity of ~50% at wavelengths less than 600 nm[30]. An increase in coverage, or size may cause a shift in the plasma based on interaction with other gold nanoparticles in such close proximity changing the reflectance and the scattering cross sections. This could promote additional reflection/absorption at wavelengths higher than 600 nm.

Figure 5.3.3 shows the spectral response of an unmodified cell (blue), the same cell modified with gold nanoparticles (red) and the spectral response after the gold nanoparticles are grown using the K-gold solution (green) (see Section 3.3.2.2). The cell was modified using a 2 minute exposure to HF and a 15 second dip in the plating solution.

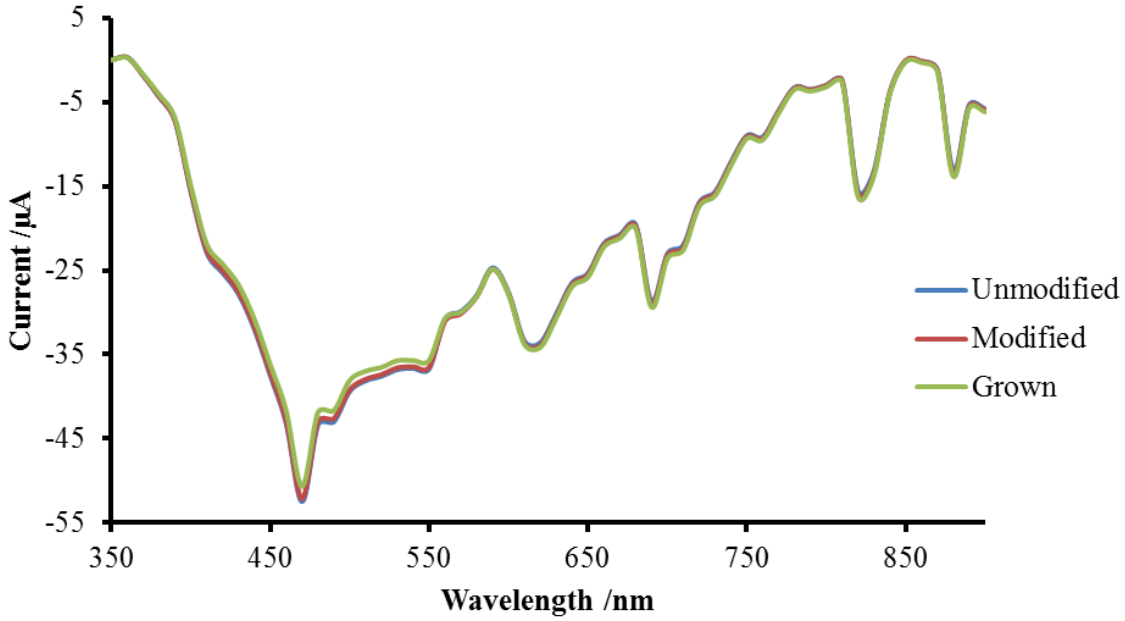

Figure 5.3.3 – Spectral Response of an unmodified cell, its gold nanoparticle modified cell and its K-gold grown modified cell.

The differences in current are difficult to see from this graph, so Figure 5.3.4 shows the corrected difference in current between the modified cell and the unmodified cell. As mentioned previously the error is greater at both ends of the bandwidth tested due to the small current produced, therefore the graph shows the difference in current between 400nm and 750 nm.

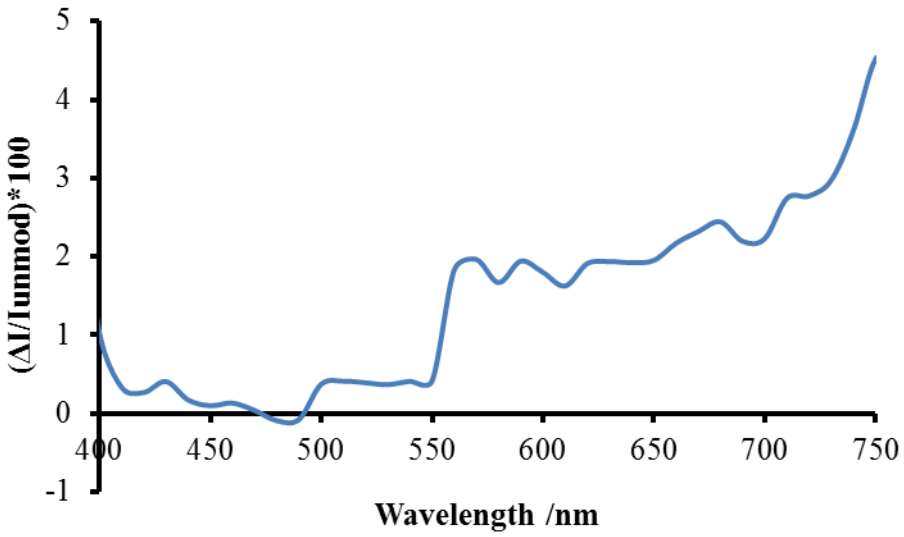

Figure 5.3.4 – Corrected difference in current between the gold nanoparticle modified solar cell and its unmodified cell.

Unlike the cell in Figure 5.3.1 and Figure 5.3.2, this cell shows an improvement after the cell was modified. Between ~400 nm and ~550 nm there is a relatively small improvement in comparison with those between ~550 nm – 750nm. Overall however, there is a slight improvement to the cell at all wavelengths besides 480 nm, where there is a very small loss of efficiency. This trend is similar to that seen in the cell shown in Figure 5.3.1, with greater improvements in the higher wavelengths, which shows a greater scattering efficiency at these wavelengths.

These results are somewhat contrary to the results shown in the previous section (see Section 5.2) in which the reflection is greater in the higher wavelengths. Therefore the current output should also be lower at these wavelengths. The fact that there is an improvement shows that current enhancements shown in Figure 5.3.4 are most likely from light trapping[10], as less light is penetrating the surface, the nanoparticles are increasing the efficiency in which the solar cell converts the light that does penetrate into

electricity. This also shows that there is indeed a competition between light scattering, and reflection and absorption. However, from this it would appear that the greater competitor is the reflection of light from the surface.

Figure 5.3.5 compares the corrected differences in current between the modified cell (blue) shown in Figure 5.3.3, and the same cell after the nanoparticles underwent K-Gold growth (Section 3.3.2.2)(red).

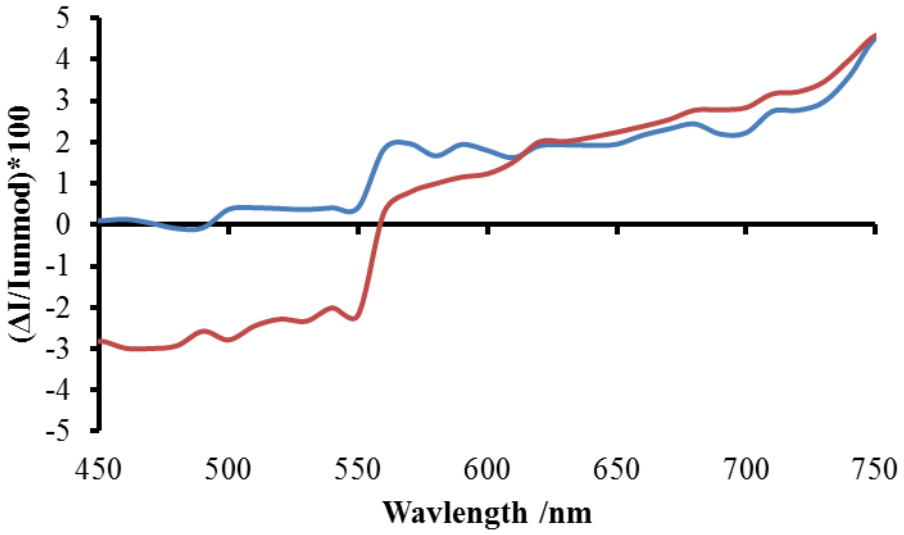

Figure 5.3.5 – Comparison of the corrected differences in current of a solar cell modified with gold nanoparticles (blue) and the same cell after K-Gold particle growth(red).

When the nanoparticles increase in size, a loss of efficiency on the lower wavelength becomes apparent. The trend is more or less the same as that seen in the modified cell. Thus, after K-gold treatment, there is less current being generated which may suggest a greater amount of reflection/absorption in the lower wavelengths. This makes sense due to the increase in area of the gold nanoparticles after growth (see Section 4.6) will produce more of a film on the surface. For the most part there is a very

little improvement in efficiency at the higher wavelengths, which shows small improvements in scattering. However, due to the large loss in current output at lower wavelengths, it does not appear beneficial to change the size of the electroless deposited gold nanoparticles.

Figure 5.3.6 shows the corrected differences in current for a different solar cell that underwent the same procedure as that of the cell in Figure 5.3.3. In this graph the differences in current from the unmodified cell and the gold nanoparticle modified (blue) are compared to the unmodified cell compared to the modified cell after K-Gold growth (red) pair. This graph compares a cell with nanoparticles that are presumably smaller than those deposited onto the cell shown in Figure 5.3.4, and the same cell after its nanoparticles underwent K-gold growth.

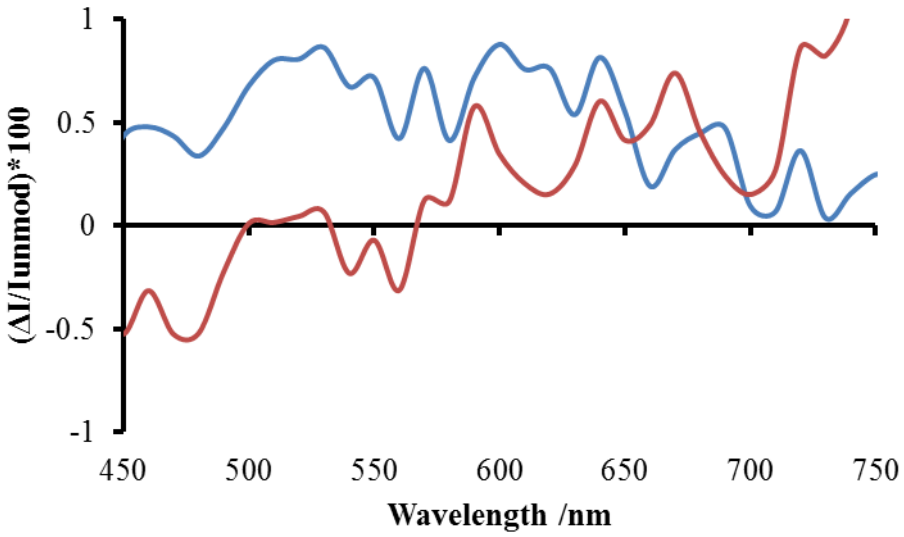

Figure 5.3.6 – Comparison of the corrected difference in current of a solar cell modified with gold nanoparticles (blue) and the cell after K-Gold particle growth (red).

In this case the modified cell shows a greater improvement in the lower wavelengths than in the higher, which is opposite to what was seen in the previous example. However once the nanoparticles were grown in the K-gold solution, the difference becomes more similar to those seen in Figure 5.3.5. This suggests that the size of the original nanoparticles were smaller in this solar cell than those seen in the cell from Figure 5.3.3. The difference seen in current efficiency at different wavelengths suggests a shift in surface plasmon resonance between the smaller and larger nanoparticles, promoting more scattering in the lower wavelengths than in the higher. The smaller particles will absorb or reflect higher wavelengths and scatter the lower wavelength. When they grow the scattering cross section red-shifts and the absorption/reflection occurs at the higher wavelengths[28]. Therefore, Figure 5.3.6 shows that smaller particles seem to be more effective for solar cell enhancement than the larger particles[28]. This finding is useful as a silicon solar cell absorbs light between ~300nm and ~1100nm, with a higher percentage of available light being absorbed from about 750 onwards[49]. Therefore, there are more photons that can be absorbed at lower wavelengths and by increasing the efficiency of the solar cell in this range, there is a higher potential for improvement.

5.4 IV Curve Results:

Figure 5.4.1 shows the IV curves of an unmodified cell (blue), the cell after gold nanoparticle modification (red), and the cell after the nanoparticles are grown in the K-gold solution. The cell was modified using a 2 minute deposition time in HF, and a 15 second dip in the plating solution. This is the same cell used for Figure 5.3.6 and its

subsequent results. Each measurement was taken 3 times and averages, with negligible differences between the results.

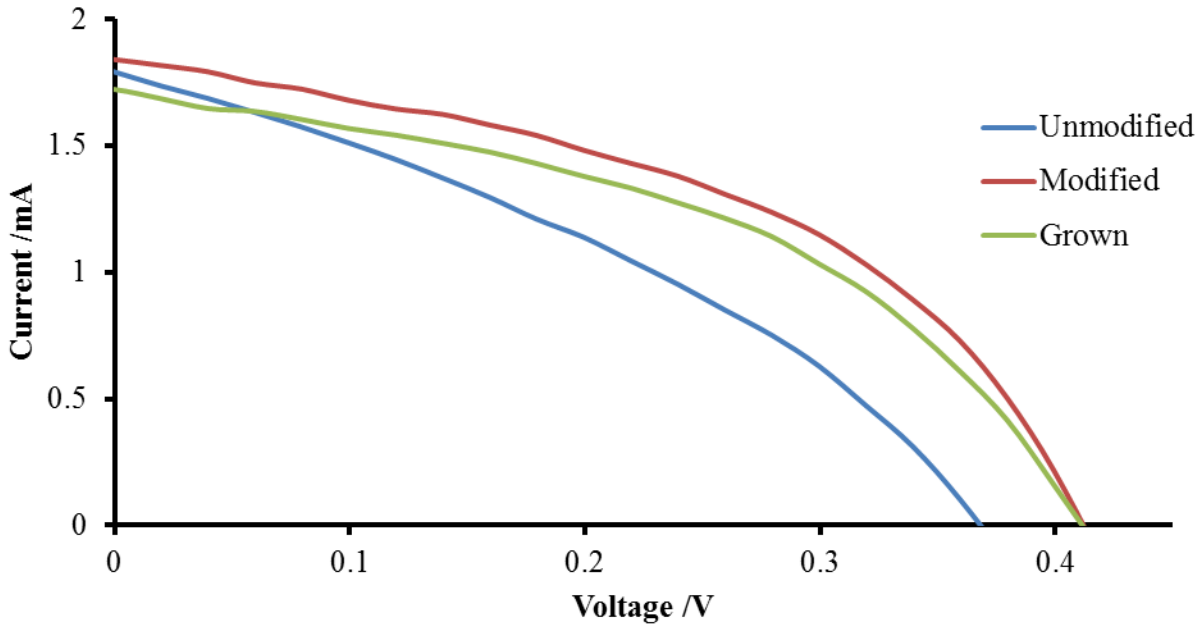

Figure 5.4.1 – IV curve of an unmodified cell, its gold nanoparticle modified cell and its K-gold grown modified cell.

The open circuit voltage for these cells can be seen above. The modified and grown cells both have V_{oc} of ~0.42 V, whereas the V_{oc} of the unmodified cell is ~0.38 V. Typically, the open-circuit voltage should be constant between the same cells. Since the open circuit voltage is the inherent voltage present when no external current is applied, an increase in current caused from the scattering of light from the gold nanoparticles should not affect the open-circuit voltage. Therefore differences are most likely due to problems in contact. If the contact is not complete the resistance of the cell will be higher. However, series resistance should only affect the fill factor of the cell and not the open-circuit voltage. This may suggest that adding gold nanoparticles to the surface has a

physical effect, as well as the scattering effect, that will increase the open-circuit voltage. The meaning of a “physical effect” is that typically the open-circuit voltage should remain constant because it is a specific value for that specific material. Therefore by depositing nanoparticles onto the surface using the electroless procedure, it may be changing some fundamental physical property that effects the open circuit voltage. The Fill Factors for this cell are 0.351, 0.460 and 0.441 for the unmodified, modified and grown cells, respectively. The large increase in fill factors between the unmodified and modified cell is partially due to the better connection and a decrease in the series resistance.

Figure 5.4.2 show the power curves for the unmodified (blue), modified (red) and grown (green) This is the same cell that was used in Figure 5.3.6 in Section 5.3. A power curve, shows the power output of a cell at different voltages, the higher the maximum of the curve the more power generated by the cell.

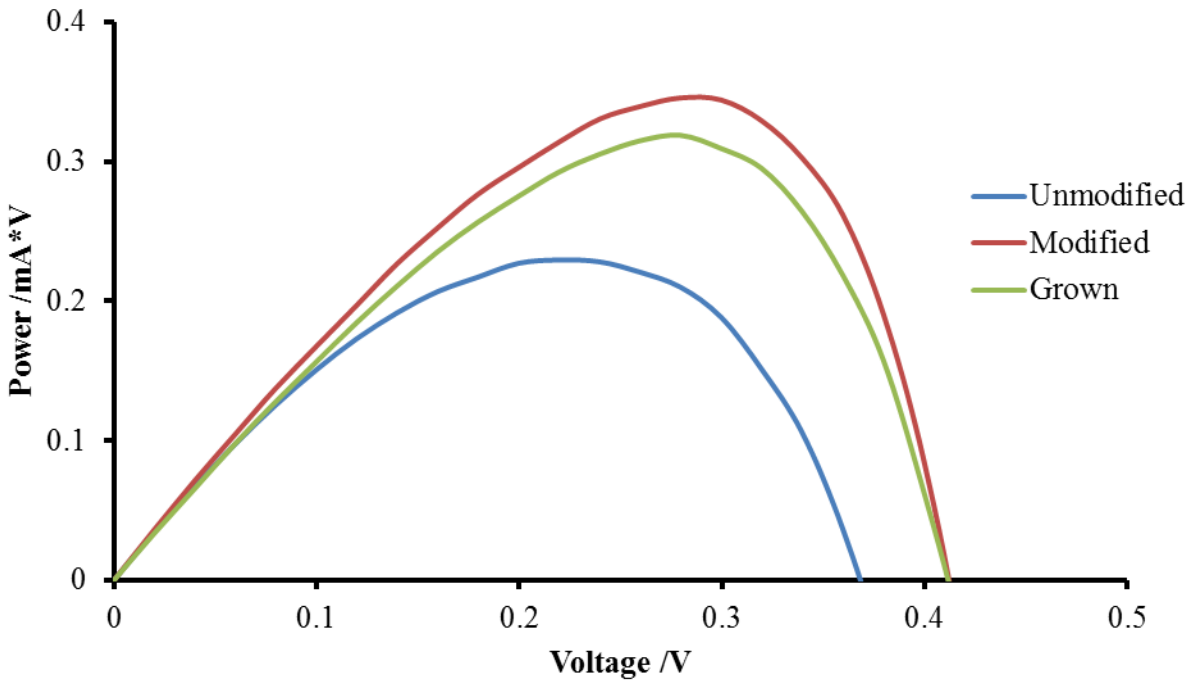

Figure 5.4.2 – Power curves of an unmodified cell, its gold nanoparticle modified cell and its K-gold grown modified cell.

The unmodified curve, like the unmodified cells fill factor, is significantly lower than the modified and K-gold grown cells, for the same reasons previously stated. The important comparison here is the one between the modified and K-gold grown curves. The power curve of the grown cell is slightly less than that of the modified curve. This data is somewhat unexpected when compared with Figure 5.3.6 of the percent differences in current of the modified and K-gold grown cells, where the current only slightly decreases in the lower wavelengths and has a large increase in the higher wavelengths for the K-gold grown particles. From the power curve (Figure 5.4.2) it can be seen that the decrease in current at the lower wavelengths is more substantial than the increase at the higher wavelength (shown in Figure 5.3.6) because the power curve of the modified cell is greater than that of the cell after K-gold growth. This is probably due to the higher

energy and intensity of the light at lower wavelengths. Therefore the photons at lower wavelengths provide more current than those at higher wavelengths.

The same experiment was repeated to test if the same finding would be present in a different solar cell. Figure 5.4.3 shows the IV curve of this repeated test using a different solar cell:

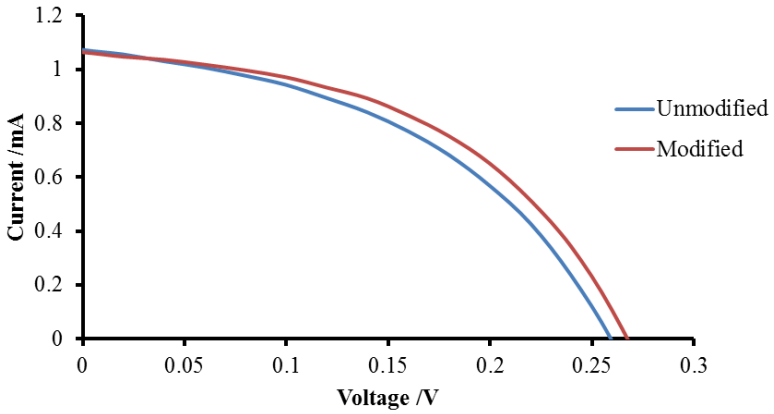

Figure 5.4.3 – IV curve of an unmodified cell and its gold nanoparticle modified cell.

This experiment was done in a more controlled manner; the unmodified cell was measured 3 times and each time the connection was redone to ensure the variation in position would be averaged out. The cell was then immediately modified using the same parameters as mentioned above, and measured in the same fashion as the unmodified cell. This gives a moderately more accurate IV curve. The open-circuit voltage is again higher in the modified cell than that of the unmodified cell, however to a slightly smaller extent, which suggests that there is some sort of physical change in the cell, as extra care was taken in the testing phase.

Figure 5.4.4 shows the power curve for these cells.

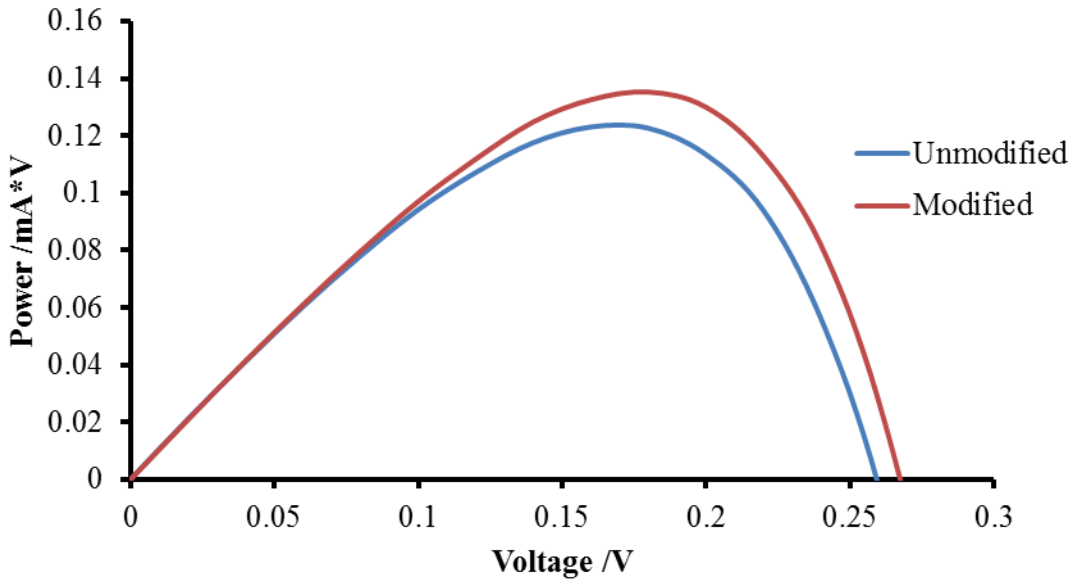

Figure 5.4.4 – Power curve of an unmodified cell and its gold nanoparticle modified cell.

This shows that the modified cell does indeed have a higher power output than that of the unmodified cell. There is a ~10% increase in power between the unmodified and modified cell.

5.5 Summary:

Gold nanoparticles were deposited onto the surface silicon solar cells and caused an enhancement in power generation, however only for samples with a low surface coverage. Samples with a high surface coverage reflect more light than they absorb, causing a decrease in power generation. Samples treated using a 15 second deposition time were shown to provide a ~10% increase in maximum power output.

Chapter 6: Electroless Deposited Nanostructures and SERS

6.1 Silicon nanoparticle modification for SERS:

Another use for nanoparticles deposited onto silicon is their ability to be used for SERS. However, using particles that are randomly deposited onto the surface, such as those deposited using the procedures in Section 3.3.1.1 and 3.3.1.2, will create random hot spots (as mentioned in Section 2.6) and will not be as consistent as those produced using organized nanostructures. Therefore, nanodoughnut arrays were fabricated (see Section 3.3.1.3) by electroless deposition in order to produce nanostructures that have more uniform hot spots and more consistent SERS enhancements. This chapter will look at the structure of the nanodoughnuts that were fabricated and test their abilities as SERS substrates.

6.2 Scanning Electron Microscope Imaging of Nanodoughnut Array:

Using the technique decribed in Section 3.3.1.3 on page 32 gold nanodoughnuts were fabricated on a silicon surface. Similar structures have been fabricated using electroless[50,51] and non-electroless processes[52,53], but none seem to display the same highly crystalline quality as the nanodoughnuts.

Figure 6.2.1 shows the SEM image for an array of nanodoughnuts. The nanodoughnuts are approximately 900 nm in diameter, which varies slightly between structures. The periodicity of the structures is ~4μm in a 5x5 array.

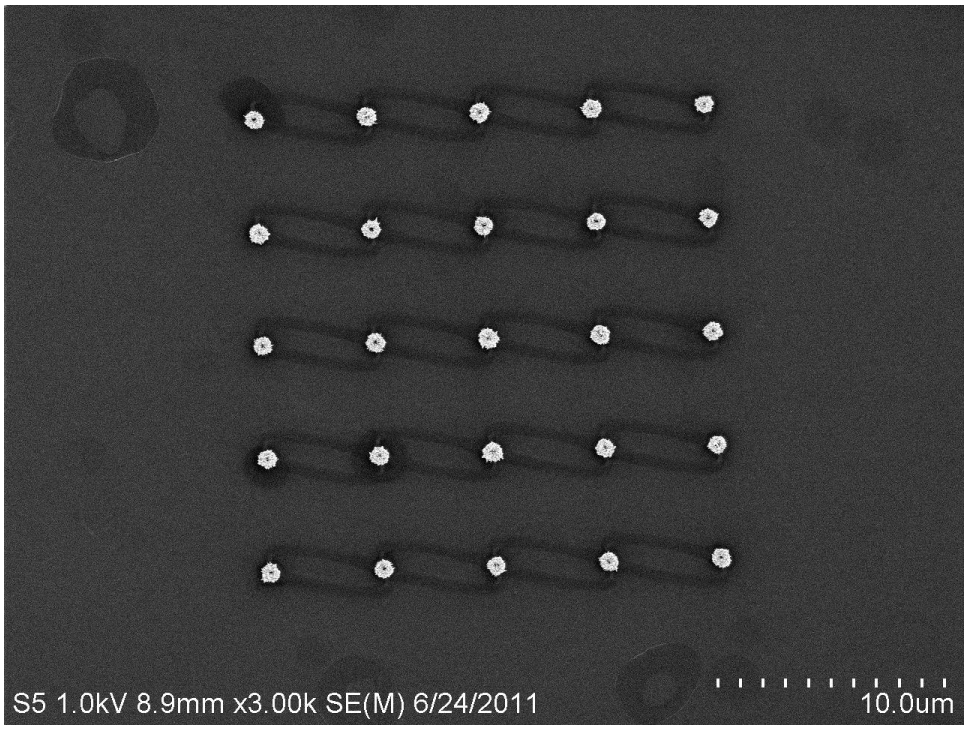

Figure 6.2.1 – SEM image of a full nanodoughnut array.

Figure 6.2.2 shows a closer view of the nanodoughnuts in the array.

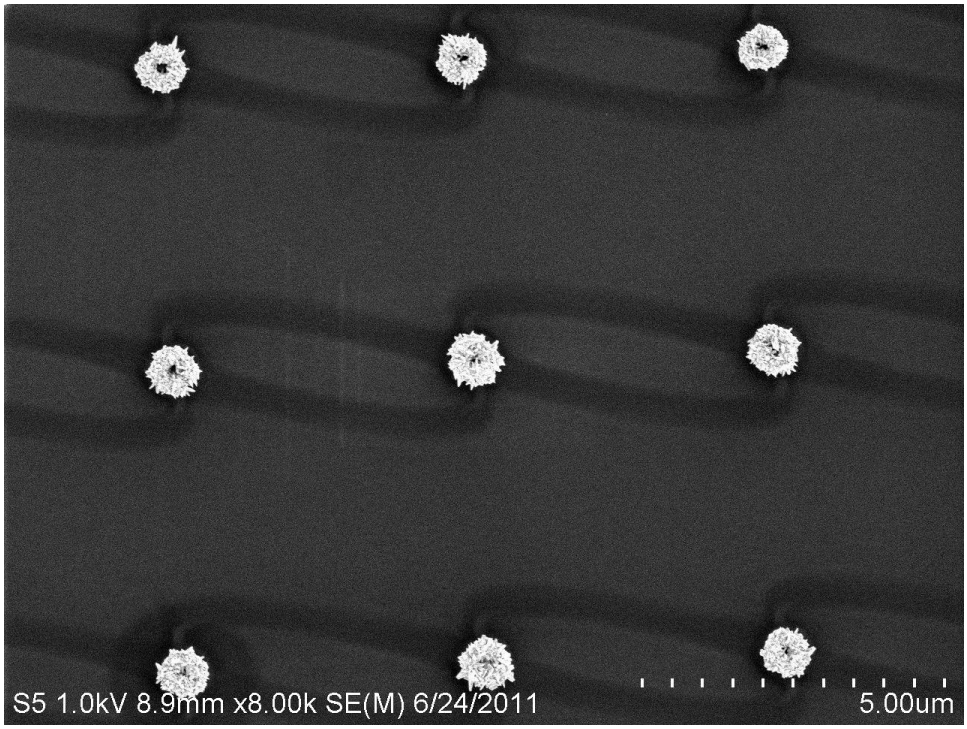

Figure 6.2.2 – SEM image of nanodoughnuts within the array.

In this closer view, differences in structures become more apparent. Each nanodoughnut displays unique crystal structures and projections. Some structures have clear, wide open centers, as in the structure in the top-left of the image. Whereas in others, the crystals begin to grow over the center of the ring and filling in the "hole" of the nanodoughnut.

Figure 6.2.3 show a close up view of a single nanodoughnut. At this magnification, it can be clearly seen that the doughnut is made up of separate gold crystals, forming the polycrystalline structure, which have grown out of the hole produced by the FIB. The growth is random, which is the reason for the individual structures uniqueness.

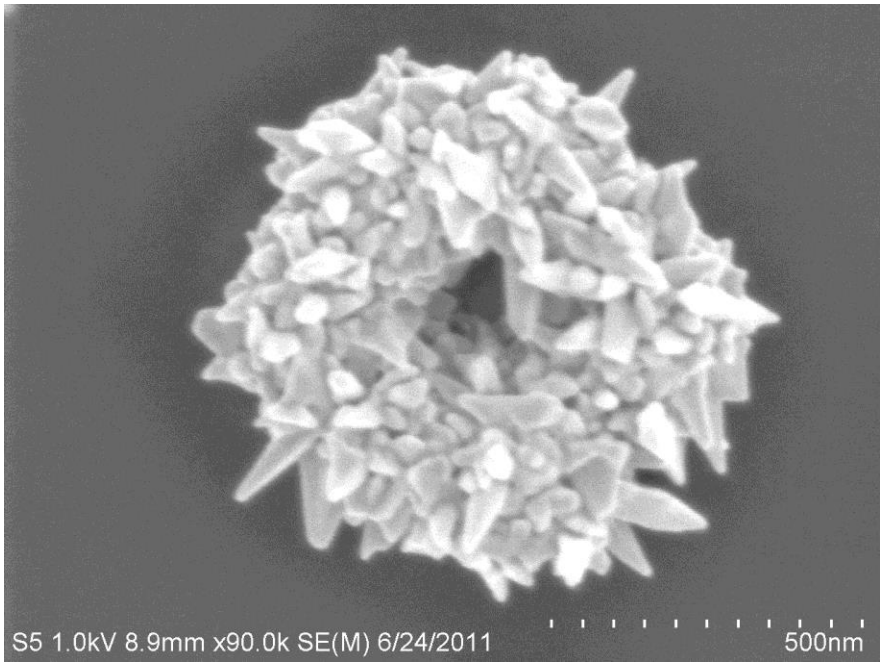

Figure 6.2.3 – SEM image of a nanodoughnut.

Depth can also be clearly seen in the center of the ring, showing the crystal growth within the hole itself.

Figure 6.2.4 shows another nanodoughnut at close magnification. This structure shows large crystal growth outside the structure, particularly the large crystal at the top-right of the nanodoughnut.

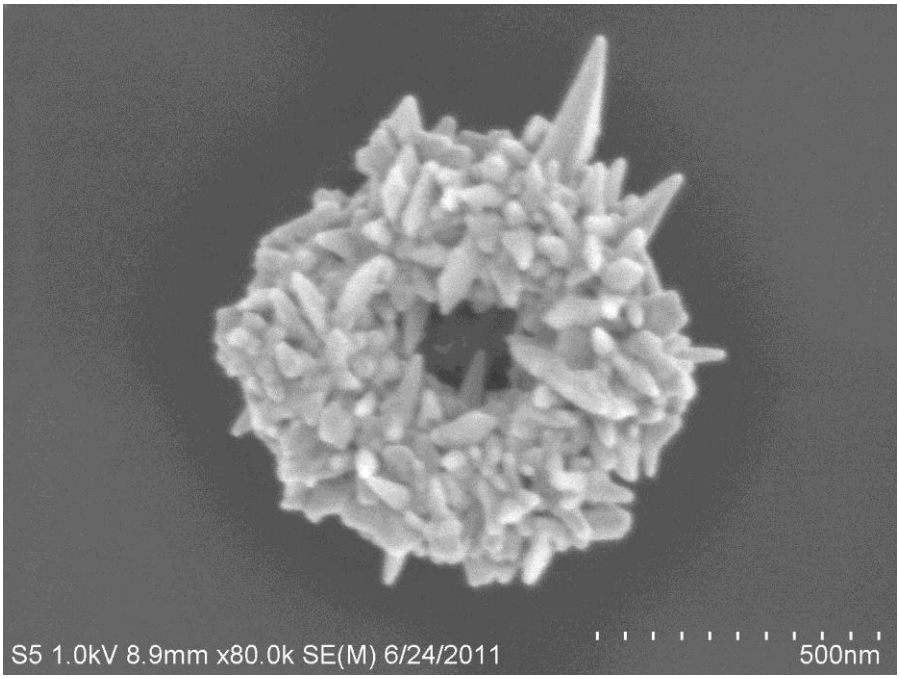

Figure 6.2.4 – SEM image of a nanodoughnut.

The basic mechanism in which the nanodoughnuts are grown starts with the effects of the focused ion beam on the surface of the silicon. When the holes are cut into the PMMA coating on the surface of the silicon, the beam does not necessarily stop once it has reach silicon. The FIB then cuts into the silicon leaving a cone shaped hole. The sides of this cone would be cut fairly jagged producing numerous defect sites in which nanoparticles could begin to grow. The particle coverage in the holes would be very high, so when the nucleation starts the particles would begin to grow together forming the ring

structure of the nanodoughnuts. The bottom of the ring is most likely bare due to the fact that the gold ions are reduced to the nanoparticles present at the top of the cone. Therefore, no gold ions reach the bottom since no nucleation sites are present there. This leaves the bottom empty to be oxidized to continue the nucleation of the particles in the ring creating the large crystal projection in the nanodoughnuts. With additional time the nanoparticles will grow into the center forming more of a disk shape.

Therefore, based on the rough surface configuration of the crystals, these nanodoughnuts should be well suited for SERS.

6.3 SERS Results for Nandoughnuts:

Figure 6.3.1 shows the Raman signal produced by rhodamine 6G at the nanodoughnut sites within the array:

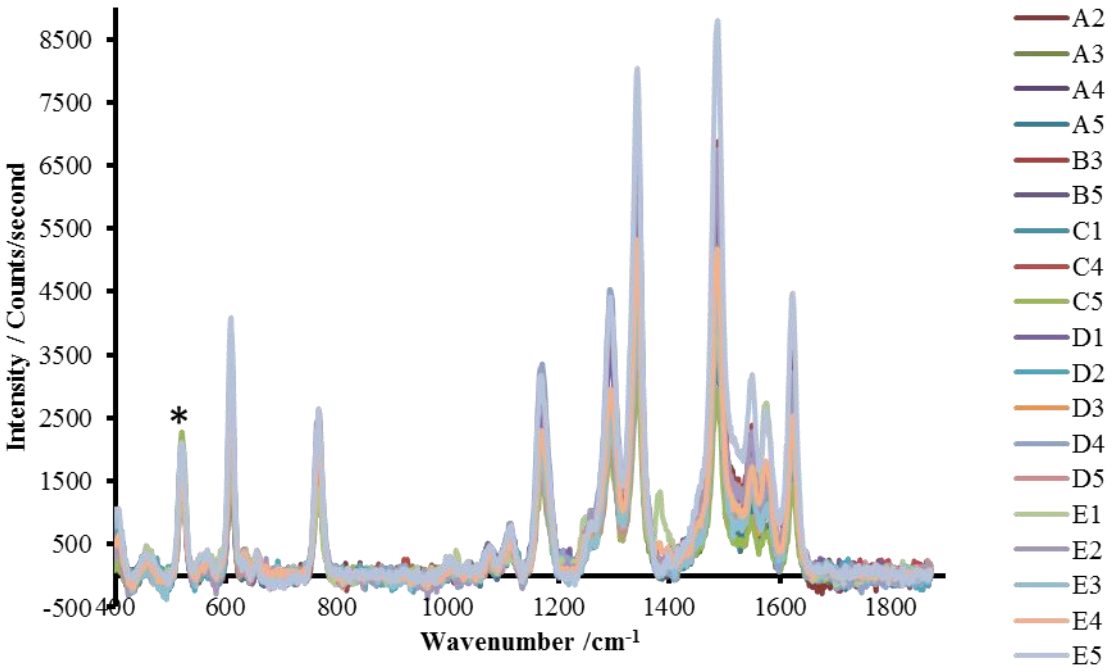

Figure 6.3.1 – Raman signal from 400 cm^{-1} to 900 cm^{-1} of individual nanodoughnuts within an array using rhodamine 6G.

The peak from silicon is located at ~520 cm^{-1} (marked with *), the rest of the peaks present are from the rhodamine 6G[42]. Each peak is labelled relative to a nanodoughnut in the array, some signals have been omitted because of low signal results.

Figure 6.3.2 shows the Raman signal of the blank silicon substrate, away from the nanodoughnut arrays present on the same surface.

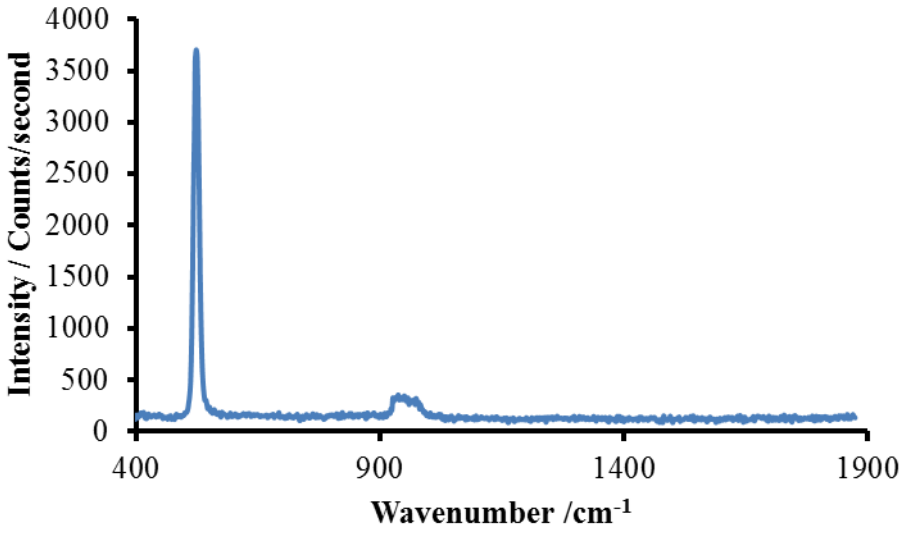

Figure 6.3.2 – Raman spectrum of blank silicon substrate using rhodamine 6G dye, which correlates to literature values found in ref[54].

The silicon peak is still present at ~520 cm^{-1}, and another feature at around ~925 cm^{-1} which is another peak that is present in the Raman spectra of silicon. So from Figure 6.3.2 it is obvious the nanodoughnuts are responsible for the increase in signal intensity of the rhodamine 6G. In fact on the blank silicon sample there is no evidence that rhodamine 6G is present in the solution used. Therefore, the increase in signal intensity cannot even be quantified using the normal Raman spectrum of the rhodamine 6G adsorbed on silicon as a reference.

Figure 6.3.3 shows a blow-up of the signal shown in Figure 6.3.1, between 1450 cm^{-1} and 1700 cm^{-1}.

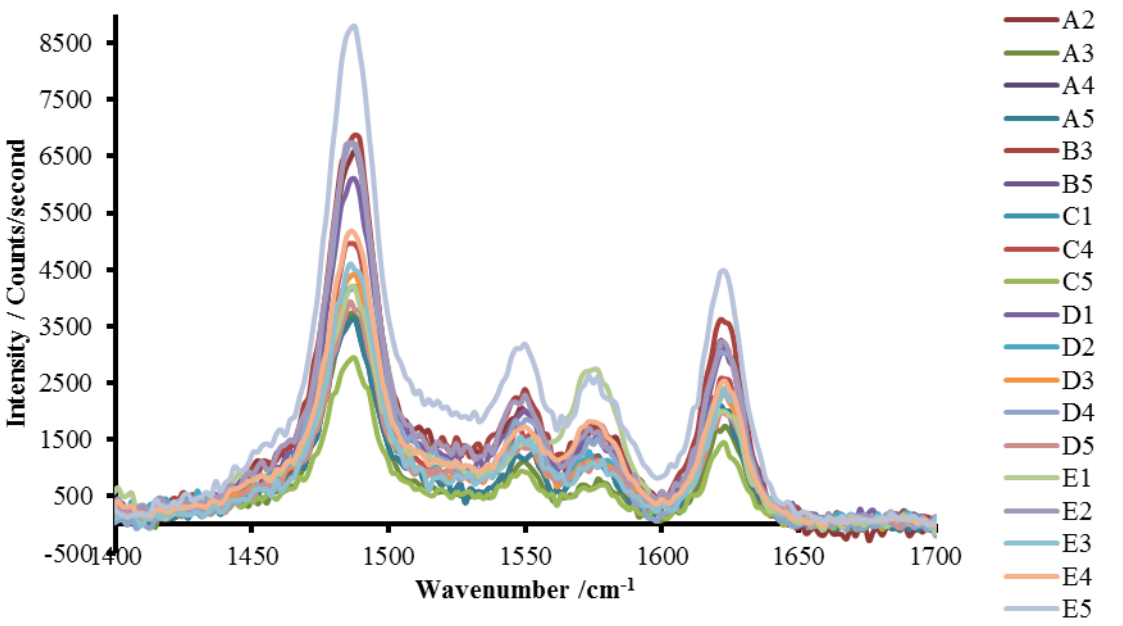

Figure 6.3.3 – Raman signal from 1400 nm to 1700 nm of individual nanodoughnuts within the array using rhodamine 6G taken at the nanodoughnut site.

From this figure, it is apparent that the signal intensity is not consistent between individual nanoparticles. However, this process has not been optimized and therefore there is room for improvement, in which to make the signal intensity more consistent between doughnuts. Due to the difference in the equipment used in similar works it is hard to say if this is an improvement to what currently exists. However, the nanodoughnuts show an interesting and hopefully useful application for electroless deposition.

6.4 Mapping of SERS Signal from Nanodoughnuts Array:

Figure 6.4.1 shows the SERS mapping of the nanodoughnut array taken at ~1485 cm^{-1}:

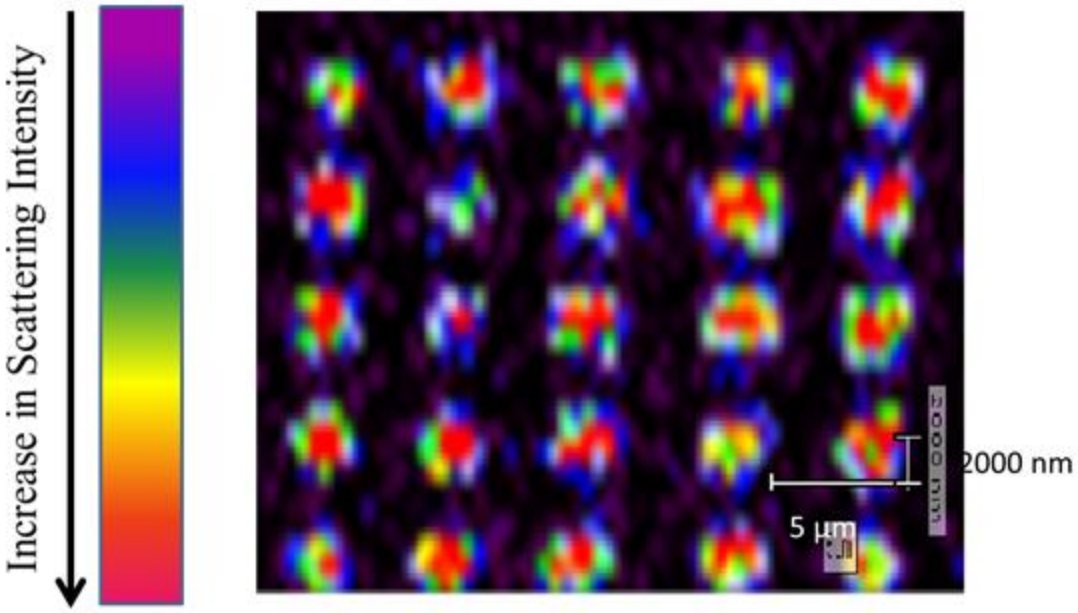

Figure 6.4.1 – Mapping of the SERS signals present in the nanodoughnut array.

As the mapping is done using a false-colour intensity scale, with red being the highest signal and black being the weakest signal. From the figure, it is apparent that the highest signals in the array are located at the nanodoughnuts. This means that the nanodoughnuts produce hotspots that have a higher enhancement factor for the Raman signal than any other areas in the array. This is due to the fact that each individual particle in the nanodoughnut has a LFIEF creating a multi local field enhancement coupling creating a large enhancement factor in this area. For the most part, the silicon has a black colour intensity signifying that there is a very weak Raman intensity for the rhodamine 6G in this area which agrees with the data shown in Figure 6.3.2.

6.5 Summary:

Electroless deposition was shown to be a diverse technique that can be used for nanostructure fabrication. The nanodoughnuts were viewed under the SEM showing that they were polycrystalline in form. A Raman measurement was performed on the nanodoughnut array showing a fairly strong signal for the rhodamine 6G when the measurement was taken over a nanodoughnut. The SERS mapping performed also showed hot spots over the nanodoughnuts. Therefore, the nanodoughnuts were shown to have promise as SERS substrates, however further testing is required.

Chapter 7: Conclusions and Future Works

7.1 Summary and Conclusion:

In the optimization of electroless deposition: deposition time, temperature of plating solution, HF exposure and concentration of plating solution all affect the deposition process. The longer the deposition time, the more nanoparticles are deposited on the surface up to a certain threshold. The greater the temperature of the plating solution, the larger the particles grow, however the size distribution becomes larger as well. Conversely, the colder the plating solution gets the smaller the nanoparticles that are deposited, but the size distribution is still large. A temperature of ~30°C was found to be the optimal temperature for a more uniform size distribution. The longer the sample is exposed to HF the more particles can be deposited on the surface, again up to a certain threshold. The less concentrated the plating solution is made; the fewer nanoparticles are deposited onto the silicon surface.

These findings allow a more accurate deposition of nanoparticles using the electroless technique. However, due to the inconsistency in the quality of the nanoparticles deposited, this technique is still not sophisticated enough to compete with the prefabrication method mentioned in Chapter 1: and Section 2.1. Using the prefabrication method larger and more uniform particles[55] can be deposited onto a silicon surface with better control over the surface coverage[56]. Therefore, more work will have to be done before the particles deposited using electroless deposition will have the same quality and diversity as those deposited using the prefabrication method.

The gold nanoparticles that were deposited onto the surface of the silicon solar cell resulted in an enhancement in power generation, at low particle surface coverages, giving a ~10% increase in maximum power output. As this technique is primarily used on thin-film cells, the results are not comparable to those found in literature, as thin-film cell have a very small optical thickness and the p-n junction cells used in this work have a comparatively large optical thickness, so the enhancements to the thin-film cells are more pronounced. Other techniques are used to increase the optical thickness and the light collection of solar cells as well, such as anti-reflective coating[57], which reduces the reflection of light from the surface of the cell so more photons penetrate the surface; and surface texturing[58], which increases optical thickness by adding a patterned texture to the surface of the cell which increases the angle of refraction of the light penetrating the surface, thus increasing the lights path length in the cell and increasing the optical thickness. Compared to these techniques the increase from the gold nanoparticles is fairly small as combined these two techniques offer a 98% improvement to absorption[59]. However, since the nanoparticles are deposited onto the surface of the silicon these three techniques could be used in concert to not only further increase the light trapping and optical thickness more, but also increase the amount of light absorbed at different wavelengths improving the cell overall. The effects of the nanoparticles deposited using the electroless method were also interesting, showing an increase in open-circuit voltage, which is not seen using the prefabrication method.

Electroless deposition was also used for nanostructure fabrication creating nanodoughnuts which were shown to be promising as SERS substrates. The nanodoughnuts fabricated have a unique polycrystalline structure that makes the entire

nanodoughnut a hot spot. Due to the differences in the apparatus' used for Raman detection, it is difficult to compare the results shown in this work with works in the literature. Therefore more research will have to done to see if this is a viable SERS substrate.

7.2 Future Works:

Future work for the electroless deposition process would be to further reduce the concentration of the plating solution in order to more precisely deposit gold nanoparticles onto the surface of solar cells. This would allow more control in finding the optimal deposition time required to provide the largest enhancements. Also, adjusting the concentration of KF in the plating solution may allow for different sizes of particles to be deposited onto the silicon. If there is less KF, it likely that fewer particles will deposited onto the surface as the nucleation will stop once the surface is oxidized, but growth will continue resulting in larger particles. Inversely, if more KF is added, more particles would be deposited onto the surface leaving less gold available for growth, and producing smaller particles. The deposition on solar cells should be optimized, and precise surface coverages and sizes should be investigated. The steps above would be necessary for this process, and would require finding the ideal surface coverage as well as the ideal nanoparticles size. The fabrication of nanodoughnuts should be optimized to allow for a greater consistency in the Raman signal produced. Adjusting the parameters of the FIB milling could allow for more uniform crystal growth by adjusting the diameter of the hole in the PMMA. Also increasing the thickness of the PMMA may prevent the gold crystals from growing over the sides of the hole making the size of the doughnuts more uniform. Another option would be to melt the doughnuts in order to make a more traditional, or

"smooth" doughnut structure. Other shapes should be investigated such as the production of nano-boxes or nanotriangles, as different shapes affect the hot spots produced by the structure.

Bibliography

1. Xie, Z.; Yu, W.; Wang, T.; Zhang, H.; Fu, W.; Liu, H.; Li, F.; Lu, Z.; Sun, Q., Plasmonic Nanolithography: A Review. *Plasmonics* **2011,** *6*, 565-580.
2. Mody, V.; Siwale, R.; Singh, A.; Mody, H., Introduction to metallic nanoparticles. *Journal of Pharmacy and Bioallied Sciences* **2010,** *2* (4), 282-289.
3. Yang, L.; Akhatov, I.; Mahinfalah, M.; Jang, B., Nano-fabrication: A Review. *Journal of Chinese Institute of Engineers* **2007,** *30*, 441-446.
4. Rodgríguez-Fernández, J.; Pérez-Juste, J.; de Abajo, J.; Liz-Marzán, L., Seeded Growth of Submicron Au Colloids with Quadrupole Plasmon Resonance Modes. *Langmuir* **2006,** *22*, 7007-7010.
5. Chen, B.; Jiao, X.; Chen, D., Size-Controlled and Size-Designed Synthesis of Nano/Submicrometer Ag Particles. *Crystal Growth and Design* **2010,** *10*, 3378-3386.
6. Hajduková, N.; Procházka, M.; Štěpánek, J.; Špírková, M., Chemically reduced and laser-ablated gold nanoparticles immobilized to silanized glass plates: Preperation, characterization and SERS spectral testing. *Colloids and Surfaces A* **2007,** *301*, 264-270.
7. Sperling, R.; Gil, P.; Zhang, F.; Zanella, M.; Parak, W., Biological applications of gold nanoparticles. *Chemical Society Review* **2008,** *37*, 1896-1908.
8. BPp.l.c. *BP Energy Outlook 2030*; London, United Kingdom, 2012.
9. BPp.l.c. *BP Statistical Review of World Energy*; London, United Kingdom, 2012.
10. Atwater, H.; Polman, A., Plasmonics for Improved Photovoltaic Devices. *Nature Materials* **2010,** *9*, 205-213.
11. Hwang, G.; Pang, L.; Mullen, E.; Fainman, Y., Plasmonic Sensing of Biological Analytes Through Nanoholes. *IEEE Sensors Journal* **2008,** *8*, 2074-2079.
12. Zhang, Y.; Hong, H.; Myklejord, D.; Cai, W., Molecular Imaging with SERS-Active Nanoparticles. *Small* **2011,** *7*, 3261-3269.
13. Le Ru, E.; Blackie, E.; Meyer, M.; Etchegoin, P., Surface Enhanced Raman Scattering Enhancement Factors: A Comprehensive Study. *Journal of Physical Chemistry C* **2007,** *111*, 13794-13803.
14. Carraro, C.; Maboudian, R.; Magagnin, L., Metallization and nanostructuring of semiconductor surfaces by galvanic displacement processes. *Surface Science Reports* **2007,** *62*, 399-425.
15. Zamborini, F.; Bao, L.; Dasari, R., *Analytical Chemistry* **2011,** *84*, 541-576.
16. Zhao, L.; Siu, A.; Petrus, J.; He; Z.; Leung, K., Interfacial Bonding of Gold Nanoparticles on a H-terminated Si(100) Substrate Obtained by Electro- and Electroless Deposition. *Journal of the American Chemical Society* **2007,** *129*, 5730-5734.
17. Cerruti, M.; Doerk, G.; Hernandez, G.; Carraro, C.; Maboudian, R., *Langmuir* **2010,** *26*, 432-437.
18. Murray, W.; Barnes, W., Plasmonic Materials. *Advanced Materials* **2007,** *19*, 3771-3782.
19. Willet, K.; Van Duyne, R., Loaclized Surface Plasmon Resonance Spectroscopy and Sensing. *Annual Review of Physical Chemistry* **2007,** *58*, 267-297.
20. Juluri, B. K. DDSCAT and electric field at plasmon resonance. http://juluribk.com/2010/05/26/ddscat-and-electric-field-at-plasmon-resonance/.

21. Kraufer, S., *Solar Electric Generation*. Springer Berlin Heidelberg: Heidelberg, 2006; p 19-48.
22. Green, M., Thin-film solar cells: review of materials, technologies and commercial status. *Journal of Materials Science: Materials in Electronics* **2007,** *18*, 15-19.
23. Zimmermann, Y.; Schäffer, A.; Hugi, C.; Fent, K.; Corvini, P.; Lenz, M., Organic photovoltaics: Potential fate and effects in the environment. *Environmental International* **2012,** *49*, 128-140.
24. Wright, M.; Uddin, A., Organic - inorganic hybrid solar cells: A comparitive review. *Solar Energy Materials & Solar Cells* **2012,** *107*, 87-111.
25. Grätzel, M., Dye-sensitized solar cells. *Journal of Photochemistry and Photobiology C: Photochemistry Reviews* **2003,** *4*, 145-153.
26. Li, B.; Wang, L.; Kang, B.; Wang, P.; Qiu, Y., Review of recent progress in solid-state dye-sensitized solar cells. *Solar Energy Materials & Solar Cells* **2006,** *90*, 549-573.
27. Muller, R.; Kamins, T., *Device electronics for integrated circuits*. 2nd ed.; Wiley: New York, 1986.
28. Catchpole, K.; Polman, A., Plasmonic Solar Cells. *Optical Express* **2008,** *16*, 21793-21800.
29. Jana, S.; Le Donne, A.; Binetti, S., Enhancement of silicon solar cell performances due to light trapping by colloidl metal nanoparticles. *Journal of Physics and Chemistry of Solids* **2011,** *73*, 143-147.
30. Schlücker, S., *Surface Enhanced Raman Spectroscopy: Analytical, Biophysical and Life Science Applications*. Wiley-VCH Verlag & Co.: Weinheim 2011; p 1-37.
31. Spinelli, P.; Ferry, V.; van de Groep, J.; van Lare, M.; Verschuuren, M.; Schropp, R.; Atwater, H.; Polman, A., Plasmonic Light Trapping in thin-film Si solar cells. *Journal of Optics* **2012,** *14*, 1-11.
32. Pudasaini, P.; Ayon, A., Nanostructured thin film silicon solar cells efficiency improvement using gold nanoparticles. *Physica Status Solidi A* **2012,** *208*, 1475-1480.
33. Kneipp, K.; Kniepp, H.; Bohr, H., Single-Molecule SERS Spectroscopy. *Topics in Applied Physics* **2006,** *103*, 261-277.
34. Morton, S.; Jensen, L., Understanding the Molecule-Surface Chemical Coupling in SERS. *Journal of the American Chemical Society* **2009,** *131*, 4090-4098.
35. Kumar, G., Plasmonic nano-architectures for surface enhanced Raman scattering: a review. *Journal of Nanophotonics* **2012,** *6*, 064503-1-064503-20.
36. Escobedo, C.; Brolo, A.; Reuven, G.; Sinton, D., Optofluidic Concentration: Plasmin Nanostructures as Concentrator and Sensor. *NanoLetters* **2012,** *12*, 1592-1596.
37. Brolo, A.; Arctander, E.; Gordon, R.; Leathem, B.; Kavanagh, K., Nanohole-Enhanced Raman Scattering. *NanoLetters* **2004,** *4*, 2015-2018.
38. Andrade, G.; Min, Q.; Gordon, R.; Brolo, A., Surface-Enhanced Resonance Raman Scattering on Gold Concentric Rings: Polarization Dependence and Intensity Fluctuations. *Journal of Physical Chemistry C* **2011,** *116*, 2672-2676.
39. Lee, A.; Ahmed, A.; dos Santos, D.; Coombs, N.; Park, J.; Gordon, R.; Brolo, A.; Kumacheva, E., Side-by-Side Assembly of Gold Nanorods REduces Ensemble-Averaged SERS Intensity. *Journal of Physical Chemistry C* **2012,** *116*, 5538-5545.
40. Yong, K.; Sahoo, Y.; Swihart, M.; Prasad, P., Synthesis and plasmonic properties of silver and gold nanoshells on polystyrene cores of different size and of gold-silver

core-shell nanostructures. *Colloids and Surfaces A-Physiochemical and Engineering Aspects* **2006,** *209*, 89-105.
41. Oldenburg, S.; Westcott, S.; Averitt, R.; Halas, N., Surface enhanced Raman scattering in the near infrared using metal nanoshell substrates. *Journal of Chemical Physics* **1999,** *111*, 4729-4735.
42. Minati, L.; Torrengo, S.; Rossi, B.; DallaSerra, M.; Antonini, V.; Speranze, G., Synthesis and charaterization of Raman active gold nanoparticles. *Colloids and Surfaces A: Physiochemical and Engineering Aspects* **2011,** *386*, 92-97.
43. Magagnin, L.; Maboudian, R.; Carraro, C., Gold Deposition by Galvanic Displacement on Semiconductor Surfaces: Effect of Substrate on Adhesion. *Journal of Physical Chemistry B* **2002,** *106*, 407.
44. Yeshchenko, O.; Dmitruk, I.; Grytenko, K.; Prokopets, V.; Kotko, A.; Schrader, S., Influence of interparticle interaction on melting of gold nanoparticles in Au/polyetrafluoroethylene nanocomposites. *Journal of Applied Physics* **2009,** *105*, 094326.
45. Yagi, S.; Oeda, N.; Kojima, C., Electroless Growth of Size-controlled Gold Nanoparticles Using Hydroquinone. *Journal of the Electrochemical Society* **2012,** *159*, H668-H673.
46. Liu, J.; Ashmkhan, M.; Wang, B.; Yi, F., Fabrication and reflection properties of silicon nanopillars by cesium chloride self-assembly and dry etching. *Applied Surface Science* **2012,** *258*, 8825-8830.
47. Sandu, T.; Vrinceanu, D.; Gheorghiu, E., Surface plasmon resonances of cluster nanoparticles. *Plasmonics* **2011,** *6*, 407-412.
48. de Souza, M.; Corio, P.; Brolo, A., Cu nanoparticles enable plasmonic-improved silicon photvoltaic devices. *Physical Chemistry Chemical Physics* **2012,** *14*, 15722-15728.
49. van Sark, W.; Meijerink, A.; Schropp, R., Solar Spectrum Conversion for Photovoltaics Using Nanoparticles. In *Third Generation Photovoltaics*, Fthenakis, V., Ed. Intech: 2012; p 4.
50. Weller, R.; Ryle, W.; Newton, A.; McMahon, M.; Miller, T.; Magruder, R., A Technique for Producing Ordered Arrays of Metallic Nanoclusters by Electroless Deposition in Focused Ion Beam Patterns. *IEEE Transactions on Nanotechnology* **2003,** (2), 154-157.
51. Dong, W.; Guo, X.; Wang, S.; Wand, Z.; Ming, N., Fabrication of Two-Dimensional Arrays of Micron-Sized Gold Rings Based on Preferential Nucleation at Reentrant Sites. *Chinese Physics Letters* **2008,** *25* (2957-2960).
52. Kim, S.; Jung, J.; Choi, D.; Jung, H.; Yang, S., Patterned Arrays of Au Rings for Localized Surface Plason Resonance. *Langmuir* **2006,** *22*, 7109-7112.
53. Laurent, G.; Félidj, N.; Grand, J.; Aubard, J.; Lévi, G., Raman Scattering images and spectra of gold ring arrays. *Physical Review B* **2006,** *73*, 245417.
54. Zhang, W.; Zhang, S.; Liu, Y.; Chen, T., Evolution of Si suboxides into Si nanocrystals during rapid thermal annealing as revealed by XPS and Raman studies. *Journal of Crystal Growth* **2009,** *311*, 1296-1301.
55. Perrault, S.; Chan, W., Synthesis and Surface Modification of Highly Monodispersed, spherical Gold Nanoparticles of 50-200 nm. *Journal of the American Chemical Society* **2009,** *131*, 17042-17043.

56. Zheng, J.; Zhu, Z.; Liu, Z., Nanopatterned Assembling of Colloidal Gold Nanoparticles on Silicon. *Langmuir* **2000,** *16*, 4409-4412.
57. Raut, H.; Ganesh, V.; Sreekumaran Nair, A.; Ramakrishna, S., Anit-reflective coatings: A critical, in-depth review. *Energy & Environmental Science* **2011,** *4*, 3779-3803.
58. Sai, H.; Kanamori, Y.; Arafune, K.; Ohshita, Y.; Yamaguchi, M., Light Trapping Effect of Submicrom Surface Textures in Crystalline Si Solar Cells. *Progress in Photovoltaics: Research and Applications* **2007,** *15*, 415-423.
59. Zhao, L.; Zuo, Y.; Zhou, C.; Li, H.; Diao, H.; Wang, W., Theoretical investigation on the absorption enhancement of the crystalline silicon solar cells by pyramid texture coated with SiN_x:H lyer. *Solar Energy* **2011,** *85*, 530-537.